DEVELOPMENT OF NEWLY BUILT CHIRPED-PULSED FOURIER TRANSFORM MICROWAVE (CP-FTMW) SPECTROMETER FOR STUDYING BIOMOLECULES IN THE GAS PHASE

by

Ryan George Bird

B.S., Southampton College, 2004

Submitted to the Graduate Faculty of

Arts and Sciences in partial fulfillment

of the requirements for the degree of

Doctor of Philosophy

University of Pittsburgh

2011

UNIVERSITY OF PITTSBURGH

ARTS AND SCIENCES

This dissertation was presented by

Ryan George Bird

It was defended on

July 27th, 2011

and approved by

Committee Members:

Dr. Sunil K. Saxena, Associate Professor
Department of Chemistry, University of Pittsburgh

Dr. Stephen G. Weber, Professor
Department of Chemistry, University of Pittsburgh

Dr. Trevor J. Sears, Professor
Department of Chemistry, State University of New York at Stony Brook

Dissertation Advisor:

Dr. David W, Pratt, Professor,
Department of Chemistry, University of Pittsburgh

DEVELOPMENT OF NEWLY BUILT CHIRPED-PULSED FOURIER TRANSFORM MICROWAVE (CP-FTMW) SPECTROMETER FOR STUDYING BIOMOLECULES IN THE GAS PHASE

Ryan Bird, Ph.D.

University of Pittsburgh, 2011

Recent advances in the technology of oscilloscopes and digital waveform generators have made it possible to shorten collection times, increase scan bandwidths and improve the overall sensitivity of microwave spectroscopy. Thus, microwave spectroscopy has become a powerful tool for the determination of the structures of molecules. The Pate group, at the University of Virginia, has developed a new technique called chirped-pulse Fourier transform microwave (CP-FTMW) spectroscopy that has the ability to measure the broadband pure rotational spectra of large molecules. Working in collaboration with the Pate group, we have developed, at the University of Pittsburgh, a small version of the UVa spectrometer. This version of the CP-FTMW spectrometer uses a narrower bandwidth pulse, ~500 MHz, which makes it possible to record a spectrum using lower power amplifiers at significantly reduced cost. Using this new spectrometer, the pure rotational spectra of N,N′-dimethylaniline, 4,4’-dimethylaminobenzonitrile, *o*-toluidine, *m*-toluidine, 4-fluorobenzyl alcohol, valeric acid, and δ-valerolactam were collected and studied. From these spectra, their three-dimensional structure, bonding properties, and intermolecular interactions were determined.

TABLE OF CONTENTS

LIST OF TABLES

LIST OF FIGURES

LIST OF EQUATIONS

LIST OF SCHEMES

PREFACE

This dissertation would not have been possible without the guidance and inspiration of my advisor, Dr. David W. Pratt. His passion for science and endless support allowed me to develop the necessary skills to accomplish my own research goals. I am also very thankful for the opportunity to learn from him and work under him.

Most importantly, I would like express my gratitude to our collaborators at the University of Virginia. The principal investigator there, Dr. Brooks H. Pate, has been a source of great inspiration as he is able to lead the charge in developing new technology in microwave spectroscopy. I am especially thankful to Justin L. Neill for building the initial version of our spectrometer and for his endless help. I would also like to thank past and present members of the Pate group including Dr. Gordon G. Brown, Dr. Steve T. Shipman, Matt Muckle and Daniel P. Zaleski for all their work and helpful advice.

I also owe a great deal of thanks to many Pratt group members, both current and previous. Dr. Leonardo Alvarez, Dr. Diane M. Miller, Dr. Philip J. Morgan, Adam J. Fleisher, Justin W. Young, and Dr. Vanesa Vaquero have all been instrumental in teaching me the art of spectroscopy and the science behind it.

I also owe a great deal of gratitude to those in the spectroscopy community who have created spectral fitting tools, since without these programs my research would not have been possible. I would like to thank Dr. David Plusquellic for creating JB95, Dr. Herbert Pickett for

SPFIT/SPCAT, Dr. Holger Hartwig for XIAM, and Dr. Isabelle Kleiner for BELGI. Additionally, I would like to thank Dr. Zbigniew Kisiel and Dr. William Bailey for their helpful websites (http://www.ifpan.edu.pl/~kisiel/prospe and http://web.mac.com/wcbailey/nqcc, respectively).

Without the skill of the machine and electronics shop staff at the University of Pittsburgh, none of the experiments would have been possible. I am forever grateful for all of their help and hard work, especially Tom Gasmire, Dennis Sicher, and Jeff Sicher in the machine shop and Bob Muha, Chuck Fleishaker, and Jim McNerney in the electronic shop.

I would also like to thank my whole family from the bottom of my heart for their support and prayers, my parents, brother, sister, grandparents, family-in-law and soon-to-be family-in-law. Most of all I, would like to thank my fiancé, Leanna Stitt, whose constant encouragement, love, and support gave me the necessary inspiration and motivation to complete this research.

Ryan G. Bird

1.0 INTRODUCTION

Recent advances in the technology of oscilloscopes and digital waveform generators, fueled by the computer and telecommunications industries, have made it possible to shorten collection times, increase scan bandwidths and improve the overall sensitivity of microwave spectroscopy by several orders of magnitude. A new technique that takes advantage of these new advances is chirped-pulse Fourier transform microwave (CP-FTMW) spectroscopy,[1] developed by the research group of Professor Brooks Pate at the University of Virginia (UVa). CP-FTMW uses a single polarizing pulse to obtain a large portion (~10,000 MHz) of the entire rotational spectrum, making it possible to study the structural and dynamical properties of large molecules in the gas phase for the first time.

Working in collaboration with the Pate group, we have developed, at the University of Pittsburgh, a small version of the UVa spectrometer which is described in Chapter 2. This version of the CP-FTMW spectrometer uses a narrower bandwidth pulse, ~500 MHz, which makes it possible to record a spectrum using lower power amplifiers at significantly reduced cost. Additionally, this spectrometer also has the ability to switch from broadband to narrowband (~500 kHz) by changing the quality, or Q factor, of the cavity. A higher Q cavity will have an increased signal-to-noise ratio, but smaller bandwidth; the opposite holds for a lower Q cavity. This new spectrometer will be used to study small biomolecules (*e.g.*; capped amino acids, β-peptides, dipeptides, sugars, and their complexes) and collect their pure rotational spectra. From these spectra, their three-dimensional structure and bonding properties can be determined. In addition, studying conformers will enable a better understanding of their energy landscapes.

Given the goals of this project, certain challenges must be addressed before the more complicated biomolecules can be studied. These include the development of methods to distinguish one conformer of a molecule from another, to assign the spectra of molecules containing quadrupolar nuclei, and to disentangle the complex splitting patterns produced by molecules undergoing internal motions. As will be clear from what follows, these challenges have been met; our solutions to them are described in Chapter 3 (multiple conformers), Chapter 4 (multiple quadrupolar nuclei), and Chapters 5 and 6 (methyl group internal rotations).

Microwave spectroscopy is not a conformer-specific technique and the spectrum of a larger molecule could contain contributions from multiple conformers, making assignments of the transitions the spectrum difficult. Even a "simple" molecule like 1-heptanal could have as many as 15 conformers.[2] Therefore, we developed a technique to differentiate the spectrum of one conformer from another. This technique, known as microwave-optical double resonance (MODR), combines the conformer-specific ability of fluorescence spectroscopy with the simplicity of microwave spectroscopy. MODR uses a tunable UV laser to excite one conformer to an electronically excited state. This interaction would affect the intensity of the entire microwave spectrum of one conformer, but not the others, thus making it easy to distinguish one conformer's spectrum from the others.

Quadrupolar nuclei, generally nitrogen (N-14) in most biomolecules, increase the spectral density of a microwave spectrum by splitting each transition into several lines (by a factor ~3^N, where N is the number of quadrupolar nuclei). However, with this complication also comes another spectral fitting parameter, as splitting patterns are dependent on the hybridization and connectivity of the nuclei. In our study of N,N′-dimethylaniline (DMA) and 4,4’-dimethylaminobenzonitrile (DMABN), we learned how to fit a molecule with multiple nitrogens. In addition, we learned how to use the quadrupole coupling constants to describe the local environment around the nitrogen.

Internal motion in a molecule also leads to spectral confusion by causing splittings in spectra due to quantum mechanical tunneling under a barrier hindering the motion. This tunneling can result in small perturbations (splittings) from a larger barrier and *vice versa* for a small barrier. We have demonstrated the ability to fit both small and larger barrier methyl rotors in *m*-toluidine and *o*-toluidine, respectively. We have also been able analyze the motion of the –CH_2OH group in 4-fluorobenzyl alcohol, which showed rotation-vibration coupling that further perturbed the splittings in the spectrum. In addition to learning how to fit the previously mentioned molecules, we have also learned to use multiple spectral fitting programs including JB95,[3] SPFIT/SPCAT,[4] XIAM,[5] and BELGI.[6]

Finally, as described in Chapter 7, we were able to study amino acid mimics such as valeric acid, 5-aminovaleric acid (AVA), δ-valerolactam and its water complexes.[7] Upon heating, AVA reacted to form δ-valerolactam. A study of the reaction pathway of δ-valerolactam identified the preferred structure of AVA and demonstrated the importance of the n→π* interaction in biomolecules. By studying the lowest energy conformations of valeric acid, 5-aminovaleric acid, and δ-valerolactam and comparing them to propanoic acid,[8] GABA,[9] and β-alanine[10] we were able to observe how additions to the carbon backbone can affect the types and strengths of their intermolecular interactions.

1.1 REFERENCES

(1) Brown, G. G.; Dian, B. C.; Douglass, K. O.; Geyer, S. M.; Shipman, S. T.; Pate, B. H. *Rev. Sci. Instrum*. **2008**, *79*, 053103.

(2) Fisher, J. M.; Xu, L.-H.; Suenram, R. D.; Pate, B.; Douglass, K. J. *Mol. Struct.* **2006**, *795*, 143-154.

(3) Plusquellic, D. F.; Suenram, R. D.; Mate, B.; Jensen, J. O.; Samuels, A. C. *J. Chem. Phys*. **2001**, *115*, 3057-3067.

(4) Pickett, H. M. *J. Mol. Spectrosc.* **1991**, *148*, 371-377.

(5) Hartwig, H.; Dreizler, H. *Z. Naturforsch., A: Phys. Sci*. **1996**, *51*, 923-932.

(6) Hougen, J. T.; Kleiner, I.; Godefroid, M. *J. Mol. Spectrosc*. **1994**, *163*, 559-586.

(7) Evangelisti, L. and Caminati, W. *Phys. Chem. Chem. Phys.* **2010**, *12*, 14433-14441.

(8) Ouyang, B.; Howard, B. J.; *J. Phys. Chem. A.* **2008,** *112*, 8208-8214.

(9) Sanz, M. E.; Lesarri, A.; Peña, M. I.; Vaquero, V.; Cortijo, V.; López, J. C.; Alonso, J. L. J. Am. Chem. Soc. **2006,** *128*, 3812-3817.

(10) Blanco, S.; López, J. C.; Mata, S.; Alonso, J. L.; *Angew. Chem. Int. Ed.* **2010,** *49*, 9187-9192.

2.0 APPLICATIONS OF NEWLY BUILT CHIRPED-PULSED FOURIER TRANSFORM MICROWAVE (CP-FTMW) SPECTROMETER FOR STUDYING BIOMOLECULES IN THE GAS PHASE

J.L. Neill built the spectrometer;
R.G. Bird performed the experimental measurements, analyzed the spectra, and wrote the paper

2.1 INTRODUCTION

In biology, the structure of molecule is synonymous with its function. Therefore, without knowing its structure, its function cannot be fully understood. Currently, the most popular methods to determine the structures of molecules are NMR and X-ray crystallography. However, both of these methods are condensed phase techniques; NMR samples are usually liquids, while X-ray crystallography samples are solids. Since these molecules are in the condensed phase, their true structure cannot be determined accurately. This is because solvent molecules can interact with the sample and affect its three-dimensional structure. The best way to solve this problem is to work in the gas phase with techniques such as fluorescence and microwave spectroscopy. Fluorescence is a very powerful tool for determining structure, but the molecule must have a strong fluorophore. Microwave spectroscopy, on the other hand, only requires the molecule to have a dipole moment. Other possibilities for structural determination are through theoretical calculations such as Gaussian. However, these calculations are not always accurate and require multiple computers to complete in a timely manner. In addition, these calculations will need spectroscopic data to benchmark their accuracy. Recent advances in the technology of oscilloscopes and digital waveform generator, fueled by the computer and telecommunications industries, have made it possible to shorten collection times, increase scan bandwidth and improve the overall sensitivity of microwave spectroscopy. Thus, microwave spectroscopy has become a powerful tool for the determination of the structures of molecules.

2.2 MICROWAVE SPECTROMETER

Fourier transform microwave spectroscopy (FTMW) can best be summarized in four simple steps (Figure 2.1). First, the microwave pulse is generated by either an analog source; *i.e.*, a klystron or magnetron or a digital source, such as a synthesizer or arbitrary waveform generator. The frequency of this pulse is tuned so that it is resonant with a rotational transition in the ground electronic, ground vibrational state. This pulse causes populations in the two different rotational levels (a and b) to mix, creating a macroscopic polarization. The macroscopic polarization begins to lose coherence and emits a free induction decay (FID). The FID is then converted from the time domain to the frequency domain by Fourier transform. FTMW is thus completely analogous to FT-NMR.

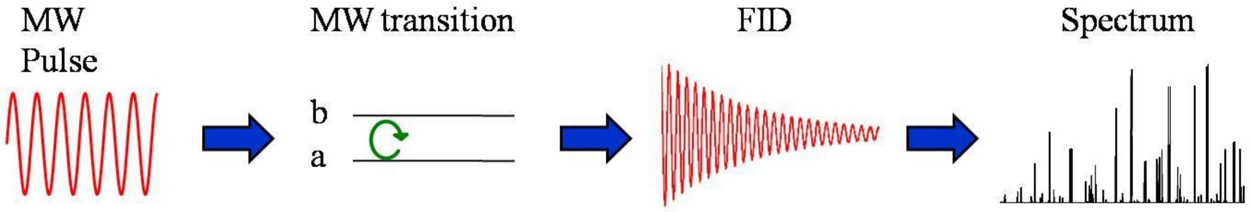

Figure 2.1. Simplified diagram of Fourier transform microwave spectroscopy

A free-induction decay can best be described using the Bloch vector diagram in Figure 2.2. The z-axis represents the population difference between the two states, a and b, and the arrow represents the macroscopic polarization of the sample. Without a microwave field present, a majority of the molecules lie in the lower state due to the Boltzmann distribution. Once the microwave field interacts with the sample, it mixes the two states, which rotates the vector into the xy-plane. The macroscopic polarization then begins to lose its coherence and the vector spreads out into different components and emits a FID.

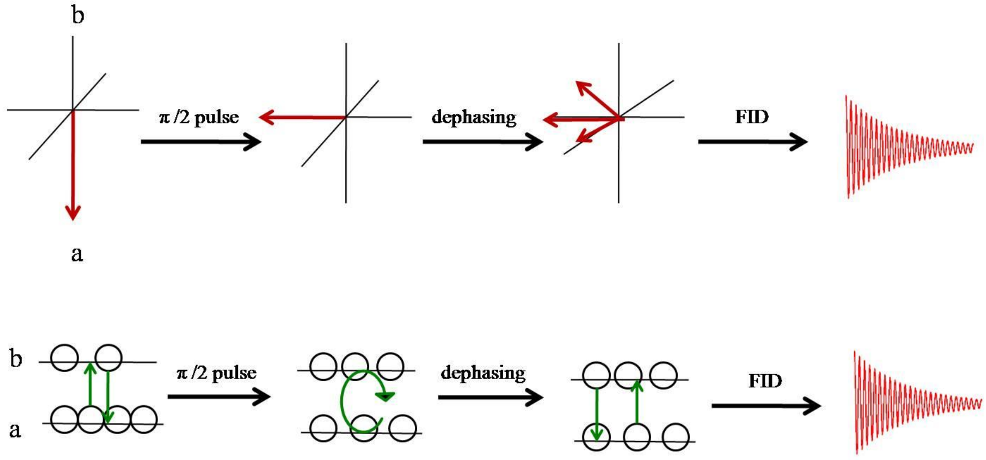

Figure 2.2. A depiction of the excitation of a microwave transition that results in the emission of a FID. The top scheme represents this interaction in the form of a Bloch vector diagram, while the bottom trace uses a energy level diagram.

Another way to describe the FID is to look at a two-level-system energy diagram. With no electric field present, the molecules switch between states due to collisions, but a majority still remains in the lower level. Upon interaction with the microwave field, the two states are mixed with an equal number of molecules existing in each state. This mixing of the two states creates an non-equilibrium state known as a superposition state. If these molecules remain in this coherent state, they would emit a signal of constant amplitude infinitely. However, they begin lose their coherence from collisions and other interactions between molecules. These molecules still emit a signal at the same frequency, but their phases are different. This dephasing causes destructive interference which decreases the amplitude of the signal over time, which gives the FID its shape. This shape can be described by Equation 2.1,

$$\boldsymbol{S_{fid}(t) = \frac{4\pi\mu\omega_0}{cE_0}(N_b - N_a)e^{(-t/T_1)}e^{(-t/T_2)}cos(\omega_0 t)} \tag{2.1}$$

where the decay term T_1 describes the relaxation of the level populations caused by collisions and the T_2 term describes the relaxation of the macroscopic polarization owing to the loss of phase coherence.[1,2] Since the molecules in this experiment are expanded through a supersonic jet, collisions are expected to be minimum, and T_2 is expected to dominate the decay rate. The intensity of the FID is dependent on the population difference between the two levels, $(N_b - N_a)$, the dipole moment of the molecule, μ, and the electric field, E_0.

Our own spectrometer was built at the University of Virginia and moved to the University of Pittsburgh in late October of 2007. Preparations were immediately made to facilitate the setup and installation of the instrument. Vacuum, water, and electrical lines were installed in the laboratory for the operation of the diffusion pump. In addition, several safety precautions were installed to prevent the diffusion pump from overheating, including cooling water flow-meter and high temperature cut-off switches. To make the instrument more efficient, a gate valve was inserted between the chamber and the diffusion pump. This allowed the chamber to be opened to atmosphere while the pump was still on, eliminating the time required for the pump to cool down.

This spectrometer is a hybrid of the Balle-Flygare[3-5] spectrometer and the chirped-pulse broadband spectrometer (CP-FTMW) developed by the Pate Group.[6,7] The Balle-Flygare spectrometer uses two spherical mirrors to create a narrowband cavity, while the Pate spectrometer uses microwave horns to create a broadband cavity. Pate's spectrometer uses a single polarizing pulse, called a chirped-pulse, to obtain a large portion of the entire rotational spectrum of a molecule. CP-FTMW uses two recent advances in digital electronics to measure the entire rotational spectrum over 11 GHz frequency range in one pulse. The first is a new digital waveform generator that is fast enough to produce a chirped pulse from 500 MHz to 10 GHz in 1μs. The ability to produce a chirped pulse in such a short period of time is important so it doesn't interfere with the free induction decay emitted from the molecules. The other advance is the development of ultrafast digital oscilloscope. A Fourier transform of an 11 GHz spectrum requires an ultrafast digital oscilloscope in order to collect all the necessary data points.

The newly built spectrometer utilizes a completely digital signal generation and detection method (Figure 2.3). The microwave signal originates from a Tektronix Series 3252 arbitrary waveform generator (AWG). It has the ability to create a digital microwave pulse from 0 to 240 MHz in both standing wave and linear sweep (chirped pulse) form. The AWG creates a 30 MHz pulse that lasts around 100 ns. This pulse is then mixed up with a microwave frequency from an HP 83752B Synthesizer that increases the output pulse to the 8 to 18 GHz range. Because of this mixing up, the synthesizer's frequency is set to 30 MHz less than the frequency of the transition observed. This pulse is then amplified by a 1 W solid state amplifier (Microwave Power Model L0618-30 6-18 GHz) and attenuated by a 0 to 60 dBm attenuator. The attenuator is necessary to prevent the transition of interest from being saturated. Next, the pulse travels through a circulator and into the chamber and is broadcast into the cavity by an antenna. Once the microwave pulse dies out in the cavity, the free induction decay (FID) emitted from the molecules can be detected. The FID is then transmitted back through the antenna, the chamber, and the circulator. This FID then passes through a switch, which protects the low-noise amp (Miteq AMF-5F-08001800-14-10P) from the power of the initial microwave pulse. Next, the FID is amplified by a ~20 times low-noise amp and is mixed down by the same frequency from the synthesizer and amplified again (Miteq AU-1562 0.01-500MHz). This step is necessary because the scope which detects the FID cannot detect GHz frequencies. Finally, the FID is detected on a Tektronix DPO7054 oscilloscope (500 MHz, 20 Gs/s) where it is signal averaged and Fourier transformed.

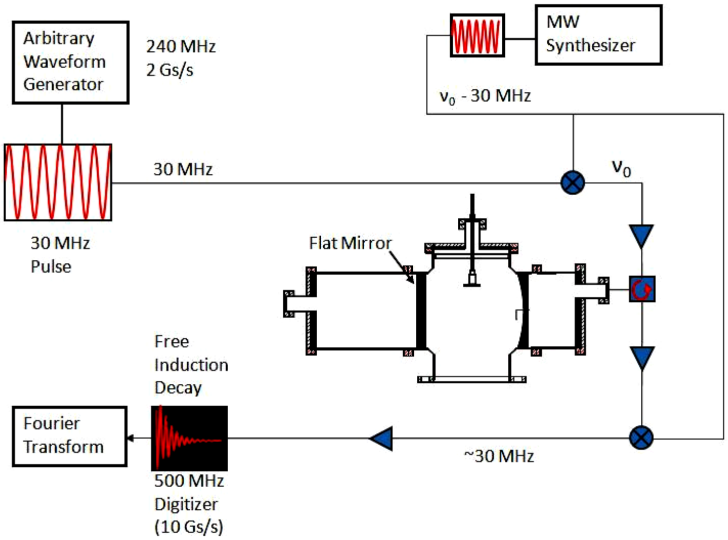

Figure 2.3. The schematic for the narrowband cavity setup. Circles with X's represent mixers, triangles represent amplifiers, and a box with a circular arrow represents a circulator.

The chirped pulse technique requires a slightly different instrumental setup. The first main difference is that instead of a 30 MHz pulse, the AWG generates a chirped pulse of any frequency range from 0-240 MHz. The pulse is created using a program (ArbExpress) included in the oscilloscope software and is then imported into the AWG using a GPIB connection. Also, the synthesizer does not need to be set at 30 MHz less than the desired transition. This is because the purpose of the chirped-pulse technique is to monitor more than one transition, so the synthesizer is set at whichever frequency allows for the greatest sampling efficiency. In addition, the chirped-pulse technique requires a different cavity configuration, either the free space or wide band configuration. Since both of these cavity configurations require a microwave horn to broadcast the signal, the microwave components (circulator, 1W amp, low noise amp, *etc*.) are connected at the other end of the spectrometer.

The chirped pulse, created by the (AWG), can be described by Equations 2.2 and 2.3,[7]

$$E(t) = E_{max}e^{i(\omega_0 t+\frac{\alpha}{2}t^2)} \tag{2.2}$$

where the instantaneous frequency can be determined by:

$$\omega_{inst} = \frac{d}{dt}\left(\omega_0 t + \frac{1}{2}\alpha t^2\right) = \omega_0 + \alpha t. \tag{2.3}$$

The linear sweep rate, α, is dependent on the sweep range and the pulse duration (t_{pulse}),

$$\Delta\omega = \alpha \times t_{pulse}. \tag{2.4}$$

Figure 2.4 shows an example of a chirped pulse signal from 0.001 to 250 MHz. It should be noted that excitation energy for a chirped pulse is constant over all frequencies of the sweep.

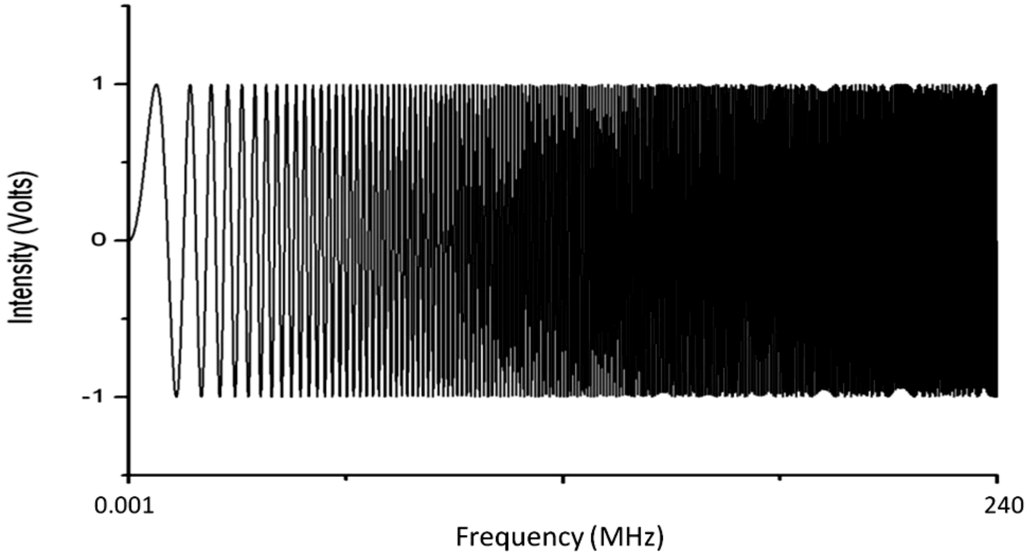

Figure 2.4. A plot of a linear frequency sweep (chirped pulse) for 0.001 to 250 MHz.

Along with signal generation and detection, these instruments need to be aligned in their timing. For this, the T_0 time point is initiated from the AWG which then triggers the scope and synthesizer. In addition, the AWG triggers two Stanford Research Systems DG535 digital delay generators which turns on the 1 W amp, switch, pulsed nozzle, and laser (for double resonance). The sequence of events is that the pulsed nozzle is triggered first. The digital delay sends the trigger signal to an Iota One Pulse Driver, which then triggers the solenoid in the chamber, which creates a gas pulse through a General Valve Series 9 pulsed nozzle with a diameter of 1 mm. This gas pulse usually lasts from between 400 to 600 µs and begins 700-800 µs before the T_0 pulse from the AWG (or about 99.2 ms after T_0 on the same cycle). Next, the 1 W amplifier is triggered (from 500 ns to 1.75 µs after T_0) to amplify and allow the pulse to continue into the chamber. A short time before and after the 1 W amplifier is on, the switch is opened (from 100 ns to 3.75 µs after T_0) to protect the low-noise amp from being damaged from a too-powerful pulse. Finally, at about 3 to 13 µs after T_0, the scope is triggered to Fourier transform the collected free induction decay.

This spectrometer also has the ability to be switched from broadband to narrowband by changing the quality, or Q factor, of the cavity. The Q of a cavity can be calculated by dividing the power stored by the power lost. A higher Q cavity will have an increased signal-to-noise ratio, but smaller bandwidth; the opposite is true for a lower Q cavity. This is because the intensity of the observed transition is proportional to the square root of the Q factor. The bandwidth of the spectrometer is related to the Q of the cavity by

$$\Delta\nu_c = \frac{\nu}{Q} \tag{2.5}$$

where $\Delta\nu_c$ is the bandwidth and ν is the center frequency.

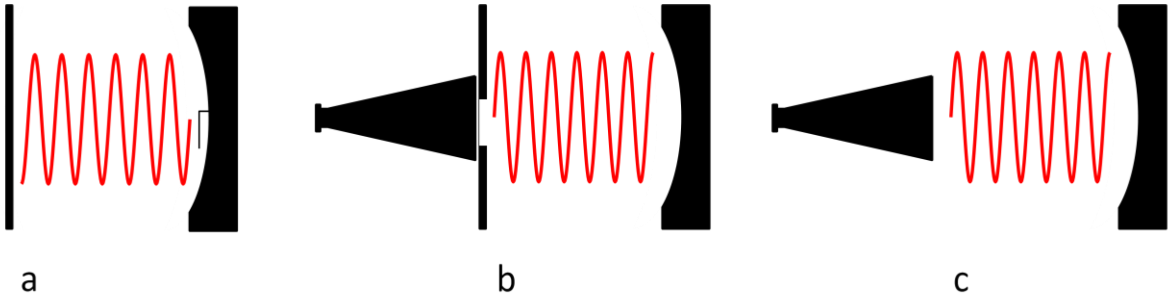

Figure 2.5. The setup for the three different cavities possible in the newly built spectrometer is shown. Narrowband (a) is similar to the Balle-Flygare cavity except one of the spherical mirrors is replaced by a flat mirror. Wideband (b) uses a microwave horn to broadcast the signal and a flat mirror with a hole in it. Free space (c) replaces the flat mirror with a microwave horn to increase the bandwidth to the limit of the AWG.

Three different cavity setups may be used in our spectrometer. These are shown in Figure 2.5. The narrowband cavity setup is similar to Fabry-Perot spectrometer, except that one of the spherical mirrors is replaced by a flat mirror (Figure 2.5a). This change decreases the Q of the cavity but more importantly it creates a simple way to change the cavity/mirror setup. The narrowband setup has a Q of around 10,000 and a bandwidth of 1 MHz. In order to increase the bandwidth of the spectrometer, the Q of the cavity must decrease. This was accomplished by cutting a hole in the flat mirror, which increases the power lost in the cavity. As the Q decreases, more power needs to be coupled into the chamber over a broader frequency range to properly polarize the sample. Therefore, in the wideband setup (Figure 2.5b), a microwave horn is used to broadcast the microwave signal into the chamber. Microwave horns provide better coupling over broad frequency ranges than an antenna. The bandwidth of the cavity can then be adjusted by varying the size of the hole in the flat mirror (Table 2.1). The free space cavity (Figure 2.5c) utilizes just a microwave horn and spherical mirror. The bandwidth of this cavity is limited only by the chirped pulse frequency range of the AWG, which is 480 MHz.

Table 2.1. Hole coupling bandwidth

Hole Size (in)	Cavity Q	Approx. Bandwidth @ 12 GHz (FWHM)
Narrow Band	10000	1.2 MHz
0.255	2400	5 MHz
0.460	240	50 MHz
0.665	150	80 MHz
1.300	80	~150 MHz
Free Space	>10	Limited By Spectrometer (480 MHz)

In order to collect a good spectrum, the cavity length must be adjusted to minimize the power lost for the frequency of interest. These cavity spacings are known as modes and can be monitored using a diode crystal in the same position as the switch on the circulator. The cavity mode is adjusted by increasing or decreasing the cavity length. (The spherical mirror is mounted on a translation stage and can be adjusted by turning a knob located on the outside of the chamber.) The diode crystal is connected to the oscilloscope and the spherical mirror is moved until the mode is located at the center of the scope, which in narrowband corresponds to 30 MHz or the center of the transition of interest. In Figure 2.6, it can be seen that the width of the mode depends on the Q of the cavity. The frequencies where the relative signal is around zero show high loss in the cavity. However, the frequencies with a negative signal are stored in the cavity.

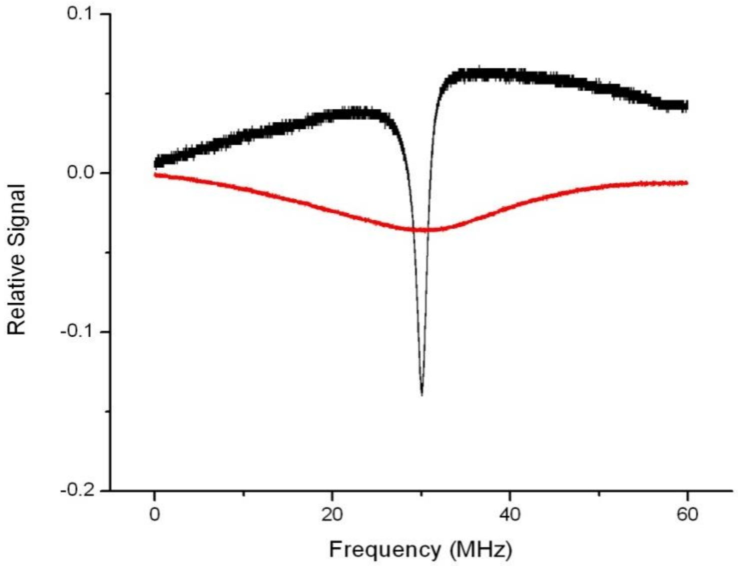

Figure 2.6. Cavity modes of both the narrowband (Black) and the wideband (Red) configuration.

2.3 ACETONE

Once the FTMW spectrometer was properly installed, its operating characteristics had to be determined. This was done by measuring transitions of a molecule with a high vapor pressure whose spectrum had been previously observed. For this test, acetone was chosen. An external sampling container was set up with helium passing over the head-space of acetone. The mixture was then introduced into the vacuum chamber through a 1 mm nozzle using a pulsed valve. The acetone transition of 0_{00}-1_{11} with 5000 averages was observed using the narrowband setup (mirror to mirror cavity) with a 6500:1 signal to noise ratio (Figure 2.7). The intensity and frequency of the transition were comparable with previous data.[8]

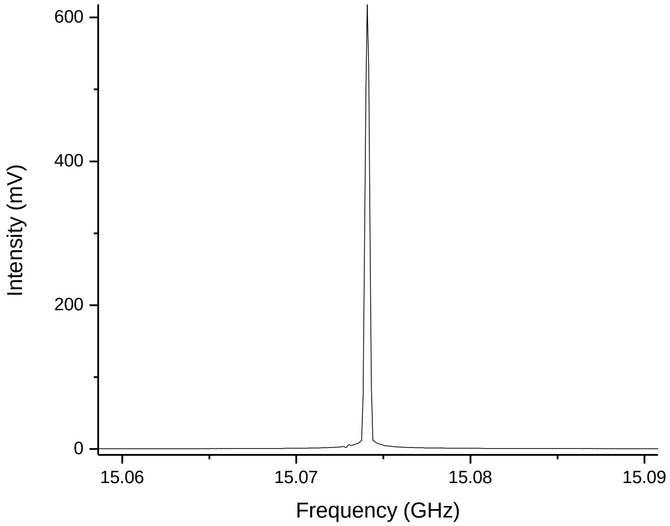

Figure 2.7. Spectrum of the 2_{11}-2_{02} transition of acetone using 5000 averages and the narrowband cavity setup.

Next, the spectrometer cavity was set up for the wide band technique. The acetone transitions of 0_{00}-1_{11} along with three addition transitions were observed using a mirror with a hole diameter of 1.3 inches (Figure 2.8). The increased losses in the cavity due to the hole resulted in a Q of 80 and a bandwidth of around 150 MHz. The signal intensity of a transition is proportional to the $\sqrt{Q}$. The narrowband cavity had a Q of 10000 and created a spectrum of 0_{00}-1_{11} with an intensity of 620 mV while the wideband cavity created an intensity of 8.5 mV. This relationship between Q and signal further confirms that the spectrometer is working properly. Unfortunately, along with decreasing the Q on the cavity, the holed-mirror also blocks some of the pulse from the horn from entering the cavity. Therefore, with the attenuator set at 1 dBm, the 0_{00}-1_{11} was not yet fully polarized. This caused the signal to be less than expected, which accounts for the smaller wideband signal when compared to narrowband. In addition, a C-13 isotopomer can be seen on the left of the main peak at around 15.074 GHz. This isotopomer has about a 2.2% natural abundance.

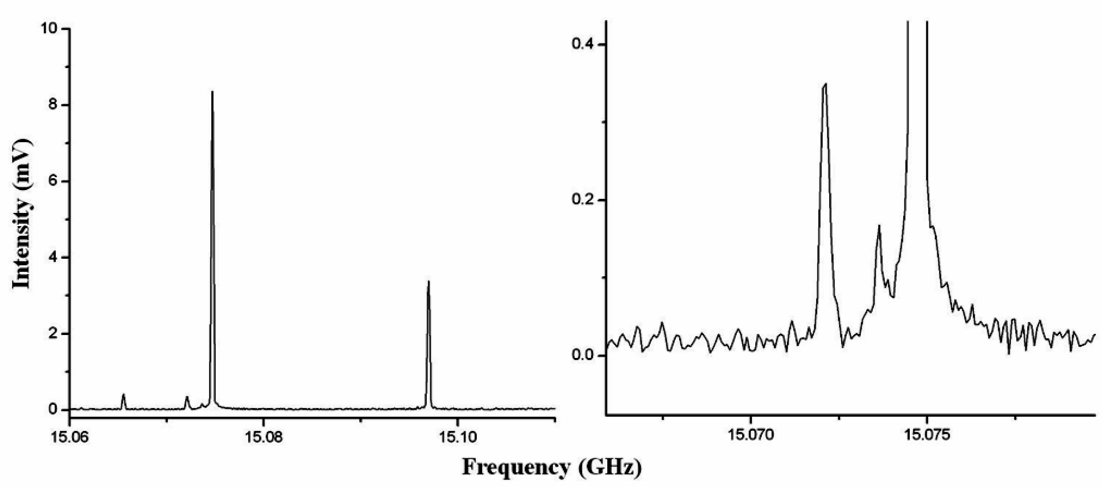

Figure 2.8. Wideband spectra were taken using a mirror with a 1.3 in hole. Three additional transitions can be observed along with the 0_{00}-$1_{11,}$ the most intense transition. On the right, portion of the baseline is zoomed in to reveal a ^{13}C isotopomer of acetone at 15.074 GHz.

Finally, the free space setup was tested (horn to mirror cavity) using a frequency range of 14.8 – 15.3 GHz. In this frequency range, four transitions of acetone were observed with the 0_{00}-1_{11} transition having a signal to noise ratio of 20:1. Both the frequencies of the observed transitions and their relative intensities agreed with those reported in the literature for this molecule. An interesting problem occurs in the free space cavity, which required some ingenuity to overcome (Figure 2.9). Since the free space cavity has essentially no Q, a large bandwidth of frequencies can be stored in it. This becomes a problem when the chirped pulse is mixed with the center frequency from the synthesizer. Two different frequency ranges are created, $\nu_{synth} + \nu_{chirped}$ and ν_{synth} - $\nu_{chirped}$, and broadcasted into the cavity. Then, when these frequencies are mixed down by the synthesizer and collected on the scope, the two spectra are overlaid on top of each other. In order to identify which peaks are on the positive or negative side of the center frequency from the synthesizer (ν_0), the center frequency is changed and the peaks are compared to the original spectrum. The peaks that shift to the left are on the positive side of ν_0, and *vice versa*. Once the peaks are identified, a mirror image of the spectrum is created and the false peaks are then deleted (Figure 2.10).

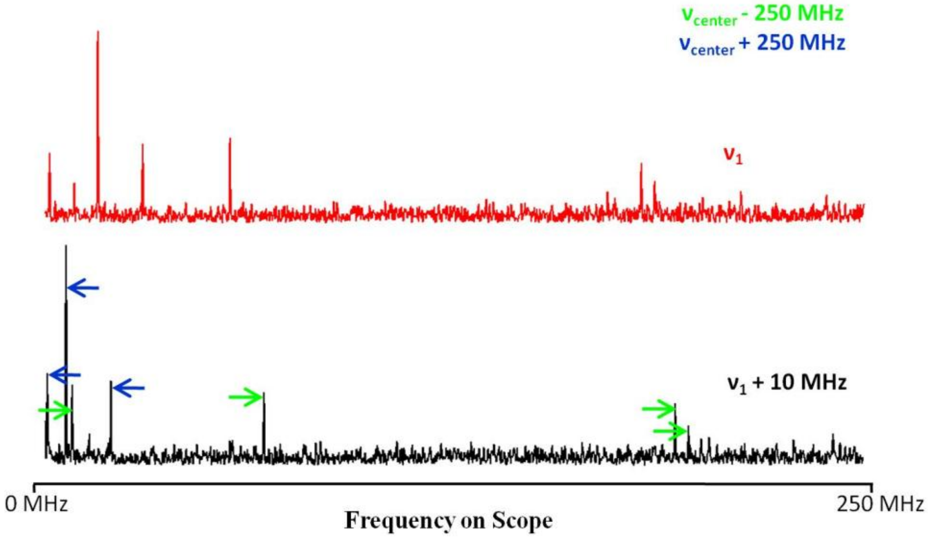

Figure 2.9. A free space spectrum of acetone. The center frequency of the black trace is 10 MHz greater than the red trace. The resulting shift in peaks allow for the proper frequency assignments to be made, either the frequency of the scope plus the center frequency (blue) or minus the center frequency (green).

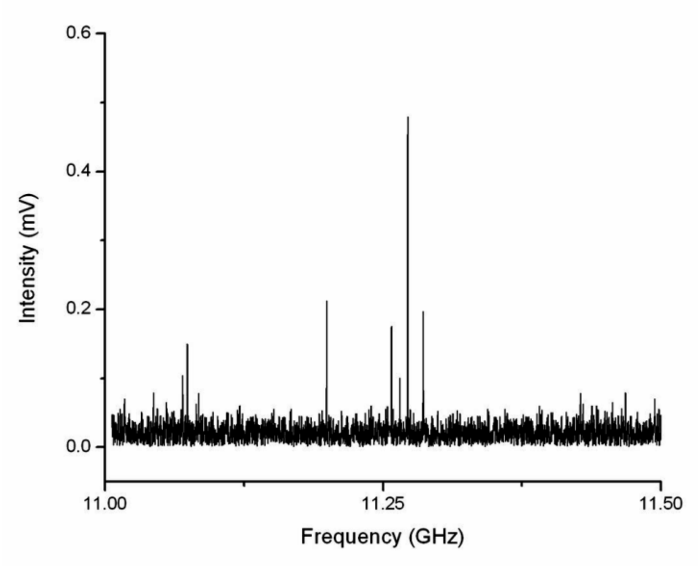

Figure 2.10. The corrected spectrum of acetone from 14.8 – 15.3 GHz with false peaks removed.

2.4 INCREASING SPECTRAL RESOLUTION

Often, when dealing with spectra that exhibit small perturbations, *i.e.* quadrupole or high barrier internal torsional splittings, small peak widths are necessary to resolve the splitting. In most spectroscopic techniques, peak widths are limited by the lifetime of the transition. For instance, the average lifetime for an electronic transition is nanoseconds, resulting in peak widths on the order of a MHz. On the other hand, the average lifetime of a microwave transition is hundreds of microseconds, and the corresponding peak widths are a few tenths of a kHz. Therefore, in order to increase our resolution, the spectrometer and collection method need to be changed.

In Fourier transform techniques, the resolution ($\Delta\omega$) is inversely proportional to the collection time (Δt) and the number of points sampled (N):

$$\Delta\omega \propto \frac{1}{N\Delta t} \tag{2.6}$$

Therefore, to increase resolution, we can either buy a new oscilloscope that has a higher sampling rate, or increase the time over which the FID is collected. Both options are viable, but the latter is easier and much less expensive. Consequently, increasing the FID collection time decreases the signal intensity since the Fourier transform signal is proportional to the average FID amplitude. An example of the advantages and disadvantages of using an extended FID collection time can be seen in Figure 2.11. The spectrum of *o*-toluidine exhibits two types of splittings, the larger splitting is from quadrupole and the smaller, torsional. The quadrupole splitting can be seen in both the 10 μs FID (blue) and 40 μs FID (black); however, the torsional splitting can only be seen in the higher resolution black spectrum. The disadvantage of a longer FID collection time can is that the Fourier-transformed spectrum loses intensity.

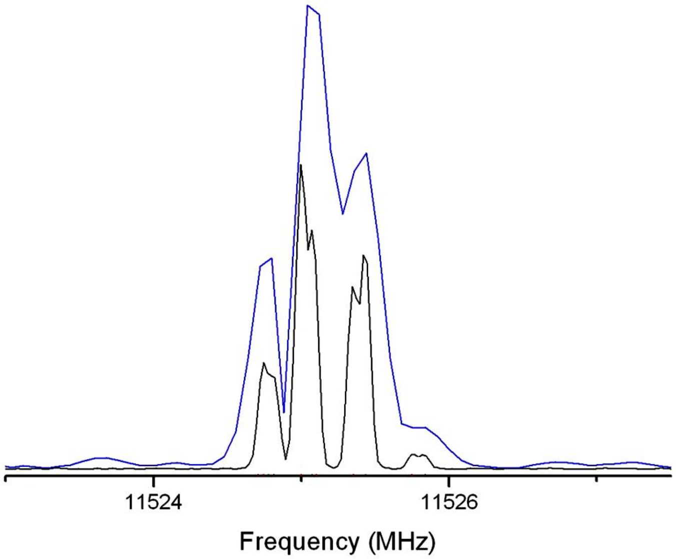

Figure 2.11. The spectrum of *o*-toluidine with the collection of a 10 µs FID (blue) and a 40 µs FID (black), which is increased by a factor of 5, to ease comparison. The spectrum is also split by the larger quadrupole splitting and smaller torsional splittings.

There is, however, a limitation to the length of the FID that can be collected using the spectrometer setup depicted in Figure 2.3. The FID can only be collected while the molecules are in the cavity. To increase the time molecules are in the cavity, the nozzle must moved from a position perpendicular to the microwave axis to one that is parallel. Now the only thing limiting the FID collection length is distance between the mirrors. Figure 2.12 depicts the difference in peak width of an acetone transition between a nozzle perpendicular to the microwave axis (blue) and parallel to the microwave axis (green and red). The green and red spectra are doubled into Doppler doublets caused by molecules emitting signal both towards and against the directions they are traveling. The center of the doublets corresponds to the frequency of the transition. The difference between the peak widths of the green and red spectra are from the backing gas used. The green spectrum used helium and the red spectrum used argon. The heavier argon travels slower, reducing the speed of the molecules in the cavity, allowing for a longer FID detection time. For comparisons, the green and red spectra are increased by a factor of 10.

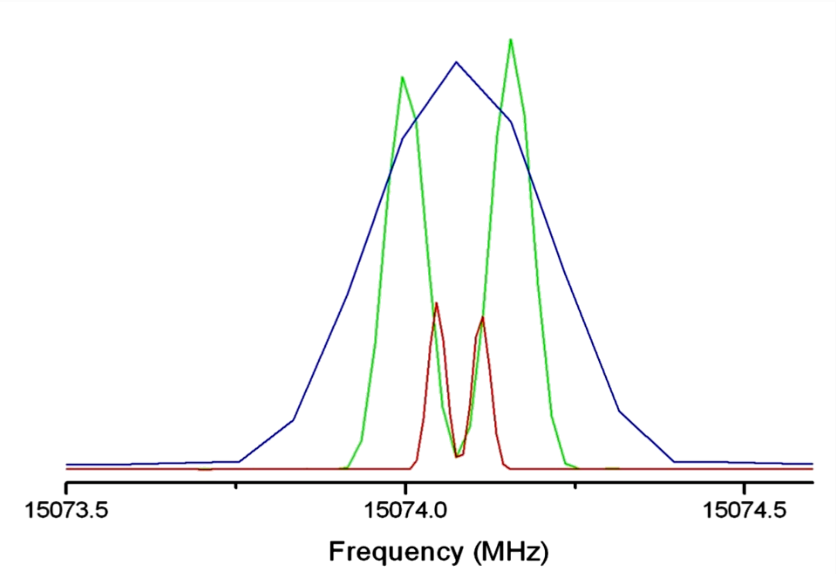

Figure 2.12. The spectrum of acetone using a nozzle perpendicular to the microwave axis (blue), parallel with helium backing gas (green) and parallel with argon backing gas (red). The blue and green spectra are increased by a factor of 10.

2.5 REFERENCES

(1) Flygare, W. H. *Molecular Structure and Dynamics*; Prentice-Hall, Inc., Englewood Cliffs, NJ: United States, 1978.

(2) Steinfeld, J. I. *Molecules and Radiation: An Introduction to Modern Molecular Spectroscopy*; MIT Press,Cambridge, MA: United States, 1978.

(3) Balle, T. J.; Campbell, E. J.; Keenan, M. R.; Flygare, W. H. *J. Chem. Phys.* 1979, *71*, 2723-4.

(4) Balle, T. J.; Flygare, W. H. *Rev. Sci. Instrum.* 1981, *52*, 33-45.

(5) Campbell, E. J.; Buxton, L. W.; Balle, T. J.; Keenan, M. R.; Flygare, W. H. *J. Chem. Phys.* 1981, *74*, 829-40.

(6) Brown, G. G.; Dian, B. C.; Douglass, K. O.; Geyer, S. M.; Pate, B. H. *J. Mol. Spectrosc.* 2006, *238*, 200-212.

(7) Brown, G. G.; Dian, B. C.; Douglass, K. O.; Geyer, S. M.; Shipman, S. T.; Pate, B. H. *Rev. Sci. Instrum.* 2008, *79*, 053103.

(8) Groner, P.; Albert, S.; Herbst, E.; De Lucia, F. C.; Lovas, F. J.; Drouin, B. J.; Pearson, J. C. *The Astrophysical Journal Supplement Series* 2002, *142*, 145-151.

3.0 APPLICATION OF MICROWAVE-OPTICAL DOUBLE RESONANCE TO IDENTIFY MULTIPLE CONFORMERS IN A SINGLE MICROWAVE SPECTRUM

This work was published in part in and is reproduced with permission from
Faraday Discuss., **2011**, *150*, 227-242

R.G. Bird and J.L. Neill performed the experimental measurements;
R.G. Bird analyzed the spectra and wrote the paper

3.1 INTRODUCTION

Past microwave experiments have concentrated on smaller molecules (< 10 atoms) owing to their low boiling points and lack of conformers. This is because microwave spectroscopy is not a conformer specific technique. So the simple microwave spectrum of a molecule could contain contributions from multiple conformers making assigning the transitions or “fitting” the spectrum difficult. This becomes a problem as molecules increase in size, the number of possible conformers increases; *e.g.*, 1-heptanal has as many as 15 conformers.[1]

The first major step in adapting this spectrometer for small biomolecules was to develop a heated nozzle for solid samples. The heated nozzle was developed from a metal nozzle currently used in laser-induced fluorescence experiments. It was modified by raising the sample holder above the bottom of the nozzle, so that it would not interfere with the larger beam waist of the microwave field. Recently, a new digital DC power supply was incorporated into the spectrometer to increase the heating reproducibility of the sample. The new DC power supply was used to replace both an AC power supply and a DC analog power supply. The AC power supply added excessive noise to the FID measured on the scope. The analog DC power supply made it difficult to get accurate and reproducible current readings.

3.2 PYRIDONE MICROWAVE

The new nozzle was then tested by performing experiments on 2-hydroxypyridine (2HP). 2HP was chosen for this test also because it exhibits keto-enol tautomerization (Figure 3.1). 2HP is readily converted to 2-pyridone (2PY) by transfer of a hydrogen atom from the hydroxyl group to the nitrogen atom. As shown in Figure 3.2, 2HP exhibits a very strong microwave transition in the vicinity of 13 GHz. Also apparent is the splitting of this transition into three strong components owing to the presence of the ^{14}N atom in the sample. Both the position of the microwave transition and its characteristic splitting are diagnostic of the presence of 2HP in the sample. 2PY was also observed and both the position of the microwave transition and its characteristic quadrupole splitting are diagnostic of the presence of 2PY in the sample. It was concluded that both the new heated nozzle and the spectrometer were performing adequately.

Figure 3.1. Keto-enol tautomerization of 2-hydroxypyridine

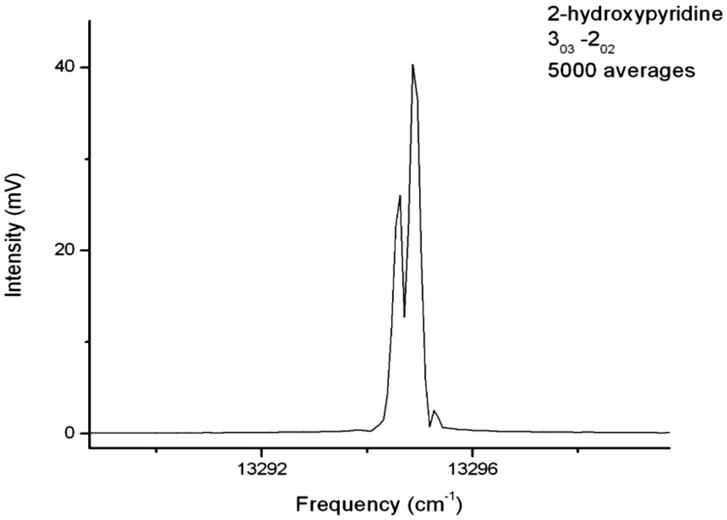

Figure 3.2. Spectrum of the J = 3←2 transition of 2-hydroxypyridine with a frequency of 13.2946233 GHz. The most intense peak is the F= 4←3, followed by F= 2←3 on the left, and F= 1←2 on the right.

The difference in the splitting between 2HP and 2PY can be explained by the distribution of electrons around the nitrogen atom. Kukolich and co-workers[2] were able to collect data on the quadrupole splitting parameters for both 2HP and 2PY and their findings can be summed up in Table 3.1. It should be noted that they defined the x-z plane as the plane of the molecule. 2PY is an aromatic molecule, while 2HP is nonaromatic. This causes the lone pair of electrons in the nitrogen to spend a majority of their time in different orbitals. In 2PY, the electron pair spends a majority of the time in the p_y orbital, which is perpendicular to the aromatic ring. On the other hand, the nitrogen lone pair in 2HP spends most of the time in the p_z orbital, which is in the plane of the aromatic ring.

Table 3.1. N-14 quadrupole coupling strengths and *p*-orbital occupation numbers (Ref 2)

	2-Hydroxypyridine	2-Pyridone
eQq_{xx}	1.2612(4)	1.6335(7)
eQq_{yy}	2.359(6)	-2.759(4)
eQq_{zz}	-3.620(3)	1.1315(6)
$n_x(p_x)$	1.33	1.37
$n_y(p_y)$	1.26	1.74
$n_z(p_z)$	1.76	1.40

Since 2HP readily converts to 2PY, a broadband spectrum would contain transitions of both conformers, as can be seen in Figure 3.3. In the expanded view, the quadrupole splitting in the different conformers can be seen. Without prior knowledge of this molecule it would be difficult to identify which transition is from which conformer and even if the transitions were from different conformers to begin with. Therefore, an additional spectroscopic technique most be incorporated to separate out the conformers.

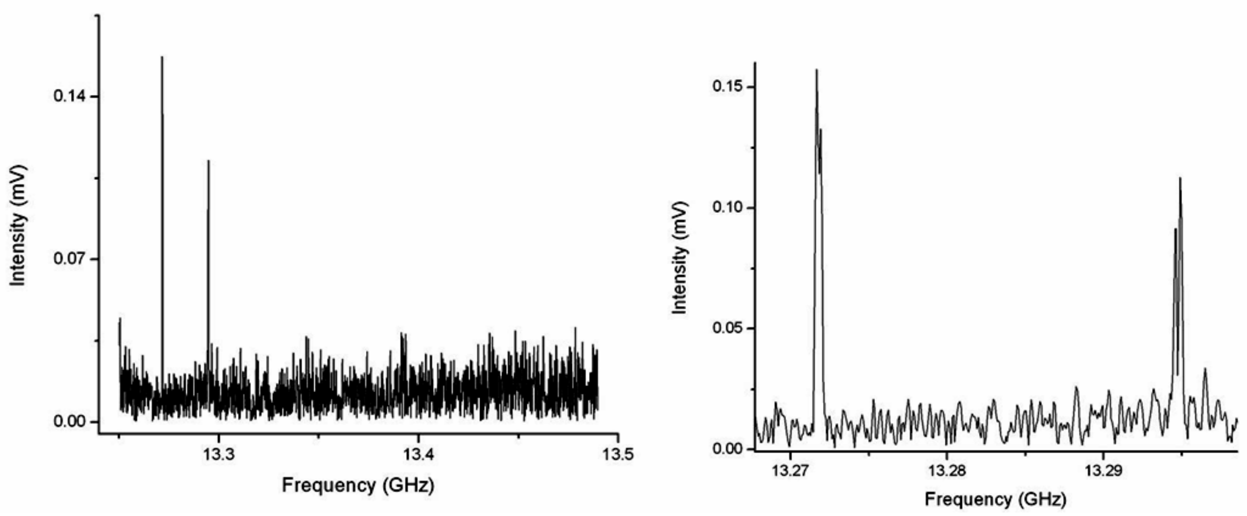

Figure 3.3. Free space spectrum of 2HP and 2PY from 13.25 to 13.50 GHz (left) and an expanded view of both transitions (right).

3.3 DOUBLE RESONANCE

The larger a molecule becomes, the more complicated its rotational spectrum will become. Therefore, the microwave spectrum of biomolecules is expected to consist of many overlapping spectra containing different transitions from different conformers. One way to get around this is to use a technique known as microwave-optical double resonance spectroscopy (MODR).[3,4] It has been discovered that different conformers of large molecules also have different electronic spectra.[5,6] MODR uses a tunable laser to excite one conformer to an electronically excited state. This interaction would result in a change in the intensity of the microwave spectrum of one conformer, but not the others.

In order to perform MODR, a few things needed to be setup. First, a way to introduce the UV light into the spectrometer needed to be devised. The introduction method needs to expand the beam diameter as well. This is because the microwaves and sample fill a majority of the cavity and in order for double resonance to occur properly, the UV light must occupy a similar volume. The easiest way to do this is to place a lens along the path of the UV laser before it enters the microwave spectrometer. Using the Hermite-Gauss mode expansion,

$$\omega = \frac{\lambda}{2\pi}\left(\sqrt{d(2R-d)}\right)^{\frac{1}{2}} \tag{3.1}$$

where λ is the microwave wavelength, d is the mirror distance (16.5 cm), and R is the mirror radius of curvature (30 cm), the beam waist of the spectrometer at 12 GHz was found to be about 3.5 cm. Therefore, the UV laser beam was expanded to about 4 cm, to ensure good overlap.

Another problem that had to be addressed was to devise a way to introduce the laser light into the spectrometer while minimizing power loss from reflection. This problem was overcome by the use of a baffle arm window set at Brewster's angle. When the incident polarized UV laser light passes through a window at Brewster's angle, approximately 56º, the reflectance for that polarization approaches zero. Therefore, the only power lost is due to surface absorption at the windows. Luckily, instead of having to machine a new baffle arm, one from an older cavity was used and slightly modified to make the inner diameter a large as possible to increase the limit to which the laser beam can be expanded.

The third problem had to deal with timing issues. It was necessary to trigger all electrical components of the system off the same initial T_0 pulse, which originated from the arbitrary waveform generator. These electrical components currently include a 1 watt amp, a switch to protect the low-noise amp, the nozzle pulse driver, the microwave synthesizer and oscilloscope. In order to keep everything on the same timing cycle, the UV laser had to be externally triggered as well. Once this was accomplished, the timing of the laser pulses with respect to when the nozzle and microwave pulse fire had to be adjusted to maximize the overlap.

MODR utilizes the interaction of a laser pulse with molecules in either of the two levels of a microwave transition. This interaction causes intensity changes in the FID emitted. There are two possible timing situations for MODR, either the sample interacts with the laser before the microwave field (ground state depletion method) or it interacts with the laser after the microwave field (coherence method).[3,7] In the ground state depletion method, the intensity of the microwave transition would either increase or decrease depending on how the laser interacts with the sample (Figure 3.4). If the laser excites the lower state of the transition, the amplitude of the signal is decreased and *vice versa*. This is because the intensity of the free induction decay of the microwave transition depends on the difference in the population between the lower (N_a) and the upper (N_b) states. Therefore, if the laser excited a molecule from the lower state of the microwave transition, N_a would decrease, resulting in a decrease in population difference and a decrease in the free induction decay signal. If the laser is resonant with the upper state of the microwave transition (N_b), the population difference would increase, resulting in a larger free induction decay signal.

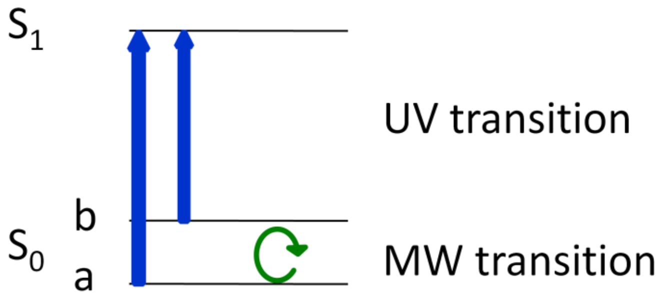

Figure 3.4. Energy level diagram for a microwave-optical double resonance transition is shown above. The green arrow represents a microwave transitions between the lower state a and upper state b. The blue arrows represent electronic transitions from either the a level or the b level of the microwave transition.

In the coherence method, the laser interacts with the sample after the FTMW. This then results in a decrease in the intensity of the signal do to a loss of phase coherence. This occurs when the molecules that were excited return to the ground state and emit a FID. The emitted FID from the excited molecules is out of phase with the free-induction decay of the other molecules. When the two free-induction decays overlap, there is a net decrease in the amplitude due to destructive interference. MODR is therefore a simple way to identify the rotational spectra of specific conformers from the overall microwave spectrum.

3.4 DOUBLE PULSE

A typical double resonance spectrum is collected by monitoring the intensity of a microwave transition while scanning a laser. When the laser is resonant with this transition, it will induce a change in the intensity of the microwave signal. This technique is a powerful tool, but problems can occur from fluctuations in the signal intensity due to shot-to-shot noise. Variations in the temperature of the mirrors or the concentration of the sample in the gas pulse can cause the signal intensity to slowly increase or decrease over the period of the laser scan. This fluctuation leads to a noisy MODR baseline and even false peaks. One way around this problem is a technique developed by the Pate group called double pulse.[7,8] In double pulse, the microwave signal before and after the molecules interact with the laser are subtracted to removed background noise.

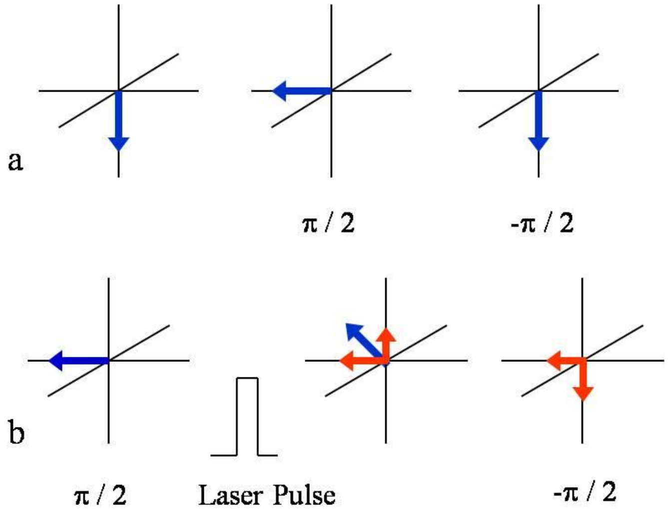

Figure 3.5. A Bloch vector diagram for the double pulse technique

Double pulse is a technique that utilizes the double resonance method of ground-state depletion to produce a background free spectrum. In this technique, the molecules interact with a microwave pulse (π/2), followed by the laser pulse, and then a second microwave pulse 180 degrees out of phase (-π/2). Figure 3.5a depicts the double pulse technique without a resonant laser pulse as a Bloch vector diagram, where the z axis again represents the population difference between two rotational states. The double pulse technique can also be described using a density matrix.[8] Before any interaction occurs, a majority of the molecules occupy the lower state due to the Boltzmann distribution. The first microwave pulse creates a coherence by mixing the two states, which is depicted in the diagram as the vector rotating around the x-axis until it is along the y-axis. If the molecules were just left alone, they would begin to de-phase and emit a FID. However, if a second microwave pulse (-π/2) interacts with the molecules, it will demix them and break up the coherence, thus rotating the vector back down and no FID is observed. Now, if the laser is resonant with either one of the states involved in the microwave transition, the vector will be rotated around the x-axis (Figure 3.5b). This new vector position will be in either above the xy-plane (the laser interacts with the lower rotational level) or below the xy-plane (the laser interacts with the upper state). This vector will have components along both the y and z axes (orange arrow) and after the second microwave pulse rotates back down, there will still be a component of the vector along the y-axis that will de-phase and emit a FID. Therefore, in the double pulse technique, a signal is only observed when the laser is resonant with the microwave transition.

The double pulse technique utilizes the same experimental setup as the basic “microwave only” setup. The only difference is that both channels of the AWG are used to create the pulse. The first channel creates the first microwave pulse. The second channel creates a pulse that is

180 degrees out of phase with respect to the first pulse; its phase and amplitude are manipulated to reduce the transition intensity to as close to zero as possible. This second pulse is then looped back into the AWG and incorporated into the channel 1 pulse. The detection process for double pulse is a little more involved than the basic microwave spectrum generation. While the laser is scanning, its frequency is recorded and later used to generate the plot. The oscilloscope meanwhile records signal-averaged FID's (usually 20 or 100 averages per laser step). These FIDs are then worked up using a Mathcad program where they are Fourier transformed and the intensity at the microwave transition frequency of interest is then recorded. These intensities and their corresponding laser frequencies are plotted to generate a double resonance spectrum.

3.5 IDENTIFICATION OF CONFORMERS

The double pulse double resonance spectra of both 2HP and 2PY were collected monitoring the same microwave transition 3_{03}-2_{02} in each conformer and scanning the laser across their respective origins. The results of these scans are shown in Figure 3.6. It should be clear that the electronic origin for 2HP and 2PY are greatly different, which allows for easy identification of one over the other in a microwave spectrum. Additional information about the excited state can also be gained from these spectra. The positive peaks are electronic transitions that originate from the upper level of the microwave transition, and vice versa for the negative peaks. The three major sets of transitions are the P, Q, and R-branches of the electronic spectrum that result from a ΔJ-1, ΔJ, and ΔJ+1 transition from the ground state. In addition, both molecules have *ab*-hybrid type symmetry which result in different K_a and K_c selection rules which causes the splitting pattern. Therefore, as many as 10 different excited state transitions can be easily identified from a single double pulse spectrum.

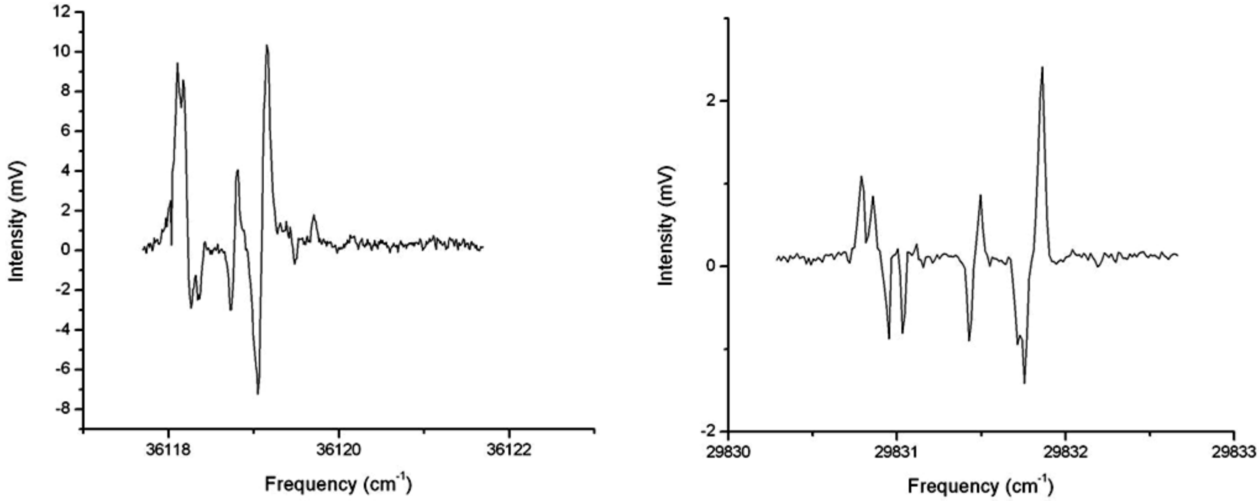

Figure 3.6. Double pulse scans of 2HP (left) and 2PY (right) while monitoring the 3_{03}-2_{02} microwave transition and scanning the laser across their respective origins.

The double pulse technique offers improvements over contemporary double resonance scans, but it also has faults of its own. Double pulse greatly improves the signal to noise ratio and allows for easy identification of transitions. Second, since this is an absorption technique and not a fluorescent one, electronic spectra of non-fluorescing molecules can be determined. However, this technique has yet to be applied to a broadband spectrum where more than one transition is monitored. This is mainly because an additional transition would require an additional frequency for the second pulse. This could be easily overcome with a second AWG. Another problem lies with larger molecules. Using the equations that describe energy levels spacings, it can be determined that the difference in energy between two similar transitions originating in the ground state and ending in an excited state depend upon on the B and C rotational constants, affecting the spacing between positive and negative peaks in a double pulse spectrum. As a molecule increases in size, these constants decrease, which would cause an overlap between positive and negative peaks and a decrease in resolution and intensity.

3.6 EXCITED STATE MICROWAVE SPECTROSCOPY

Not only does the double pulse technique allow for the identification of different conformers, it also gives information about a molecule's excited state geometry. Since rotationally resolved electronic spectra are more condensed, containing hundreds of transitions over only 30 GHz of frequency, a vibrationally resolved UV laser would not have the resolving power to separate out transitions. Double pulse simplifies this congestion by selecting only the excited state transitions that originate from one of two possible ground state levels. Furthermore, these spectra are separated into P, Q and R-branches with positive and negative peaks, which correspond to the ground state levels from which they originate. Since the ground state levels are already known from the microwave assignments, assigning the double pulse spectrum is as simple as identifying the P ($\Delta J = -1$), Q ($\Delta J = 0$) and R-branches ($\Delta J = 1$) and following the selection rules. The resulting assignment of 2HP can be seen in Figure 3.7, where the blue levels are the excited state assignment from transitions that originate from the 3_{03} ground state level, and the red levels are from the 2_{02} ground state level. The excited state spectrum of 2HP contains both *a*- and *b*-type transitions resulting in the small splitting observed in the P-branch.

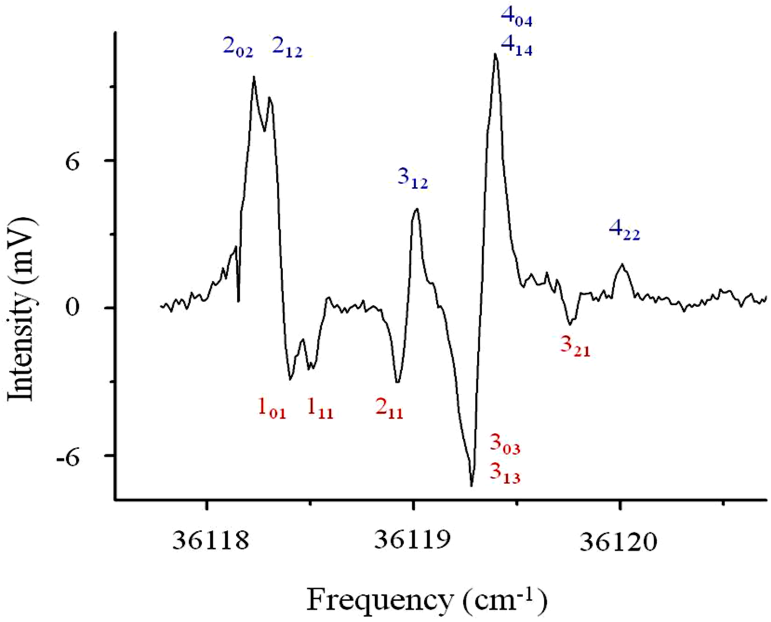

Figure 3.7. The double pulse spectrum of the 3_{03}-2_{02} transition of 2HP. The red assignments are excited state transitions that originate from the 2_{02} ground state level, while the blue excited state assignments originated from the 3_{03} ground state level.

Table 3.2. Comparison of the frequencies of 2HP.

Transition	Double Pulse freq (cm^{-1})	Predicted freq (cm^{-1}) [Ref 8]	Difference (cm^{-1})
3_{03}-2_{02}	36118.1043	36118.2434	-0.1391
3_{03}-2_{12}	36118.1727	36118.3087	-0.1360
2_{02}-1_{01}	36118.2625	36118.3852	-0.1227
2_{02}-1_{11}	36118.3532	36118.4748	-0.1216
2_{02}-2_{11}	36118.7310	36118.8458	-0.1148
3_{03}-3_{12}	36118.8152	36118.9071	-0.0919
2_{02}-3_{13}	36119.0524	36119.1643	-0.1119
2_{02}-3_{03}	36119.0524	36119.1243	-0.0719
3_{03}-4_{04}	36119.1548	36119.2432	-0.0884
3_{03}-4_{14}	36119.1548	36119.2642	-0.1094
2_{02}-3_{21}	36119.4822	36119.6097	-0.1275
3_{03}-4_{22}	36119.7076	36119.8326	-0.1250

Table 3.2 compares the assignments made from double pulse spectrum of 2HP with those from the predicted excited state spectrum determined by Borst, *et al*.[9] As can been seen the errors in the assignments made by the double pulse technique are on the order of the resolution of the UV laser, 0.05 cm^{-1}. The accuracy of the double pulse assignments can be improved by simply improving the resolution of the UV laser, through either using a better etalon or injection seeding the laser. Many modern pulsed solid state lasers can achieve a resolution of 0.005 cm^{-1} or better. Additionally, the assignments made from the double pulse spectrum can be used to calculated excited state rotational constants. A comparison of the rotational constants determined for the double pulse spectrum and those from Borst, *et al*.[9] are shown in Table 3.3. The agreement between the two is very good considering the resolution of the laser used. The percent error can be further reduced by either increasing the resolution of the laser, or collecting and assigning multiple double pulse spectra. Since only J = 2 and 3 levels in the excited state were assigned, the quality of the fit will increase greatly as higher J's are assigned, even if the resolution of the UV laser used remains the same.

Table 3.3. Comparison of 2HP rotational constants between high resolution electronic and double pulse techniques.

S_1 constants	Electronic (MHz) [Ref 8]	Double Pulse (MHz)	Difference (MHz)	% Error
A	5467.1	5187.5	-279.6	5.39
B	2780.5	2869.0	88.5	3.08
C	1844.6	1895.2	50.6	2.67

3.7 SUMMARY

The microwave spectrum of a gaseous sample containing multiple conformers is difficult to assign. Each conformer's spectrum is intertwined with the others. Described herein is a new spectrometer that will make it possible to identify the spectrum of individual conformers, one at a time. A heated source and temperature calibration system was incorporated into the spectrometer for collecting spectra of larger molecules. This new nozzle's ability was confirmed by collecting a spectrum of 2-hydroxypyridine and its tautomer, 2-pyridone. Next, the spectrometer's ability to distinguish the microwave spectra of 2HP and 2PY from a single broadband spectrum was tested. A UV laser was introduced into the chamber and the timing was setup for a double pulse scan. The double pulse scans of both conformers' origin band produced absorption bands with different frequencies. These different frequencies allowed for identification of one conformer over the other. Additionally, it has been demonstrated that excited state rotationally resolved spectra can be obtained and assigned with good accuracy using a microwave spectrometer and a simple low resolution laser.

3.8 REFERENCES

(1) Fisher, J. M.; Xu, L.-H.; Suenram, R. D.; Pate, B.; Douglass, K. *J. Molec. Struct.* **2006**, *795*, 143

(2) Tanjaroon, C.; Subramanian, R.; Karunatilaka, C.; Kukolich, S. G. *J. Phys. Chem. A* **2004**, *108*, 9531-9539.

(3) Nakajima, M.; Sumiyoshi, Y.; Endo, Y. *Rev. Sci. Instrum.* **2002**, *73*, 165-171.

(4) Wormsbecher, R. F.; Harris, D. O.; Wicke, B. G. *J. Mol. Spectrosc.* **1977**, *64*, 86-97.

(5) Nimlos, M. R.; Kelley, D. F.; Bernstein, E. R. *J. Phys. Chem.* **1989**, *93*, 643-651.

(6) Held, A.; Champagne, B. B.; Pratt, D. W. *J. Chem. Phys.* **1991**, *95*, 8732-43.

(7) Douglass, K. O.; Johns, J. E.; Nair, P. M.; Brown, G. G.; Rees, F. S.; Pate, B. H. *J. Mol. Spectrosc.* **2006**, *239*, 29-40.

(8) Neill, J. L.; Pate, B. H. in preparation.

(9) Borst, D. R.; Roscioli, J. R.; Pratt, D. W. *J. Phys. Chem. A* **2002**, *106*, 4022-4027.

4.0 GROUND STATE N-14 QUADRUPOLE COUPLINGS IN THE MICROWAVE SPECTRA OF N,N´-DIMETHYLANILINE AND 4,4’-DIMETHYLAMINOBENZONITRILE

This work was published in and is reproduced with permission from
J. Phys. Chem. A. **2011**, 10.1021/jp111075r

R.G. Bird, J.L. Neill, and V.J. Alstadt performed the experimental measurements;
R.G. Bird and J.L. Neill analyzed the spectra; J.W. Young modeled the barrier height;
R.G. Bird wrote the paper

4.1 ABSTRACT

Microwave spectra of N,N′-dimethylaniline and 4,4’-dimethylaminobenzonitrile have been recorded in a pulsed supersonic jet using chirped pulse techniques. Experimental substitution structures have been determined for both molecules by detection of the spectra of all ^{13}C and ^{15}N isotopomers in natural abundance using a broadband spectrometer. Additionally, narrowband techniques have been used to reveal the ^{14}N quadrupole splittings at high resolution, from which the orbital occupancy numbers of the amino- and cyano-nitrogen atoms have been determined. An apparent direct relationship between these values and the barriers to inversion of the amino groups is discussed.

4.2 INTRODUCTION

4,4’-Dimethylaminobenzonitrile (DMABN) is widely known as a model for excited state twisted intramolecular charge transfer (TICT) dynamics. This type of charge transfer was originally observed by Lippert, *et al.*[1,2] who detected an “anomalous” red-shifted emission in its fluorescence spectrum in polar solvents. Later the Grabowski group[3] suggested that a twisting motion of the dimethylamino group would facilitate the flow of electrons from the amino nitrogen atom to the π* orbitals of the aromatic ring and prohibit its back transfer. Direct evidence for this motion was provided by subsequent studies of DMABN in the gas phase using vibrationally[4] and rotationally[5] resolved electronic spectroscopy techniques.

The local electronic environment around the amino nitrogen can greatly affect the relative ease with which this charge transfer occurs. One way of determining this local environment is by measuring the electric quadrupole interactions of DMABN using microwave spectroscopy. DMABN was previously studied by Kajimoto, *et al.*[6], using microwave spectroscopy; however, they did not measure the quadrupole couplings of either nitrogen. DMABN contains two distinctly different nitrogen nuclei and determining their individual quadrupole interactions is challenging, owing to the increasingly complicated hyperfine structure from multiple quadrupolar nuclei. Our solution to this problem was to study the DMABN analog, N,N′-dimethylaniline (DMA), which contains only a single quadrupolar nucleus, and to perform experiments on DMABN at lower microwave frequencies, where the quadrupole splittings are larger. The spectrum of DMA was previously studied by Lister and co-workers;[7] they detected two small splittings which were attributed to inversion and torsional motions of the -$N(CH_3)_2$ group, but reported no quadrupole splitting. In addition, the splittings of the nitrile group in DMABN should be similar to those of benzonitrile, which have been observed by Grabow and co-workers.[8]

Reported here are studies of the microwave spectra of DMA (6-18 GHz) and DMABN (2-18 GHz) in the collision-free environment of a supersonic jet. Broadband experiments were performed to determine substitution structures of both molecules from the spectra of all ^{13}C- and ^{15}N-substituted isotopologs in natural abundance. Additionally, narrowband experiments were performed to measure the ^{14}N-quadrupole splittings in both DMA and DMABN. Analyses of these data yields direct information about their dynamically averaged structures and the local electronic environment in the vicinity of the nitrogen atoms in both molecules in their ground electronic states.

4.3 EXPERIMENTAL

Figure 4.1 shows a block diagram of the chirped-pulse Fourier transform microwave (CP-FTMW) spectrometer used in this work. Conceptually, it resembles the broadband instrument developed by the Pate group,[9,10] but it employs a significantly narrower pulse (~500 MHz) and a lower power amplifier (~1 W). To offset the power loss, one of the horns was replaced by a mirror to improve the cavity Q. This improvement made it possible to record smaller portions of the spectrum with good signal-to-noise ratio (20:1) at a significantly reduced cost.

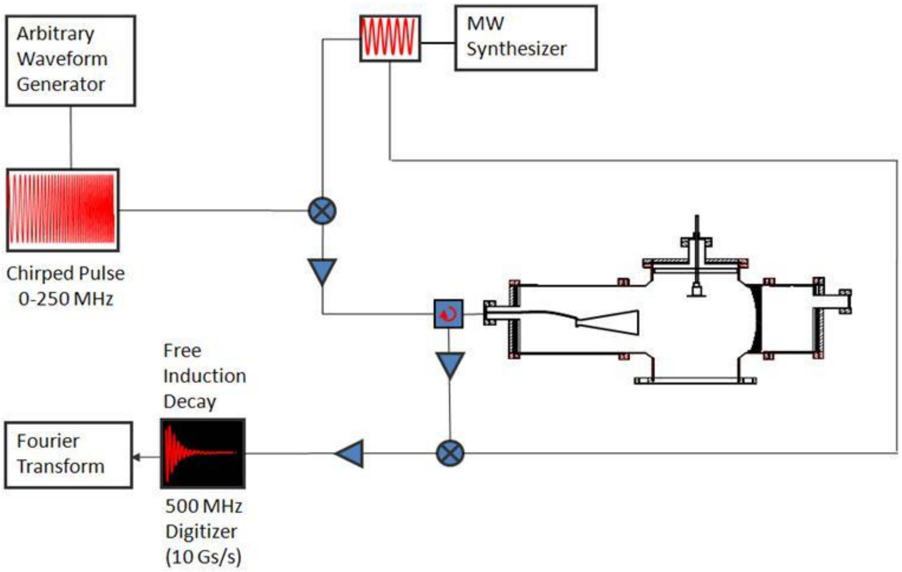

Figure 4.1. Schematic of the broadband CP-FTMW cavity setup. The microwave horn transmits and detects the signal, while the mirror enhances the power stored in the cavity.

DMA and DMABN were purchased from Sigma-Aldrich and used without further purification. DMA was heated to 70 °C and expanded through a pulsed nozzle at 10 Hz with 1 bar He backing gas while DMABN was heated to 130 °C and backed with 2 bar He. The nozzle was placed perpendicular to the microwave propagation axis. The spectra of both molecules were taken between 6.5 and 17.5 GHz in 450 MHz segments, collecting a 10 μs FID and signal averaging for up to 10,000 shots. The segments were then patched together and analyzed using JB95[11] and Pickett's SPFIT/SPCAT.[12-14] To improve the fit of DMA, small portions of several lower frequency transitions were taken using a more powerful 10 MHz chirped pulse to help increase the signal of low intensity $\Delta F = 0$ transitions. A low frequency spectrum, 2-8 GHz, of DMABN also was taken using the UVa low frequency spectrometer.[15] In this case a 4 W solid state amplifier was used to amplify a 9 μs chirped pulse. A 40 μs FID was detected and averaged for 190,000 shots. DMABN was heated to only 120 °C to extend the sample lifetime and backed by 1 bar Ne.

^{13}C and ^{15}N substituted species were detected in natural abundance for both molecules using the UVa 6.5-18.5 GHz CP-FTMW spectrometer[9,10] employing two nozzles and averaging 320,000 FIDs. The results of the fits of the spectra of the 12 substituted DMA and 13 substituted DMABN structures are listed in Supplementary Materials Tables 4.6 and 4.7. The spectrum of DMA was also studied using a newly built 25-40 GHz CP-FTMW spectrometer.[16]

4.4 RESULTS

4.4.1 DMA

The microwave spectrum of DMA between 6-18 GHz consists of a series of μ_a-type R-branch transitions. Each transition is, in turn, split into several components by the combined effects of inversion doubling and quadrupole coupling. This is shown for the case of the $5_{05} \leftarrow 4_{04}$ transition in Figure 4.2, recorded using the more powerful 10 MHz chirped pulse. Inversion doubling produces a splitting of each transition into two components, as was first observed by

Cervellati, *et al.*[7] The lower frequency 0^+ band originates in the lower tunneling component; the higher frequency 0^- band originates in the higher tunneling component. Since the latter is a "hot" band, there is a significant difference in intensity of the two bands.

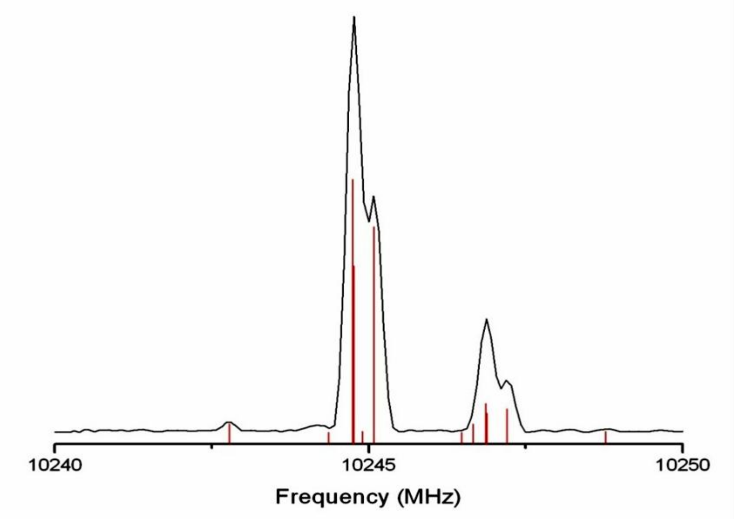

Figure 4.2. The 5_{05}←4_{04} transition of DMA is shown along with the calculated fit (red). The quadrupole splitting can be seen to be similar in both the 0^+ (left) and 0^- (right) bands. The spectrum was collected using a 10 MHz chirped pulse.

Bands 0^+ and 0^- are further split by ^{14}N quadrupole coupling. Both bands exhibit similar splitting patterns (Figure 4.2). Thus, we fit both bands to the Hamiltonian shown below:

$$\hat{\mathrm{H}} = \sum_i \left(\mathcal{H}_i^R + \mathcal{H}_i^{CD} + \mathcal{H}_i^{QUAD}\right) + \mathcal{H}^{\mathrm{INV}}, \text{with } i = +,- \tag{4.1}$$

$$\hat{\mathrm{H}}^{INV} = \Delta E + F_{ac}\,(P_a P_c + P_c P_a) \tag{4.2}$$

Here, $\hat{\mathrm{H}}_i^R$ is the rigid rotor Hamiltonian, $\hat{\mathrm{H}}_i^{CD}$ is the centrifugal distortion Hamiltonian,[17] $\hat{\mathrm{H}}_i^{QUAD}$ is the quadrupole Hamiltonian, and $\hat{\mathrm{H}}^{\mathrm{INV}}$ is the inversion-rotation Hamiltonian,[18] all for the state *i* (= + or -). ΔE is the energy difference between the 0^+ and the 0^- levels and F_{ac} is an interaction term that describes the coupling between the inversion motion of the -N(CH$_3$)$_2$ group and rotational motion about the *b*-inertial axis. However, since the spectrum consists of only *a*-type transitions which are minimally perturbed by this motion, it was difficult to accurately determine the $\hat{H}^{INV}$ terms. Instead, the two bands (0^+ and 0^-) were fit separately, using JB95 and a rigid rotor Hamiltonian. The lower frequency transition of each pair was assigned to the 0^+ level and the higher frequency transition was assigned to the 0^- level. Initial estimates of all parameters were obtained from an *ab initio* calculation and refined in a least-squares fit, shown in red in Figure 4.2. The parameters used to reproduce the experimental spectrum are listed in Table 4.1. Our rotational constants are in good agreement with those previously determined by Lister and co-workers[7] and predicted by *ab initio* calculations.[17]

Table 4.1. Experimental parameters for N,N´-Dimethylaniline.

Parameters	This Work	Lister (Ref. 7)	Theory
A(0^+) (MHz)	3500.35(8)	3500.39	3500.04[a]
B(0^+) (MHz)	1226.668(1)	1226.646	1224.15[a]
C(0^+) (MHz)	923.346(3)	923.328	923.877[a]
A(0^-) (MHz)	3501.35(6)	3499.88	
B(0^-) (MHz)	1226.656(1)	1226.590	
C(0^-) (MHz)	923.596(3)	923.645	
χ_{aa} (MHz)	2.58(4)		2.59[b]
χ_{bb} (MHz)	2.80(6)		2.91[b]
χ_{cc} (MHz)	-5.39(6)		-5.50[b]
ΔI (O^+) (amu Å^2)	-9.0	-9.1	-10.2[a]
ΔI (O^-) (amu Å^2)	-9.1		
N_{lines}	59		

[a] Calculated using Gaussian MP2/6-31+G(d).
[b] Calculated using the optimized structure from Gaussian B3PW91/6-311+G(df,pd).

As expected, the 0^+ level has the smaller value of ΔI, compared to the 0^- level. The 0^+ wavefunction has a higher amplitude in the planar configuration, whereas the 0^- wavefunction has a higher amplitude in the inverted configuration. This confirms the assignment of these two components to inversion doubling. The additional larger splitting observed by Cervellati, *et al.*[7] and attributed to a torsional motion of the $–N(CH_3)_2$ group was not observed in our spectra. Presumably, this is because our sample was colder; the jet expansion should depopulate all vibrational levels whose energy exceeds a few cm^{-1}.

An estimate of the energy difference between the 0^+ and the 0^- levels of DMA was made using the ratio of the intensities and assuming a Boltzmann distribution;

$$\frac{I_-}{I_+} = \frac{g_-}{g_+} e^{\frac{-\Delta E}{kT}} \tag{4.3}$$

Here, I_+ and I_- are the intensities of transitions originating in the 0^+ and 0^- levels, respectively, and g_+ and g_- are the appropriate statistical weights. Since DMA exhibits hyperfine splitting, the total integrated area for each transition was used to estimate its intensity rather than its peak height. For statistical weights, we calculated the nuclear spin statistics for each band assuming 5 pairs of equivalent protons which yields g_+ and g_- values of 33 and 31, respectively. Averaging the results from nine different transitions, and assuming a vibrational temperature of 2 - 3 K, we find $\Delta E = 1.3 - 2.7\ cm^{-1}$.

Some ambiguity exists in the determined value of ΔE given the uncertainty in the vibrational temperature of the jet. A direct measurement of the tunneling splitting in DMA was made possible by studies of the *c*-type $0^+ \leftrightarrow 0^-$ and $0^- \leftrightarrow 0^+$ transitions at higher frequencies. Figure 4.8 shows the microwave spectrum of DMA that was recorded using the 25-40 GHz CP-FTMW spectrometer at UVa, collected using 1.15 million FIDs over 40 hours. Analyses of these data yield the value $\Delta E = 1.92\ cm^{-1}$, in good agreement with our earlier estimate. (The low vibrational temperature is reasonable for such a small splitting.) The observed splitting is within the range (1-3 cm^{-1}) suggested by Cervellati, *et al.*[7], but is much smaller than the corresponding spacing estimated for aniline (46 cm^{-1}).[18] Since the tunneling splitting is inversely proportional to the reduced mass, some decrease in ΔE is anticipated on going from aniline to DMA, but the observed decrease is much larger than expected.

Once an accurate value of this splitting had been determined, a global fit of all measured parameters of both inversion levels of DMA was performed. The results are listed in Table 4.8. The rms of this fit is 28.3 kHz, based on 156 measured pure rotational transitions.

4.4.2 DMABN

Figure 4.3 shows the microwave spectrum of DMABN from 6-18 GHz. As in the case of DMA, the spectrum consists of many strong μ_a-type, R-branch transitions ranging from J=5 to J=16. The higher density of lines has its origin in the significantly smaller rotational constants of DMABN, and in the partially resolved quadrupole hyperfine structure arising from coupling to two ^{14}N nuclei. Unlike DMA, the microwave spectrum of DMABN shows no inversion doubling. The barrier in DMABN could be very large, leading to an unresolvable splitting, or could be very small, leading to a large splitting and a higher lying 0^- level that cools out during the expansion.

The ^{14}N quadrupole structure in DMABN is significantly better resolved at lower microwave frequencies owing to its inverse dependence on J and K; see Figures 4.4 and 4.5. The overview spectrum (Fig. 4.4) from 2 – 8.5 GHz was collected using 190,000 9 µs chirped pulses by signal averaging continuously overnight, and background subtracted for oscilloscope

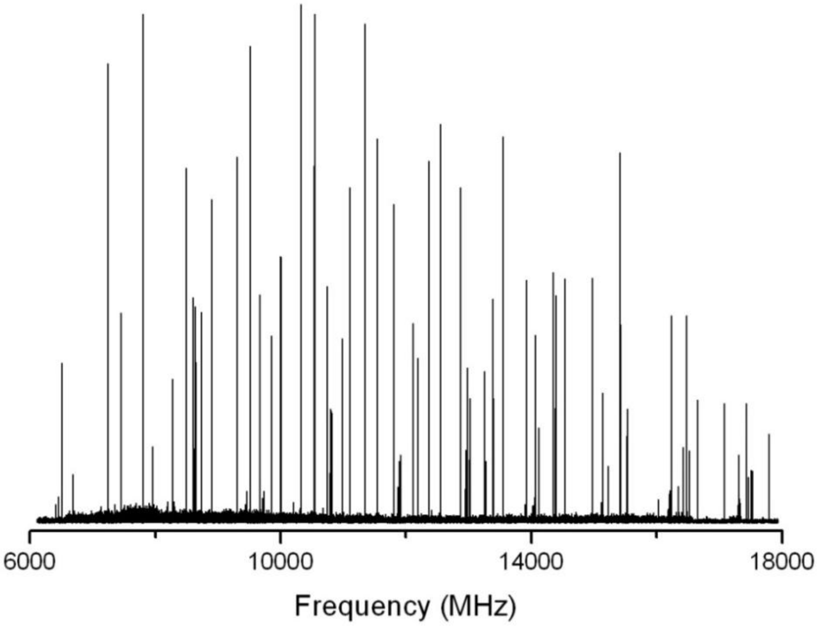

Figure 4.3. Microwave spectrum of DMABN from 6 to 18 GHz, collected using 10,000 450 MHz chirped pulses.

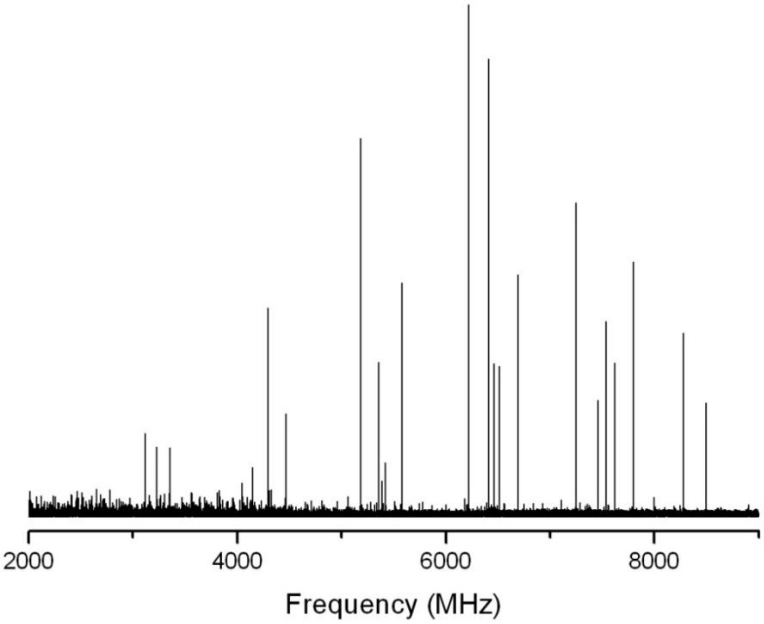

Figure 4.4. Microwave spectrum of DMABN from 2 – 8.5 GHz collected using 190,000 9 μs chirped pulses.

interferences at lower frequencies. Expanded scale views of the transitions observed in this spectrum show a rich hyperfine structure owing to quadrupole coupling with the two ^{14}N nuclei in DMABN. An example is shown in Figure 4.5. This illustrates the $3_{13} \leftarrow 2_{12}$ transition near 3115 MHz; it shows seven resolved transitions lying within a few MHz. In contrast, the $9_{09} \leftarrow 8_{08}$ transition near 9524 MHz shows little resolved structure. SPCAT was used to fit the spectrum; the parameters obtained from this fit are listed in Table 4.2 (see also Fig. 4.5). To the extent that they exist, our values of these parameters compare favorably to previously determined values.[5,6,17]

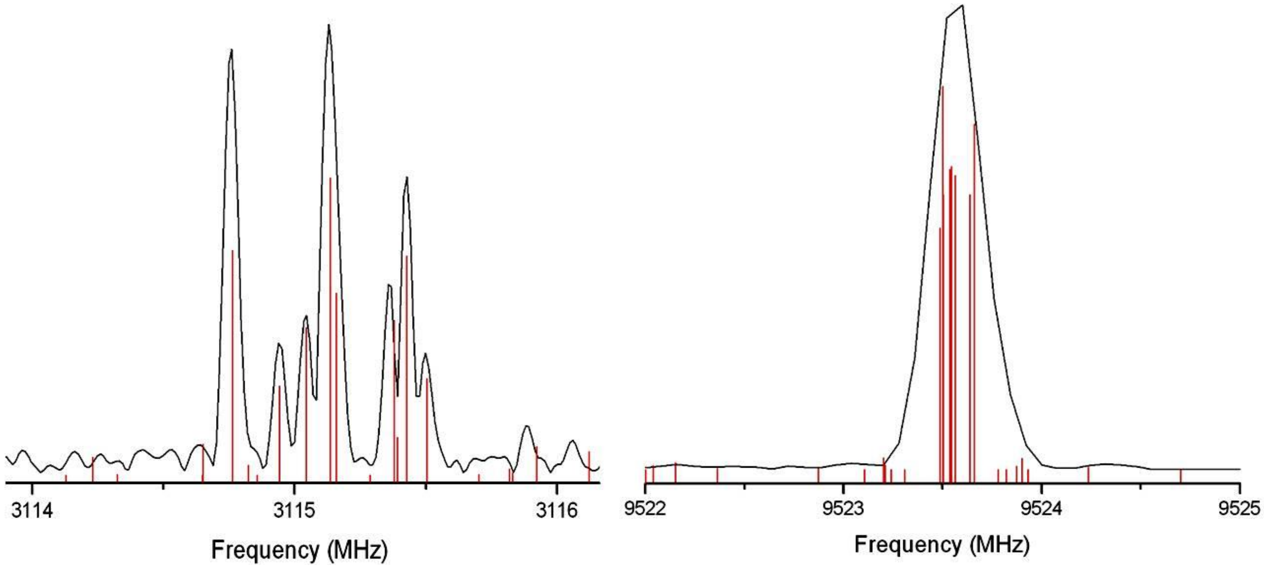

Figure 4.5. The $3_{13} \leftarrow 2_{12}$ transition (left) and the $9_{09} \leftarrow 8_{08}$ transition (right) of DMABN shown together with the calculated fits (in red).

Table 4.2. Experimental parameters for DMABN.

Parameters	This Work	Endo (Ref. 6)	Theory
A (MHz)	3469.25(97)	3469.99	3469.37[a]
B (MHz)	578.5834(29)	578.581	580.998[a]
C (MHz)	499.6121(25)	499.613	500.976[a]
χ_{aa} (MHz)	2.54(33)		2.45[b]
χ_{bb} (MHz)	2.80(13)		2.79[b]
χ_{cc} (MHz)	-5.33(13)		-5.23[b]
χ_{aa} (MHz)	-4.11(30)		-4.11[b]
χ_{bb} (MHz)	2.40(13)		2.47[b]
χ_{cc} (MHz)	1.71(13)		1.63[b]
ΔI (amu Å^2)	-7.61	-7.58	-6.73[a]
N_{lines}	255		

[a] Calculated using Gaussian M052x/6-31+G(d).
[b] Calculated from the optimized structure using Gaussian B3PW91/6-311+G(df,pd).

Finally, substitution structures of both DMA and DMABN were determined using broadband CP-FTMW techniques; see Figure 4.6. Deep signal averaging of both spectra provided rotational constants of all singly labeled ^{13}C- and ^{15}N-isotopomers in natural abundance. These are summarized in the Supplementary Materials Section 4.8; see Table 4.6 and 4.7. Then, comparison of these values using Kraitchman's equations[18] led to the heavy-atom substitution coordinates of both molecules; see Figure 4.9 and Tables 4.9 and 4.10. The experimentally determined values of the (vibrationally averaged) inversion angles are 30.0° (DMA) and 14.6° (DMABN).

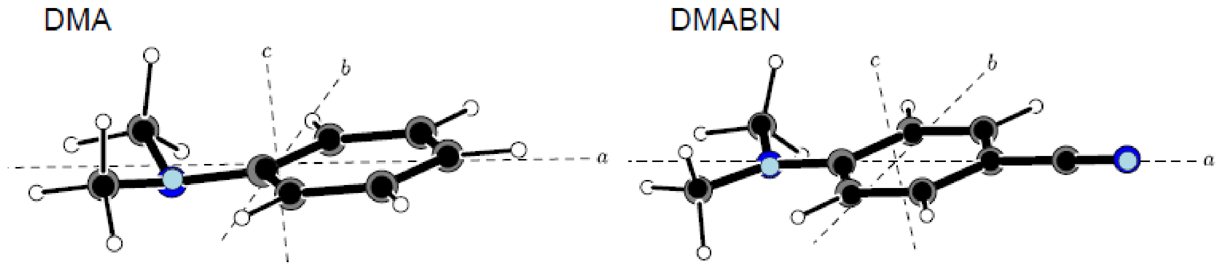

Figure 4.6. Substitution structures of DMA and DMABN (small circles), compared to *ab initio* structures calculated at an MP2/6-31+G(d) level of theory (large circles) for DMA and M052x/6-31G(d) for DMABN. The diameter of the *ab initio* atom positions is 0.45 Å, while the diameter of the experimental atom positions is 0.30 Å.

Importantly, no methyl torsional splittings were observed in any of the microwave spectra of DMA and DMABN. Primarily, this is a consequence of the large barriers to internal rotation of the methyl groups, estimated to be greater than 500 cm^{-1} in the ground state of DMABN.[5] Splittings of less than 50 kHz would not be resolved in our spectrum, owing to the observed linewidths on the order of 100 kHz.

4.5 DISCUSSION

Nuclear quadrupole coupling constants are exquisitely sensitive to the local electronic environment. To get some impression of this environment, a comparison to a control molecule needs to be made. For this, we chose aniline (AN) owing to the fact that it is the simplest analog of both DMA and DMABN and has been thoroughly researched by other workers.[18,20,21]

A comparison of the ^{14}N couplings in these three molecules requires a transformation of the measured inertial-axis frame values into the frame defined by the coupling tensor of each nitrogen nucleus (χ), as the inertial tensors and the quadrupole tensors are not coaxial. However, all three molecules have a plane of symmetry (C_s); hence, it is reasonable to assume that the tensor axes perpendicular to this plane are parallel. In that event, the transformation is a simple rotation by some angle θ about the *b* inertial axis, described by the equations

$$\chi_{xx} = \frac{\chi_{aa}\cos^2\theta - \chi_{cc}\sin^2\theta}{\cos^2\theta - \sin^2\theta} \tag{4.4}$$

$$\chi_{yy} = \chi_{bb} \tag{4.5}$$

$$\chi_{zz} = \frac{\chi_{aa}\,sin^2\,\theta - \chi_{cc}\cos^2\theta}{\sin^2\theta - \cos^2\theta} \tag{4.6}$$

Here, *x*, *y*, and *z* are the principal axes of the amino nitrogen quadrupole tensor, and θ is the angle of rotation about *b*; see Figure 4.7. In this work, since the off-diagonal values of χ in the inertial coordinate system were not measured, values of θ were determined from the calculated energy-optimized geometries of the three species using the program QTRANS.[22]

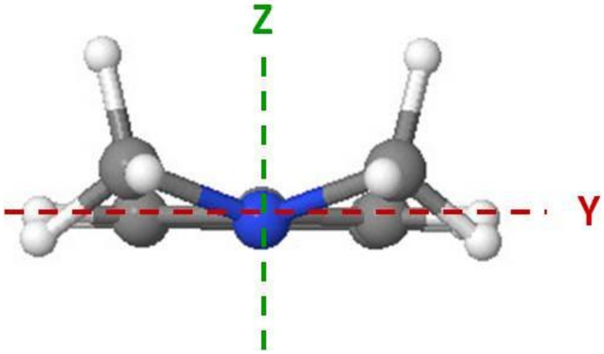

Figure 4.7. N-14 Quadrupole tensor coordinates

The results of these transformations are listed in Table 4.3. Comparison of the elements of the ^{14}N amino quadrupole tensors of the three molecules shows that χ_{xx} decreases slightly, χ_{yy} increases, and χ_{zz} decreases across the series. These changes are a direct result of the replacement of the hydrogens in aniline with methyl groups in DMA and DMABN *via* hyperconjugative effects.[23] The mechanism of such effects is well known.[24] In the particular cases of DMA and DMABN, a π-type molecular orbital can be formed from a linear combination of the three hydrogen atom 1s orbitals of the attached methyl groups, providing direct overlap with the lone pair orbital on the nitrogen atom. Donation of electrons from the methyl groups to the nitrogen results. A fully localized lone pair on nitrogen would give values of χ_{xx} = 2.50, χ_{yy} = 3.75, and χ_{zz} = - 6.25 MHz.[21] Note that the value of χ_{zz} in DMABN is slightly less negative than in DMA owing to additional ring-mediated conjugative interactions with the cyano group.

Table 4.3. Amine quadrupole coupling constants in aniline, DMA, and DMABN

Parameter	Aniline (Ref. 21)	DMA	DMABN
θ (degrees)	13.3[a]	3.6[a]	2.8[a]
χ_{xx} (MHz)	2.72	2.61	2.56
χ_{yy}(MHz)	1.86	2.80	2.8
χ_{zz}(MHz)	-4.59	-5.41	-5.35
Inversion Angle (deg)	37.5	35.5[b]	10.1[b]

[a] Calculated using QTRANS (Ref. [22]).
[b] Calculated from Gaussian structures.

A similar treatment was used for the cyano nitrogen atom in DMABN. The quadrupole constants of DMABN, benzonitrile[8] and ethyl cyanide[25] are summarized in Table 4.4. (Here, we assume that the quadrupole and inertial tensors are coincident.) Compared to ethyl cyanide, χ_{aa} (~χ_{zz}) decreases, χ_{bb} (~χ_{xx}) increases, and χ_{cc} (~χ_{yy}) decreases in benzonitrile and DMABN, all a consequence of increases in the lone pair density around the nitrogen atom in the plane of the ring.

Table 4.4. Nitrile quadrupole coupling constants in DMABN, benzonitrile and ethyl cyanide

Parameter	DMABN	Benzonitrile (Ref. 8)	Ethyl Cyanide (Ref. 26)[a]
χ_{aa} (MHz)	-4.11(30)	-4.23738(36)	-3.309(33)
χ_{bb} (MHz)	2.40(13)	2.2886(11)	1.265(13)
χ_{cc} (MHz)	1.71(13)	1.9488(11)	2.044(20)

[a] Expressed in the molecular coordinate system, these values are χ_{xx} = - 4.171, χ_{yy} = 2.127, and χ_{zz} = 2.044 MHz.

The *p*-orbital populations of the amino nitrogens in aniline, DMA, and DMABN may be determined using a method originally described by Townes and Dailey.[26] The relevant equations for an sp^3-hybridized nitrogen atom are:[19]

$$i_\sigma(NX) = \frac{\cos\varphi}{\cos\varphi - 1} = a \tag{4.7}$$

$$\chi_{xx} - \chi_{zz} = 3a[i_\sigma(NX) - i_\sigma(NC)]\chi_{210} \tag{4.8}$$

$$\frac{\chi_{yy}}{\chi_{210}} = \frac{[1-(1-a)(i_\sigma(NX))-a(i_\sigma(NC)-\pi_c]}{[1+.3(2i_\sigma(NX)+i_\sigma(NC)-\pi_c)]} \tag{4.9}$$

Here, the angle φ is the angle between the two equivalent sp^3-orbitals which was determined from the Kraitchman structures by measuring the angle between the two N-X bonds, where X is H or CH_3 (Tables 4.9 and 4.10). The quantities $\boldsymbol{i}_\sigma$(NX) and $\boldsymbol{i}_\sigma$(NC) are the ionic characters of the N-X and N- C_φ sigma bonds and π_c is the π-character of the N-C_φ bond. Once these characters were determined from Eqs. (4.7-4.9), the orbital occupancies follow immediately from Eqs. (4.10-4.12):

$$N_x = 1 + \frac{1}{2}[i_\sigma(NX) + i_\sigma(NC)] \tag{4.10}$$

$$N_y = 1 + i_\sigma(NX) \tag{4.11}$$

$$N_z = 2 - \pi_c \tag{4.12}$$

The results of these calculations are listed in Table 4.5. When comparing the orbital occupancy numbers of DMA and DMABN with aniline, a small increase in N_z is observed. This increase corresponds to an increase in the electronic density in the lone pair of the amino nitrogen. At the same time, the π-character of the N-C_φ bonds decreases smoothly from 0.19 to 0.12 to 0.09 across the series AN, DMA, and DMABN. However, there is no corresponding increase in N_x or N_y. This further supports the idea that the methyl groups are donating electron density into the lone pair π-orbital of the –$N(CH_3)_2$ groups through hyperconjugation. Apparently, this effect is amplified by the presence of the –CN group in the *para* position of the ring in DMABN, compared to DMA. This increase in the lone pair density in the two molecules is indicative of a build-up of charge and can be thought of as a precursor to charge-transfer.

Table 4.5. *p*-Orbital occupation numbers in aniline, DMA, and DMABN

Parameter	Aniline (Ref. 20)	DMA	DMABN
φ (degrees)	113.1	114.7[a]	118.0[a]
$i_\sigma(NX)$, X= H, CH_3	0.28	0.30	0.32
$i_\sigma(NC)$	0.37	0.28	0.30
π_c	0.19	0.12	0.09
N_x	1.33	1.28	1.31
N_y	1.28	1.30	1.32
N_z	1.81	1.88	1.91

[a] Determined from Kraitchman analyses of isotopologs (12 for DMA, 13 for DMABN); see Supplementary Information.

One further observation is worthy of note. In the Kraitchman structure of DMA (Figure 4.6), the nitrogen lies below the ring and the methyl groups lie above the ring, resulting in an inversion angle of 30.0° (Cervellati *et al.*[7] estimated this angle to lie between 27-30°). This angle is only slightly smaller than that found in aniline, 37.5°.[18] Now, Kydd[27] had noted many years ago that the inversion angle of ring-substituted anilines scaled approximately linearly with the inversion barriers. Aniline has an inversion barrier of 525 cm^{-1} [28,29]. Thus, we expect significantly smaller barriers in DMA and DMABN, in view of their measured inversion angles. Confirming this expectation, the observed inversion splitting in DMA ($\Delta E = 1.92\ cm^{-1}$) can be fit using a harmonic potential with a Gaussian barrier of ~90 cm^{-1}. The corresponding barrier in DMABN (for which the inversion angle is 14.6°) must be significantly smaller.[30]

Our results show that N_z (the lone pair density on the amino nitrogen) increases smoothly from 1.81 to 1.88 to 1.91 across the series; while the π-character of the $N\text{-}C_{\Phi}$ bond decreases from 0.19 to 0.12 to 0.09, as noted above. Thus, substitution of the H atoms of the $-NH_2$ group with CH_3 groups and the addition of a cyano group to the ring shifts the π-electron density from the $N\text{-}C_{\Phi}$ bond to the lone pair of the $-N(CH_3)_2$ group, flattening it towards an sp^2 structure, and substantially reducing the barrier to inversion.

4.6 ACKNOWLEDGEMENTS

This research has been supported by NSF (CHE-0618740 and CHE-0960074). We thank Dr. William C. Bailey of Kean University for his assistance with the quadrupole calculations. We dedicate this work to the memory of a friend and colleague, Dr. David O. Harris of the University of California, Santa Barbara.

4.7 REFERENCES

(1) Lippert, E.; Luder, W.; Boos, H. *Advances in Molecular Spectroscopy; European Conference on Molecular Spectroscopy, Bologna, Italy, 1959* **1962**, 443-457.

(2) Lippert, E.; Luder, W.; Moll, F.; Nagele, W.; Boos, H.; Prigge, H.; Seibold-Blankenstein, I. *Angew. Chem.* **1961**, *73*, 695-706.

(3) Rotkiewicz, K.; Grellmann, K. H.; Grabowski, Z. R. *Chem. Phys. Lett.* **1973**, *19*, 315-318.

(4) Saigusa, H.; Miyakoshi, N.; Mukai, C.; Fukagawa, T.; Kohtani, S.; Nakagaki, R.; Gordon, R. *J. Chem. Phys.* **2003**, *119*, 5414-5422.

(5) Nikolaev, A. E.; Myszkiewicz, G.; Berden, G.; Meerts, W. L.; Pfanstiel, J. F.; Pratt, D. W. *J. Chem. Phys.* **2005**, *122*, 1-10.

(6) Kajimoto, O.; Yokoyama, H.; Ooshima, Y.; Endo, Y. *Chem. Phys. Lett.* **1991**, *179*, 455-459.

(7) Cervellati, R.; Borgo, A. D.; Lister, D. G. *J. Mol. Struct.* **1982**, *78*, 161-167.

(8) Wohlfart, K.; Schnell, M.; Grabow, J. U.; Kuepper, J. *J. Mol. Spectrosc.* **2008**, *247*, 119-121.

(9) Brown, G. G.; Dian, B. C.; Douglass, K. O.; Geyer, S. M.; Pate, B. H. *J. Mol. Spectrosc.* **2006**, *238*, 200-212.

(10) Brown, G. G.; Dian, B. C.; Douglass, K. O.; Geyer, S. M.; Shipman, S. T.; Pate, B. H. *Rev. Sci. Instrum.* **2008**, *79*, 053103.

(11) Plusquellic, D. F.; Suenram, R. D.; Mate, B.; Jensen, J. O.; Samuels, A. C. *J. Chem. Phys.* **2001**, *115*, 3057-3067.

(12) Pickett, H. M. *J. Chem. Phys.* **1997**, *107*, 6732-6735.

(13) Pickett, H. M. *J. Chem. Phys.* **1972**, *56*, 1715-1723.

(14) Pickett, H. M. *J. Mol. Spectrosc.* **1991**, *148*, 371-377.

(15) Shipman, S. T.; Alvarez-Valtierra, L.; Neill, J. L.; Pate, B. H.; Lessari, A.; Kisiel, Z. In *OSU International Symposium on Molecular Spectroscopy* Columbus, Ohio, 2008.

(16) Neill, J. L.; Pate, B. H. *in preparation*.

(17) Frisch, M. J.; Trucks, G. W.; Schlegel, H. B.; Scuseria, G. E.; Robb, M. A.; Cheeseman, J. R.; Montgomery, J. A. J.; Vreven, T.; Kudin, K. N.; Burant, J. C.; Millam, J. M.; Iyengar, S. S.; Tomasi, J.; Barone, V.; Mennucci, B.; Cossi, M.; Scalmani, G.; Rega, N.; Petersson, G. A.; Nakatsuji, H.; Hada, M.; Ehara, M.; Toyota, K.; Fukuda, R.; Hasegawa, J.; Ishida, M.; Nakajima, T.; Honda, Y.; Kitao, O.; Nakai, H.; Klene, M.; Li, X.; Knox, J. E.; Hratchian, H. P.; Cross, J. B.; Bakken, V.; Adamo, C.; Jaramillo, J.; Gomperts, R.; Stratmann, R. E.; Yazyev, O.; Austin, A. J.; Cammi, R.; Pomelli, C.; Ochterski, J. W.; Ayala, P. Y.; Morokuma, K.; Voth, G. A.; Salvador, P.; Dannenberg, J. J.; Zakrzewski, V. G.; Dapprich, S.; Daniels, A. D.; Strain, M. C.; Farkas, O.; Malick, D. K.; Rabuck, A. D.; Raghavachari, K.; Foresman, J. B.; Ortiz, J. V.; Cui, Q.; Baboul, A. G.; Clifford, S.; Cioslowski, J.; Stefanov, B. B.; Liu, G.; Liashenko, A.; Piskorz, P.; Komaromi, I.; Martin, R. L.; Fox, D. J.; Keith, T.; Al-Laham, M. A.; Peng, C. Y.; Nanayakkara, A.; Challacombe, M.; Gill, P. M. W.; Johnson, B.; Chen, W.; Wong, M. W.; Gonzalez, C.; Pople, J. A. **2004**.

(18) Lister, D. G.; Tyler, J. K.; Høg, J. H.; Larsen, N. W. *J. Mol. Struct.* **1974**, *23*, 253-264.

(19) Gordy, W.; Cook, R. L. *Microwave Molecular Spectra*; 3rd ed.; Wiley-Interscience: New York, 1984.

(20) Hatta, A.; Suzuki, M.; Kozima, K. *Bull. Chem. Soc. Jpn.* **1973**, *46*, 2321-3.

(21) Kleiboemer, B.; Sutter, D. H. *Z. Naturforsch., A: Phys. Sci.* **1988**, *43*, 561-71.

(22) Bailey, W. C. Calculation of Nuclear Quadrupole Coupling Constants in Gaseous State Molecules, http://homepage.mac.com/wcbailey/nqcc/index.html.

(23) Mulliken, R. S. *J. Chem. Phys.* **1939**, *7*, 339-352.

(24) Carrington, A.; McLachlan, A. D. *Introduction to Magnetic Resonance*; Harper & Row: New York, 1967.

(25) Li, Y. S.; Harmony, M. D. *J. Chem. Phys.* **1969**, *50*, 3674-3677.

(26) Townes, C. H.; Dailey, B. P. *J. Chem. Phys.* **1949**, *17*, 782-796.

(27) Kydd, R. A. *Spectrochim. Acta, Pt. A: Mol. Spectrosc.* **1979**, *35*, 409-413.

(28) Kydd, R. A.; Krueger, P. J. *Chem. Phys. Lett.* **1977**, *49*, 539-543.

(29) Larsen, N. W.; Hansen, E. L.; Nicolaisen, F. M. *Chem. Phys. Lett.* **1976**, *43*, 584-586.

(30) Antoine, R.; Abd El Rahim, M.; Broyer, M.; Rayane, D.; Dugourd, P. *J. Phys. Chem. A* **2006**, *110*, 10006-10011.

4.8 SUPPLEMENTARY MATERIALS

Table 4.6. Fit rotational constants of singly substituted isotopomers of the 0^+ level of N,N'-dimethylaniline.

Species	A (MHz)	B (MHz)	C (MHz)	N_{lines}	rms error (kHz)
Normal Species	3500.175(25)	1266.6668(5)	923.3514(7)	62	9.8
$^{13}C_1$	3500.09(6)	1226.5473(11)	923.3005(12)	27	16.5
$^{13}C_2/^{13}C_6$	3465.44(3)	1225.9626(6)	920.5284(7)	41	13.1
$^{13}C_3/^{13}C_5$	3466.38(3)	1216.1753(7)	915.0574(7)	47	15.5
$^{13}C_4$	3500.17(4)	1206.9686(8)	912.1592(9)	32	13.2
^{15}N	3499.350(17)	1218.8696(4)	919.0233(3)	20	5.7
$^{13}C_7/^{13}C_8$	3464.61(4)	1210.6303(7)	911.8317(8)	40	14.2

Table 4.7. Fit rotational constants of singly substituted isotopomers of the 0^+ level of DMABN.

Species	A (MHz)	B (MHz)	C (MHz)	N_{lines}	rms error (kHz)
Normal Species	3469.23(10)	578.5848(9)	499.6095(10)	85	24.7
$^{13}C_1$	3469.05(10)	577.8908(5)	499.0957(5)	66	26.1
$^{13}C_2/^{13}C_6$	3434.76(10)	578.5327(5)	498.8527(5)	51	23.7
$^{13}C_3/^{13}C_5$	3435.19(8)	577.8242(4)	498.3313(4)	65	24.9
$^{13}C_4$	3469.33(9)	576.4877(4)	498.0476(4)	64	25.2
^{15}N	3469.32(7)	574.7927(3)	496.7911(3)	57	18.5
$^{13}C_7/^{13}C_8$	3433.24(9)	572.1498(5)	494.0711(4)	70	27.4
$^{13}C_9$	3469.29(9)	571.8089(5)	494.5485(4)	58	26.9
$^{15}N_2$	3469.30(9)	566.2548(4)	490.3885(4)	56	24.7

Table 4.8. Global fit of DMA microwave parameters determined using both 6-18 and 25-40 GHz spectra.

Parameters	This Work
$A(0^+)$ (MHz)	3500.145(15)
$B(0^+)$ (MHz)	1226.6650(10)
$C(0^+)$ (MHz)	923.34844(78)
$A(0^-)$ (MHz)	3500.931(23)
$B(0^-)$ (MHz)	1226.6430(11)
$C(0^-)$ (MHz)	923.60464(91)
χ_{aa} (MHz)	2.592(28)
χ_{bb} (MHz)	-2.825(10)
χ_{cc} (MHz)	-5.418(10)
Δ_J (kHz)	0.0319(11)
Δ_{JK} (kHz)	0.054(15)
δ_J (kHz)	0.00757(81)
δ_K (kHz)	0.076(31)
F_{ac} (MHz)	2.352(10)
ΔE (MHz)	57607.956(49)
N_{lines}	196
rms error (kHz)	28.3

Table 4.9. Heavy-atom substitution coordinates of the 0^+ level of N,N'-dimethylaniline.

Atom	|*a*| (Å)	|*b*| (Å)	|*c*| (Å)
C_1	0.183(9)	[0][a]	0.082(20)
C_2/C_6	0.484(3)	1.2054(13)	0.05(3)
C_3/C_5	1.8845(9)	1.1975(14)	[0][a]
C_4	2.5986(6)	[0][b]	0.065(24)
N	1.6182(9)	[0][b]	0.216(7)
C_7/C_8	2.3327(7)	1.2276(13)	0.113(14)

[a] Undetermined value.

Table 4.10. Heavy-atom substitution coordinates of DMABN.

Atom	|*a*| (Å)	|*b*| (Å)	|*c*| (Å)
C_1	1.0223(22)	[0][a]	0.087(25)
C_2/C_6	0.275(8)	1.2100(19)	0.05(4)
C_3/C_5	1.074(3)	1.205(3)	[0][a]
C_4	1.7854(19)	[0][a]	[0][a]
N_1	2.4102(8)	[0][a]	0.101(21)
C_7/C_8	3.1356(5)	1.2438(13)	0.078(28)
C_9	3.2234(11)	[0][a]	[0][a]
N_2	4.3830(8)	[0][a]	[0][a]

[a] Undetermined value.

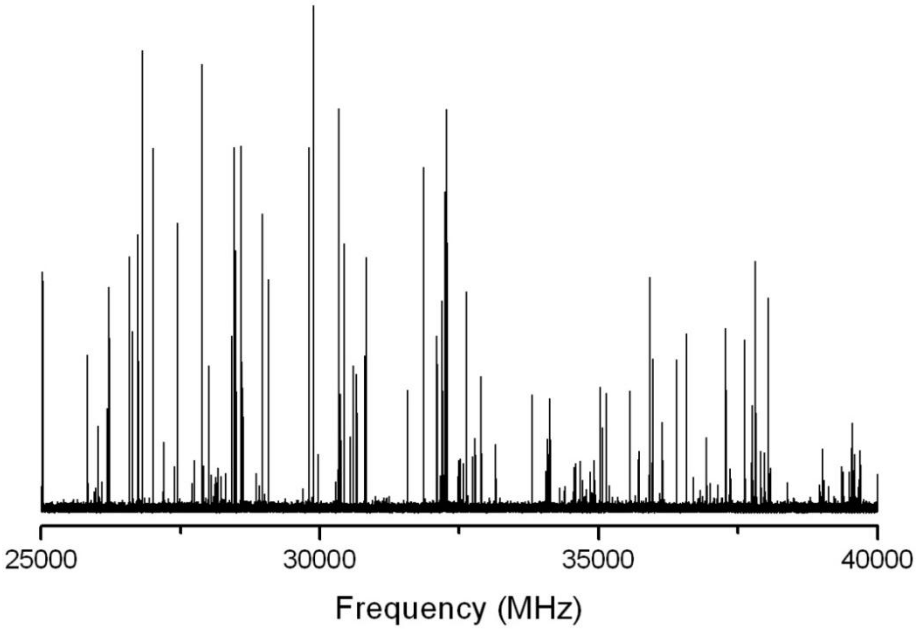

Figure 4.8. Microwave spectrum of DMA from 25 to 40 GHz, collected using 1.15 million pulses.

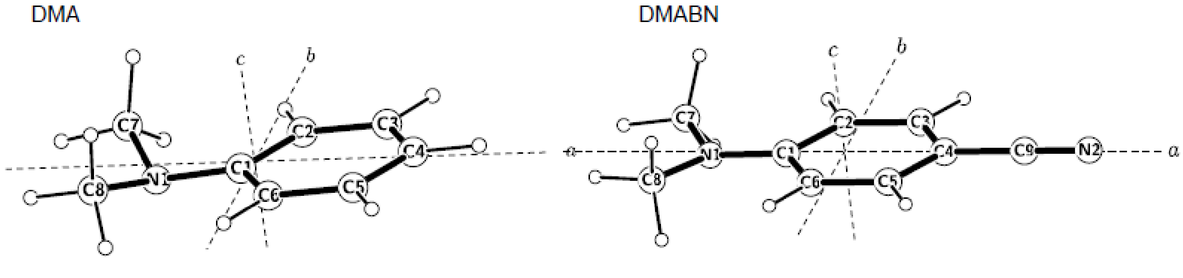

Figure 4.9. Atom labels for DMA and DMABN.

5.0 METHYL ROTORS IN THE GAS PHASE: A STUDY OF *o*- AND *m*-TOLUIDINE BY CHIRPED-PULSE FOURIER TRANSFORM MICROWAVE SPECTROSCOPY

This work was published in and is reproduced with permission from
J. Mol. Spectrosc. **2011**, *266*, 81.

R.G. Bird performed the experimental measurements, analyzed the spectra and wrote the paper.

5.1 ABSTRACT

Microwave spectra of *o*- and *m*-toluidine were recorded in a pulsed supersonic jet using chirped pulse techniques. The spectra show both torsional and ^{14}N quadrupole splittings at high resolution. From the torsional splittings, barrier heights were determined of 531 cm^{-1} and 2.0 cm^{-1}, respectively. Using the quadrupole splittings, orbital occupancy numbers of the amino-nitrogen atoms were calculated. An apparent relationship between these values and the barriers to internal rotation of the methyl groups is discussed.

5.2 INTRODUCTION

Recently, Plusquellic[1] showed that the torsional barriers of methyl groups attached to small peptides differ considerably from one molecule to the next, and even depend upon the position of substitution. Here, we explore the origins of these effects by using chirped-pulse Fourier transform microwave (CP-FTMW) spectroscopy to determine the torsional barriers of two methyl-substituted anilines. *Ortho*- and *meta*-toluidines were previously studied by vibrationally[2] and rotationally[3] resolved electronic spectroscopy. However, due to the resolution and spectral fitting limitations, there are inherent difficulties when attempting to accurately determine small barriers (<10 cm^{-1}) or large barriers (>500 cm^{-1}) in molecules of this type. CP-FTMW can potentially overcome these problems, due to its higher resolution and numerous spectral fitting programs.

Currently, numerous fitting programs that specialize in different types of methyl rotors exist. A recent review by Kleiner[4] describes these programs along with some of their advantages and disadvantages. In the case of *o*- and *m*-toluidine, three different programs were used; Plusquellic's JB95,[5] Hartwig's XIAM,[6] and Kleiner's BELGI.[7] For our purposes, JB95 was first used to fit the rigid-rotor A-bands of both conformers and then used for its spectral viewing capabilities to help with the assignments for the other two programs. In the case of *o*-toluidine, XIAM was used to fit both the quadrupole coupling and the methyl rotor, while BELGI was used for *m*-toluidine. The quadrupole coupling constants of the nitrogen atoms of both toluidines give information about the local electronic environments, which in turn may be related to the observed barrier heights.[8, 9]

Adding methyl groups to DNA attracts repressive DNA-binding proteins to it and may also cause the region to compact even further, making it inaccessible to proteins that make RNA from DNA.[10] Therefore, knowledge of the preferred orientation of such groups and their barriers to internal rotation could be biologically important.

5.3 EXPERIMENTAL

Figure 5.1 shows a block diagram of the chirped-pulse Fourier transform microwave (CP-FTMW) spectrometer used in this work. Conceptually, it resembles the broadband instrument developed by the Pate group,[11, 12] but it employs a significantly narrower pulse (500 MHz) and a lower power amplifier (1 W). To offset the power loss, one of the horns was replaced by a mirror to improve the cavity Q. This improvement made it possible to record 500 MHz portions of the spectrum with good signal-to-noise ratio (20:1) at a significantly reduced cost.

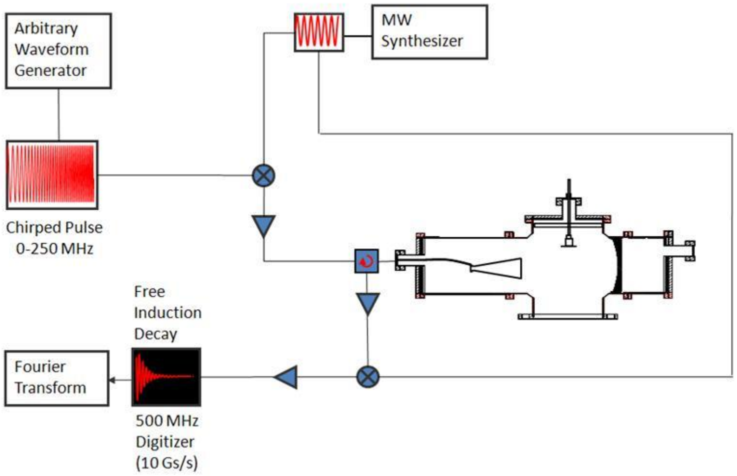

Figure 5.1. Schematic of the broadband CP-FTMW cavity setup. The microwave horn transmits and detects the signal, while the mirror enhances the power stored in the cavity.

Ortho and *meta*-toluidine were purchased from Sigma-Aldrich and used without further purification. *o*-Toluidine was heated to 60 °C and expanded through a pulsed nozzle at 10 Hz with 1.5 bar He backing gas while *m*-Toluidine was heated to 75 °C and backed with 0.5 bar He. The nozzle was placed perpendicular to the microwave signal axis. The spectra of both molecules were taken between 6.5 and 17.5 GHz in 450 MHz segments, collecting a 10 μs FID and signal averaging for up to 10,000 shots. The segments were then patched together and analyzed using JB95[5], XIAM[6], and BELGI[7]. To improve the fit of both, a more powerful 10 MHz chirped pulse was used to help increase the signal of low intensity $\Delta F = 0$ transitions and a 40 μs FID was collected resulting in better resolution.

5.4 RESULTS

The microwave spectrum of *o*-toluidine from 6-18 GHz is shown in Figure 5.2. The spectrum is made up of μ_a- and μ_b-type R-branch transitions. Each of these transitions is split into several components owing to the combined effects of torsional and nuclear quadrupole effects. As shown in the second half of Figure 5.2, these combined effects result in two separate splitting patterns, where the large splittings are caused by the nuclear quadrupole coupling and the small splittings are caused by the torsional motions of the methyl group. It can be seen from the splitting pattern of the $3_{12} \leftarrow 2_{11}$ transition that the perturbations are of the same order of magnitude.

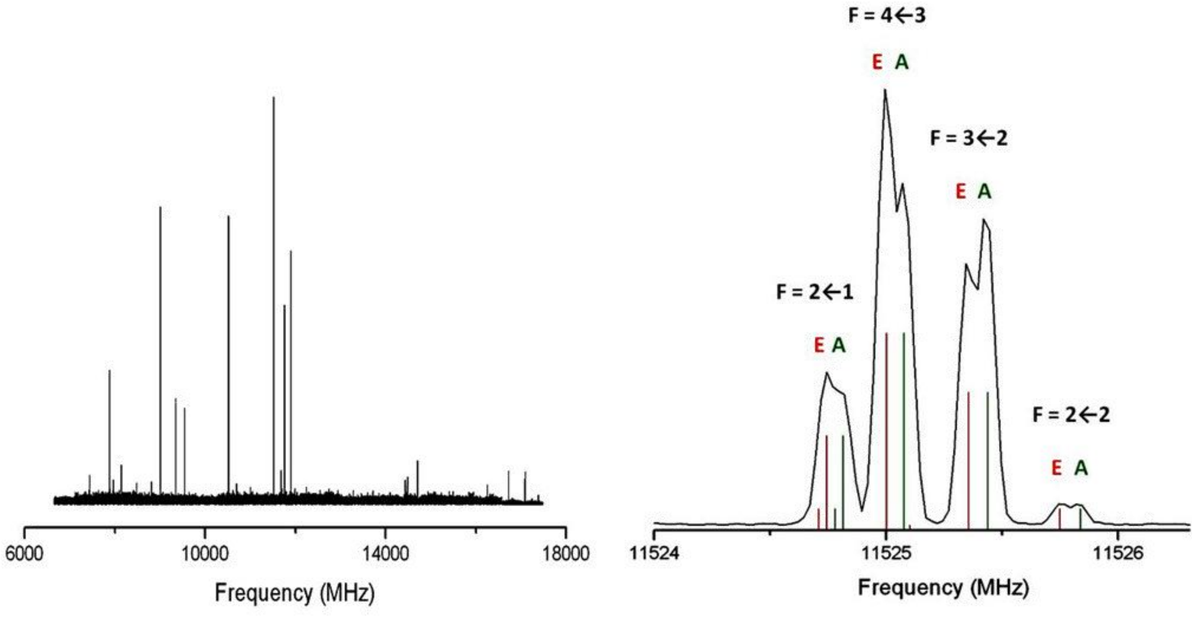

Figure 5.2. (Left) Microwave spectrum of *o*-toluidine from 6 to 18 GHz, collected using 10,000 450 MHz chirped pulses. (Right) Hyperfine splitting of the two torsional subbands [E (red) and A (green)] of the $3_{12} \leftarrow 2_{11}$ transition collected using 10,000 10 MHz chirped pulses.

The Hamiltonian of a rotating molecule that is experiencing these additional interactions can be written as:

$$\hat{H} = \hat{H}_{ROT} + \hat{H}_{TOR} + \hat{H}_{QUAD} + \hat{H}_{INT} \tag{5.1}$$

where $\hat{H}_{ROT}$, $\hat{H}_{TOR}$, and $\hat{H}_{QUAD}$ are the rotational, torsional, and nuclear quadrupole Hamiltonians and $\hat{H}_{INT}$ is the interaction among them. In the case of *o*-toluidine, the splitting patterns show that $\hat{H}_{ROT} \gg \hat{H}_{QUAD} \approx \hat{H}_{TOR}$. The small torsional perturbation is indicative of a large barrier and for that reason XIAM was chosen to fit the spectrum. XIAM allows for the simultaneous fitting of both quadrupole and torsional terms, resulting in a more accurate determination of the experimental parameters. These parameters are listed in Table 5.1. The observed methyl rotor barrier is 531 cm^{-1}, and the angle between the rotor axis and the *a* inertial axis is δ=0.67 rad. The observed barrier height is significantly different from previous results on *o*-toluidine[2,3,13] which, due to resolution limitations, relied on calculations to determine the barrier height. Initial estimates of all parameters were obtained from an *ab initio* calculation and show reasonable agreement with experimental results.[14]

The microwave spectrum of *m*-toluidine, shown in Figure 5.3, consists of μ_a- and μ_b-type R-branch transitions, similar to *o*-toluidine. Each transition is split into two components by the larger torsional interactions and then split again by the smaller quadrupole interactions. This pattern is representative of a small barrier to methyl group internal rotation where now $\hat{H}_{ROT} \approx \hat{H}_{TOR} \gg \hat{H}_{QUAD}$. XIAM fails to accurately predict E states for low barrier rotors.[4] Therefore, BELGI was employed to fit the spectrum of *m*-toluidine; the results are listed in Table 5.2. The determined barrier height is 1.97 cm^{-1}. The parameters ρ and D_{ab} describe the coupling between internal and overall rotation and the off-diagonal quadratic rotational constants,

Table 5.1. Experimental parameters for *o*-toluidine obtained from a fit of the CP-FTMW spectrum to Eq. (5.1) using XIAM

	Experimental	Electronic (Ref [3])	mp2/6-31+g(d)[a]
A (MHz)	3230.30(1)	3230.9(1)	3227.85
B (MHz)	2188.818(2)	2189.0(1)	2178.171
C (MHz)	1316.931(1)	1316.9(1)	1313.307
χ_{aa} (MHz)	2.01(1)		1.78[b]
χ_{bb} (MHz)	2.05(3)		2.10[b]
χ_{cc} (MHz)	-4.06(3)		-3.89[b]
V_3 (cm^{-1})	531(7)	703 (Ref [2])	680[c]
Delta (rad)	0.67(6)		
F_0	157.67		
ΔI (u Å^2)	-3.59	-3.53	-3.77
N_{lines}	155		

[a] Calculated using Gaussian mp2/6-31+g(d)
[b] Calculated from the optimized structure using Gaussian b3pw91/6-311+g(df,pd)
[c] Calculated using Gaussian mp2/6-311+g(d,p)

BELGI does not incorporate quadrupole coupling into the calculation. To overcome this, JB95 was used to determine the quadrupole splittings of the rigid rotor-like A-band. The A and E-band unsplit frequencies were then determined from splitting patterns calculated by JB95 to fit the rotational constants. The difference in the A and E-band quadrupole moments was assumed to be less than experimental error.

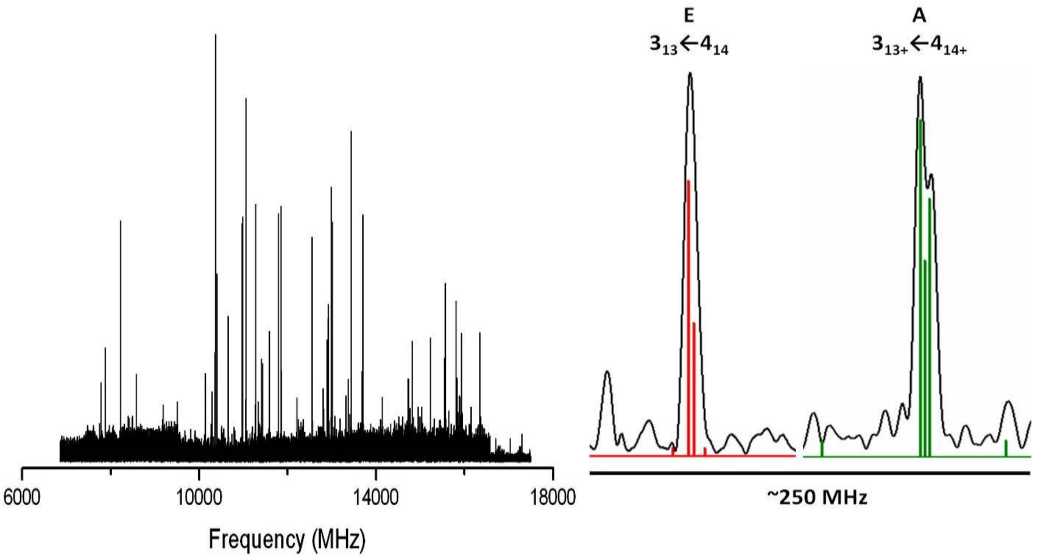

Figure 5.3. (Left) Microwave spectrum of *m*-toluidine from 6 to 18 GHz, collected using 10,000 450 MHz chirped pulses. (Right) Hyperfine splitting of the $4_{14} \leftarrow 3_{13}$ (E) and $4_{14+} \leftarrow 3_{13+}$ (A) transitions separated by around 250 MHz. Both transitions are identified using the J,Ka,Kc,parity distinctions described by BELGI (Ref. 7).

Table 5.2. Experimental parameters for *m*-toluidine obtained from a fit of the CP-FTMW spectrum to Eq. (5.1) using BELGI.

	Experimental	Electronic (Ref 3)	mp2/6-31+g(d)[a]
A (MHz)	3502.95(2)	3701.3(1)	3621.178
B (MHz)	1923.685(6)	1795.9(1)	1788.994
C (MHz)	1210.334(3)	1210.4(1)	1206.43
χ_{aa} (MHz)	2.18(5)[b]		2.68[c]
χ_{bb} (MHz)	2.05(5)[b]		2.49[c]
χ_{cc} (MHz)	-4.23(5)[b]		-5.15[c]
V_3 (cm^{-1})	1.97(5)	9.45 (Ref 3)	5.4[d]
ρ	0.021101(3)		
D_{ab} (MHz)	476.573(8)		
ΔI (u Å^2)	10.57	-0.42	-3.15
N_{lines}	53		

[a] Calculated using Gaussian mp2/6-31+g(d)
[b] Determined from the A-band using JB95
[c] Calculated from the optimized structure using Gaussian b3pw91/6-311+g(df,pd)
[d] Calculated using Gaussian m052x/6-311+g(d)

The barrier height determined in this work (V_3 = 1.97 cm^{-1}) is significantly smaller than that determined using high resolution electronic spectroscopy (V_3 = 9.45 cm^{-1}). Primarily, this difference may be attributed to differences in the Hamiltonians needed to fit the spectra; Morgan, *et al.*[3] used the perturbative "Principal Axis Method" that is most appropriate for high barrier rotors.[4]

5.5 DISCUSSION

Nuclear quadrupole coupling constants are exquisitely sensitive to the local electronic environment. For example, ring nitrogens carrying hydrogen atoms, as in pyrrole, exhibits very different ^{14}N quadrupole couplings than ring nitrogens not attached to hydrogens, as in pyridine, because the nitrogen lone pair of electrons is perpendicular to the plane of the ring, rather than lying in the plane.[15] Substituent groups carrying nitrogens, such as the NH_2-group in aniline, have (nearly) perpendicular lone pairs, but delocalization of these into the π-electron system of the ring is not uniform, and will affect the magnitude of the torsional barrier of attached CH_3-groups. Thus, comparison of the ^{14}N coupling of *o*- and *m*-toluidine will provide information that can be used to explain the large difference in their V_3 values.

In what follows, we assume that the nitrogen atom in aniline in sp^3-hybridized, to be consistent with earlier work on this molecule.[16] To obtain the relevant orbital population, the measured quadrupole couplings of *o*- and *m*-toluidine were first rotated from the inertial coordinate system (about the *c*-axis for *o*- and *m*-toluidine and about the *b*-axis for aniline) into the localized coordinate system of the attached nitrogen atom (Fig. 5.4) using the energy optimized geometries of the three species. Since the off-diagonal values of quadrupole tensor in the inertial coordinate system were not measured, values of θ were determined from the calculated energy-optimized geometries of the three species using the program QTRANS.[17] Here, the angle φ is the angle between the two equivalent sp^3-orbitals which can be determined from the theoretical structure by measuring the angle between the two N-H bonds. Then, orbital occupation numbers were determined from these data using the Townes and Dailey approach.[18] The results of these calculations are listed in Table 5.3.

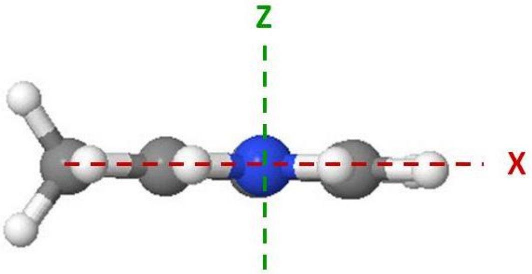

Figure 5.4. N-14 quadrupole tensor coordinates.

In Table 5.3, the quantities $\boldsymbol{i}_\sigma$(NH) and $\boldsymbol{i}_\sigma$(NC) are the ionic characters of the N-H and N-C sigma bonds and π_c is the π-character of the N-C π-bond, reflecting the population of the p_z-orbital on the nitrogen (N_z). Comparing the toluidines with aniline, we see that N_z is significantly less in *o*-toluidine than in aniline or *m*-toluidine (1.70 *vs.* 1.81 and 1.80). This decrease in the lone pair density on nitrogen may be attributed to hyperconjugation with the hydrogen atoms of the methyl group in the *ortho* position on the ring. Consistent with this view is the increase in π_c in *o*-toluidine (0.29) compared to the corresponding values of aniline (0.19) and *m*-toluidine (0.17). The N_x and N_y values of these two molecules are nearly identical, apart from some differences in the ionic character of their N-H and N-C bonds. It thus appears that there is very little direct interaction between the $–NH_2$ group and the $–CH_3$ group in *m*-toluidine.

These conclusions are largely confirmed by an examination of the calculated Mulliken charge distribution (Table 5.4 and Figure 5.5).

In addition to direct delocalization effects, the torsional barrier of a methyl group also depends on the difference in the π-characters of the two C-C bonds flanking the position of attachment of the methyl group to the ring. These differences can be quite large, especially in electronically excited states.[3] But in the ground state toluidines, these differences are small. Only in *o*-toluidine is there expected to be a difference in the π-character of the adjacent ring carbon bonds, C_1-C_2 and C_2-C_3, owing to the larger π-character of the N-C bond.

Table 5.3. *p*-Orbital occupational numbers in aniline, *o*-toluidine, and *m*-toluidine

	Aniline (Ref 16)	*o*-Toluidine	*m*-Toluidine
θ (degrees)	13.3	37[a]	58.7[a]
χ_{xx} (MHz)	2.72	2.10	2.26
χ_{yy}(MHz)	1.86	1.96	1.97
χ_{zz}(MHz)	-4.59	-4.07	-4.23
Φ (degrees)[b]	113.1[b]	109.6[b]	118.1[b]
i_σ(NH)	0.28	0.25	0.32
i_σ(NC)	0.37	0.23	0.29
π_c	0.19	0.29	0.17
N_x	1.33	1.24	1.30
N_y	1.28	1.25	1.32
N_z	1.81	1.70	1.83

[a] Calculated using QTRANS (Ref 22)
[b] Calculated from Gaussian structures.

Summarizing, CP-FTMW spectroscopy has been used to determine the CH_3-torsional barrier heights and orbital occupancies of the $–NH_2$ nitrogen atoms in *o*-and *m*-toluidine. Analysis of these data show an apparent direct relationship between the π-electron character of the N-C(ring) bond and the V_3 values; *o*-toluidine has $\pi_c = 0.29$ and $V_3 = 531$ cm^{-1}, whereas *m*-toluidine has $\pi_c = 0.17$ and $V_3 = 2$ cm^{-1}. A similar relationship apparently exist in the related molecules *o*- and *m*-tolunitrile (V_3 = 187 cm^{-1} and 14 cm^{-1}, respectively),[19,20] and *o*- and *m*-fluorotoluene (V_3 = 227 cm^{-1} and 14 cm^{-1}, respectively).[21, 22] Here, however, the two substituents withdraw electrons rather than donate them, deactivating the ring. The $–NH_2$ group, being activating, is expected to have a substantially larger effect, as observed.

5.6 ACKNOWLEDGMENTS

We thank Justin L. Neill and Dr. Brooks H. Pate of the University of Virginia for their help and for building our spectrometer. Additionally, we thank Z. Kisiel for his PROSPE website: http://info.ifpan.edu.pl/~kisiel/prospe.htm. This research has been supported by NSF (CHE-0618740 and CHE-0960074).

5.7 REFERENCES

(1) D. F. Plusquellic, D. W. Pratt, J. Phys. Chem. A 111 (2007) 7391-7397.

(2) K. Okuyama, K. Yoshihara, M. Ito, Laser Chem. 7 (1987) 197-212.

(3) P. J. Morgan, L. Alvarez-Valtierra, D. W. Pratt, J. Phys. Chem. A 113 (2009) 13221-13226.

(4) I. Kleiner, J. Mol. Spectrosc. 260 (2010) 1-18.

(5) D. F. Plusquellic, R. D. Suenram, B. Mate, J. O. Jensen, A. C. Samuels, J. Chem. Phys. 115 (2001) 3057-3067.

(6) H. Hartwig, H. Dreizler, Z. Naturforsch., A: Phys. Sci. 51 (1996) 923-932.

(7) J. T. Hougen, I. Kleiner, M. Godefroid, J. Mol. Spectrosc. 163 (1994) 559-586.

(8) Tan X. Q. Tan, W. A. Majewski, D. F. Plusquellic, D. W. Pratt, J. Chem. Phys. 94 (1991) 7721-7733.

(9) L. H. Spangler, Annu. Rev. Phys. Chem. 48 (1997) 481-510.

(10) B. Alberts, A. Jonson, J. Lewis, M. Raff, K. Roberts, P. Walter, Molecular Biology of the Cell, Garland Science, London, 2000.

(11) G. G. Brown, B. C. Dian, K. O. Douglass, S. M. Geyer, B. H. Pate, J. Mol. Spectrosc. 238 (2006) 200-212.

(12) G. G. Brown, B. C. Dian, K. O. Douglass, S. M. Geyer, S. T. Shipman, B. H. Pate, Rev. Sci. Instrum. 79 (2008) 053103.

(13) I. Kalkman, C. Vu, M. Schmitt, W. L. Meerts, Phys. Chem. Chem. Phys. 11 (2009) 4311-4318.

(14) M. J. Frisch, G. W. Trucks, H. B. Schlegel, G. E. Scuseria, M. A. Robb, J. R. Cheeseman, J. A. J. Montgomery, T. Vreven, K. N. Kudin, J. C. Burant, J. M. Millam, S. S. Iyengar, J. Tomasi, V. Barone, B. Mennucci, M. Cossi, G. Scalmani, N. Rega, G. A. Petersson, H. Nakatsuji, M. Hada, M. Ehara, K. Toyota, R. Fukuda, J. Hasegawa, M. Ishida, T. Nakajima, Y. Honda, O. Kitao, H. Nakai, M. Klene, X. Li, J. E. Knox, H. P. Hratchian, J. B. Cross, V. Bakken, C. Adamo, J. Jaramillo, R. Gomperts, R. E. Stratmann, O. Yazyev, A. J. Austin, R. Cammi, C. Pomelli, J. W. Ochterski, P. Y. Ayala, K. Morokuma, G. A. Voth, P. Salvador, J. J. Dannenberg, V. G. Zakrzewski, S. Dapprich, A. D. Daniels, M. C. Strain, O. Farkas, D. K. Malick, A. D. Rabuck, K. Raghavachari, J. B. Foresman, J. V. Ortiz, Q. Cui, A. G. Baboul, S. Clifford, J. Cioslowski, B. B. Stefanov, G. Liu, A.

Liashenko, P. Piskorz, I. Komaromi, R. L. Martin, D. J. Fox, T. Keith, M. A. Al-Laham, C. Y. Peng, A. Nanayakkara, M. Challacombe, P. M. W. Gill, B. Johnson, W. Chen, M. W. Wong, C. Gonzalez, J. A. Pople, (2004).

(15) L. D. Hatherley, R. D. Brown, P. D. Godfrey, A. P. Pierlot, W. Caminati, D. Damiani, S. Melandri, L. B. Favero, J. Phys. Chem. 97 (1993) 46-51.

(16) D. G. Lister, J. K. Tyler, J. H. Høg, N. W. Larsen, J. Mol. Struct. 1974, 23, 253-264.

(17) W. C. Bailey, Calculation of Nuclear Quadrupole Coupling Constants in Gaseous State Molecules, http://homepage.mac.com/wcbailey/nqcc/index.html.

(18) C. Tanjaroon, R. Subramanian, C. Karunatilaka, S. G. Kukolich, J. Phys. Chem. A 108 (2004) 9531-9539.

(19) N. Hansen, H. Mäder, T. Bruhn, Mol. Phys. 97 (1999) 587-595.

(20) T. Bruhn, H. Mäder, J. Mol. Struct. 200 (2000) 151-161.

(21) J. Susskind, J. Chem. Phys. 53 (1970) 2492-2501.

(22) H. D. Rudolph, A. Trinkaus, Z. Naturforsch., A: Astrophys., Phys. Phys. Chem. 23 (1968) 68-76.

5.8 SUPPLEMENTARY MATERIALS

Table 5.4. Mulliken charges on the heavy atoms in aniline, *o*-toluidine and *m*-toluidine

	Mulliken Charges[a]		
	Aniline	*o*-Toluidine	*m*-Toluidine
C1	0.341	-0.029	0.002
C2	-0.040	0.0886	-0.020
C3	0.102	-0.087	0.300
C4	-0.141	0.261	-0.243
C5	0.104	-0.428	-0.114
C6	-0.038	0.178	0.024
C7		0.303	0.458
N1	-0.329	-0.287	-0.310

[a] Calculated using Gaussian mp2/aug-cc-pvdz

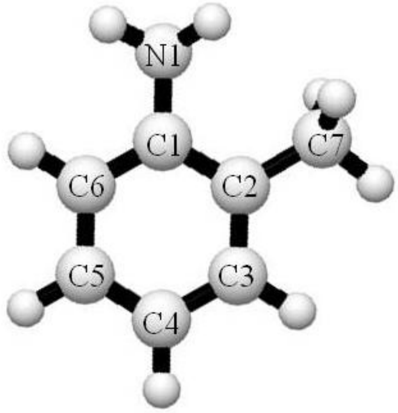

Figure 5.5. Atom labels for aniline, *o*-toluidine, and *m*-toluidine.

6.0 MICROWAVE AND UV EXCITATION SPECTRA OF 4-FLUOROBENZYL ALCOHOL AT HIGH RESOLUTION. S_0 AND S_1 STRUCTURES AND TUNNELING MOTIONS ALONG THE LOW FREQUENCY –CH_2OH TORSIONAL COORDINATE IN BOTH ELECTRONIC STATES

This work is accepted for publication in *J. Phys. Chem. A.* **2011**, 10.1021/jp2051905

A. E. Nikolaev performed the fluorescence experimental measurements and analyzed spectra;
R.G. Bird performed the microwave experimental measurements and analyzed spectra;
A. E. Nikolaev and R.G. Bird wrote the paper

6.1 ABSTRACT

Rotationally resolved electronic spectra of several low frequency vibrational bands that appear in the $S_1 \leftarrow S_0$ transition of 4-fluorobenzyl alcohol (4FBA) in the collision-free environment of a molecular beam have been observed and assigned. Each transition is split into two or more components by the tunneling motion of the attached $-CH_2OH$ group. A similar splitting is observed in the microwave spectrum of 4FBA. Analyses of these data show that 4FBA has a *gauche* structure in both electronic states, but that the ground state C_1C_2-C_7O dihedral angle of ~60° changes by ~30° when the photon is absorbed. The barriers to the torsional motion of the attached $-CH_2OH$ group are also quite different in the two electronic states; V_2 ~300 cm^{-1} high and ~60° wide in the S_0 state, and V_2 ~300 cm^{-1} high and ~120 cm^{-1} wide (or V_2 ~1200 cm^{-1} high and ~60° wide) in the S_1 state. Possible reasons for these behaviors are discussed.

6.2 INTRODUCTION

The structures and dynamical properties of flexible alkylbenzenes and their biologically relevant derivatives have been of interest for a long time.[1] Flexibility is caused by the large number of degrees of freedom of the alkyl chains in these molecules, many of which have relatively low frequencies. This can lead to a number of energetically accessible conformers that may be interconverted by torsional and bending modes of substituents attached to the benzene ring. It is of particular interest to identify the naturally occurring conformers and study the pathways that might connect them. Comparisons of the observed structures with predicted ones also may be used to improve on current theoretical methods and provide insight into the fine balance of attractive and repulsive interactions that govern the shapes of large molecules.

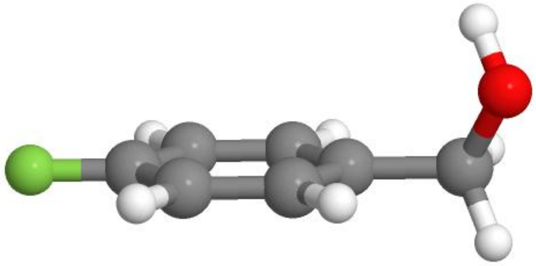

Scheme 6.1. Structural view of 4FBA

4-Fluorobenzyl alcohol (4FBA) is the subject of present report (Scheme 6.1). 4FBA is a structural homolog of benzyl alcohol (BA), the simplest aryl alcohol. Aryl alcohols are widely used solvents in organic synthesis and are frequently found as functional groups in natural products. Their formulae are rather simple; BA is a derivative of methanol (CH_3OH) with one hydrogen of the methyl group replaced by a phenyl ring. Despite this fact, the 3D structures of BA (and 4FBA) have been controversial; the $–CH_2OH$ group could be either planar, staggered, *gauche*, or freely rotating with respect to the ring. Early *ab initio* calculations predicted minimum energy planar or *gauche* structures, while molecular mechanics calculations predict a planar one. An early supersonic jet study suggested a staggered structure.[2] Guchait *et al*.[3] observed two conformers of BA in a later IR/UV study, and suggested that the more populated one was a planar structure. Mons *et al*.,[4] in their IR/UV study, observed only one conformer of BA and assigned it as a *gauche* conformer, slightly stabilized relative to the other structure by an intramolecular hydrogen bond involving the –OH hydrogen atom and the π electrons of the ring. More recently, microwave experiments by Bohn and co-workers[5] have established that BA has a *gauche* structure with a C_1C_2-C_7O dihedral angle of approximately 60°.

As will be seen, BA and its derivatives exhibit several prominent low-frequency vibrational bands in their low resolution fluorescence excitation spectra. Originally, these were assigned to a –CH_2OH torsional mode; an increased barrier to internal rotation on S_1-S_0 excitation was suggested to be responsible for the significant Franck-Condon activity.[2] But there are many other possible interpretations. Here, we explore the origins of these effects in the 4FBA derivative using high resolution microwave and electronic spectroscopy techniques in the gas phase.

6.3 EXPERIMENTAL

4FBA was obtained from Aldrich (98%) and used without further purification. Deuterium substitution of the OH group was performed by mixing the sample with D_2O, followed by phase separation. The yield was monitored using NMR and GCMS.

Microwave experiments were performed using the chirped-pulse Fourier transform microwave (CP-FTMW) technique. Our spectrometer resembles the broadband instrument developed by the Pate group,[6] but it employs a mirror-horn cavity[7] to reduce the power requirements while retaining some of the broadband capabilities of the original machine. Typically, 500 MHz chirps of the spectrum were recorded and Fourier-transformed one at a time, and then joined together to obtain the overall spectrum. 4FBA was heated to 90°C and expanded through a pulsed nozzle at 10 Hz with ~ 1.5 kTorr He backing gas. The nozzle was placed perpendicular to the microwave signal axis.

Vibrationally resolved fluorescence excitation spectra (FES) were obtained using a Quanta Ray PDL-1 dye laser (Coumarin 540) pumped by the second harmonic of Nd^{3+}/YAG DCR-1A laser, operating at 10 Hz. The visible output of the PDL-1 was doubled with a BBO crystal and tracked with a homemade autotracker. Liquid 4FBA was heated to 60 ^{o}C and expanded through a 0.75 mm orifice pulsed nozzle (General Valve Series 9), with 8 kTorr backing pressure of helium into the vacuum chamber. The observed fluorescence was detected at the crossing point of the supersonic jet and laser beam using a phototube and properly delayed boxcar integrator.

Rotationally resolved FES were obtained using a modified Spectra-Physics 380D ring dye laser, operating with Pyrromethane 556 dye and intracavity doubled in BBO, yielding 800 μW of UV radiation. The sample was placed in a heated quartz source at 80^{o}C and expanded with 750 Torr He through a heated 240 μm nozzle into a differentially pumped molecular beam machine. The sample was skimmed once 3 cm downstream of the nozzle. Fluorescence was collected using spatially selective optics placed 12 cm downstream of the nozzle. At this location, the Doppler-limited spectral resolution is about 18 MHz. The FES signal was detected by a PMT and photon counting system and processed using data acquisition software.[8] Relative frequency calibration was performed using a near-confocal interferometer having a mode-matched free spectral range of 299.7520 ± 0.0005 MHz. The absolute transition frequencies were determined by comparison to the I_2 absorption spectrum[9] and are accurate to ± 30 MHz.

Theoretical calculations were performed using the Gaussian 03 suite of electronic structure programs.[10]

6.4 RESULTS

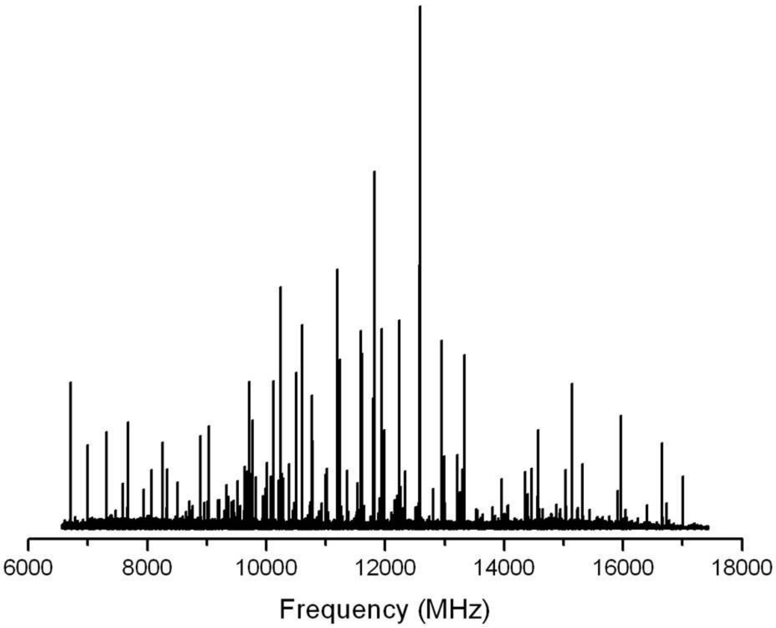

Figure 6.1. Microwave absorption spectrum of 4-fluorobenzyl alcohol (4FBA) from 6.5 to 17.5 GHz, averaging 10000 FIDs.

Figure 6.1 shows the microwave absorption spectrum of 4FBA between 6.5 and 17.5 GHz, recorded using a 10 μs FID and averaging 10,000 FIDs. The spectrum consists of μ_a- and μ_b-type transitions split by rotation-vibration interactions, as shown in detail in Fig. 6.2. The vibrational levels 0^+ and 0^- are the tunneling doublets associated with motion along the –CH_2OH torsional coordinate; μ_a transitions connect rotational levels within each manifold, whereas μ_b transitions connect rotational levels of one manifold with those of the other. Both types of rotational structure were fit using SPCAT[11] to the same Hamiltonian,[5] shown below:

$$\hat{H} = \sum_i \left(\mathcal{H}_i^R + \mathcal{H}_i^{CD}\right) + \mathcal{H}^{\mathrm{INT}}, \text{with } i = +, - \tag{6.1}$$

$$\hat{H}^{INT} = \Delta E + F_{ac}\,(P_aP_c + P_cP_a) + F_{bc}(P_bP_c + P_cP_b) \tag{6.2}$$

Here, $\hat{H}_i^R$ is the rigid rotor Hamiltonian, $\hat{H}_i^{CD}$ is the centrifugal distortion Hamiltonian,[12] and $\hat{H}_i^{\mathrm{INT}}$ is the internal rotation Hamiltonian,[13] all for the state i (0^+ or 0^-). ΔE is the energy difference between the 0^+ and the 0^- levels. F_{ac} and F_{bc} are interaction terms that describe the coupling between the torsional motion of the –CH_2OH group and rotational motion about the *b*- and *a*-inertial axes, respectively. Values of the parameters determined from this fit are listed in Table 6.1. Among these parameters, the inertial defect, $\Delta I = -30.6$ u Å^2, and the energy difference between the 0^+ and the 0^- levels, ΔE = 337 MHz, are the most significant.

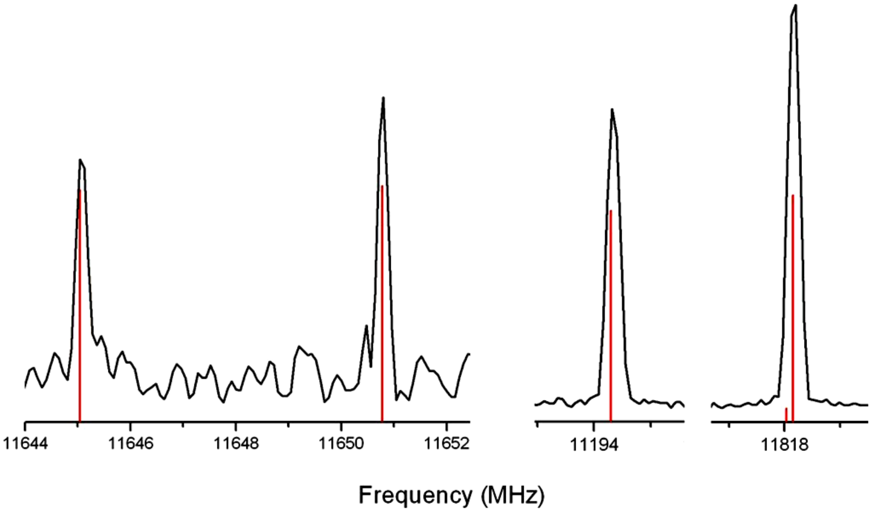

Figure 6.2. Selected portions of the microwave spectrum of 4FBA at higher resolution. From left to right: the *a*-type transitions 7_{17} 0^-←6_{16} 0^- and 7_{17} 0^+←6_{16} 0^+ separated by ~5 MHz; the *b*-type transitions 5_{15} 0^+←4_{04} 0^- and 5_{15} 0^-←4_{04} 0^+ separated by ~600 MHz.

Table 6.1. Inertial constants derived from a fit of 137 lines in the microwave spectrum of 4-fluorobenzyl alcohol (4FBA). The corresponding values for benzyl alcohol are shown for comparison.

Parameter	4FBA[a]	Benzyl Alcohol (Ref. 5)
A 0^+ (MHz)	4624.60(2)	4758.986(1)
B 0^+ (MHz)	925.716(1)	1475.398(1)
C 0^+ (MHz)	809.168(1)	1193.4018(5)
A 0^- (MHz)	4624.77(2)	4759.133(1)
B 0^- (MHz)	925.716(1)	1475.409(1)
C 0^- (MHz)	809.173(1)	1193.3769(5)
D_J (kHz)	-0.0087(5)	0.082(8)
D_{JK} (kHz)	-1.2(3)	2.5(1)
D_K (kHz)	-19(5)	1.7(2)
F_{ab} (MHz)	105.87(4)	222.021(8)
F_{bc} (MHz)	26.333(2)	57.418(1)
ΔE (MHz)	337.10(5)	492.816(2)
V_2 (cm^{-1})	304	280
ΔI u Å^2	-30.6	-25.25

[a] Experimental constants fit using SPCAT (Ref. 11).

Figure 6.3 shows the vibrationally resolved FES of 4FBA recorded in a supersonic jet. Similar spectra have been recorded by others.[2-4] The origin of this spectrum is at 37070.23 cm^{-1}. To the blue of this band, the spectrum exhibits a characteristic low frequency progression with nearly harmonic spacings of ~55 cm^{-1}. This progression has been previously assigned to a –CH_2OH torsional mode by Im, *et al.*[2] In the present experiments, a relatively high backing pressure was needed to eliminate an extensive set of hotbands. The corresponding spectrum of the OD-substituted sample is very similar to that shown in Fig. 6.3; the origin band frequency is the same to within 1 cm^{-1}, and the Franck-Condon progression also is the same, with small blue shifts of 1-5 cm^{-1} of each of the observed bands relative to their positions in the parent molecule. The frequencies of these bands in Fig. 6.3 are listed in Table 6.2.

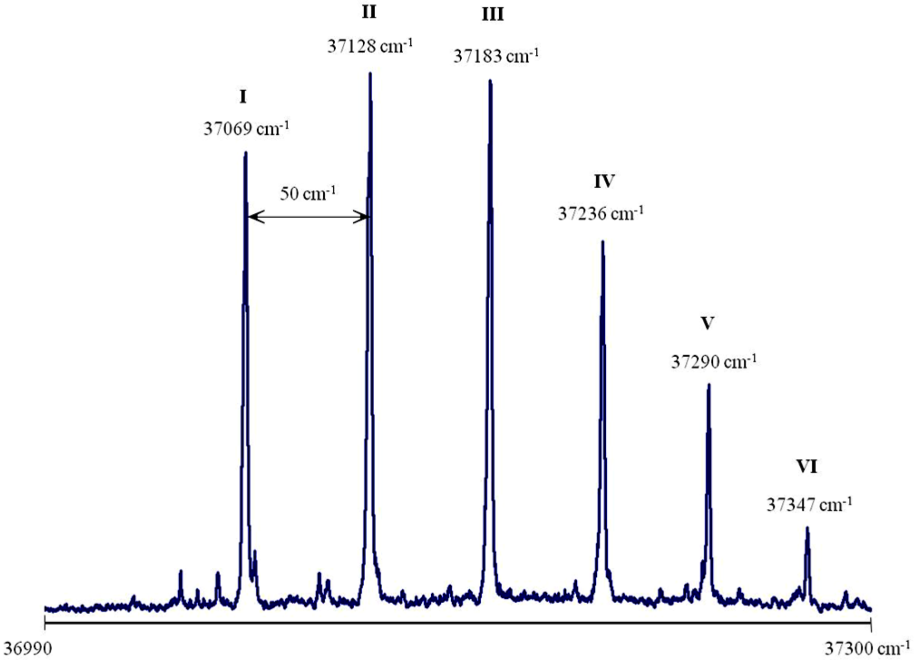

Figure 6.3. Vibrationally resolved fluorescence excitation spectrum of 4FBA.

Table 6.2. Observed vibrational bands in the low resolution $S_1 \leftarrow S_0$ fluorescence excitation spectrum of 4-fluorobenzyl alcohol (4FBA).

Band	Frequency (cm^{-1})^a	Displacement (cm^{-1})	Spacing (cm^{-1})	CIS/6-31g frequency (cm^{-1})	Torsional Assignment	ΔI avg, amu Å^{2a}
I	37069.9	0	0	0	0_0^0	-12.09
II	37127.8	57.9	57.9	73.7	τ_0^1	-13.49
III	37183.1	113.2	55.3	147.4	τ_0^2	-15.58
IV	37235.7	165.8	52.6	221.1	τ_0^3	-17.31
V	37290.0	219.8	54	294.8	τ_0^4	

[a] Average values for all subbands lying within the indicated band (Table 6.3).

Rotationally resolved FES of the first four members of this progression in the S_1-S_0 transition of 4FBA have been obtained. Figure 6.4 shows the first two of these, the rotationally resolved spectra of Bands I and II at ~37070 and ~37128 cm^{-1} (+58 cm^{-1}), respectively. Both spectra contain in excess of 4000 lines and span over 3 cm^{-1} at a rotational temperature of 6 K. Initial attempts to fit these spectra to single bands were unsuccessful. Then, autocorrelation analyses showed that a large number of transitions occur in pairs in each spectrum, with a constant separation of ~320 MHz. Notably, this splitting is comparable to that measured in the microwave spectrum of 4FBA. (We estimate that the UV splittings are known to the order of ±20 MHz.) Thus, to fit Bands I and II, the lower frequency member of every pair in each spectrum was assigned to one subband, originating in the 0^+ level, and the higher frequency member of every pair was assigned to a second subband, originating in the 0^- level. Then, each subband was fit independently using the rigid rotor Hamiltonian in JB95[14] [$\hat{H}_i^R$ in Eq. (6.1)]. The final fit of Band I utilized 112 assigned lines for the first subband and 64 lines for the second subband, with standard deviations of 8.49 and 7.82 MHz, respectively. The final fit of Band II utilized 78 assigned lines for the first subband and 118 lines for the second subband, with standard deviations of 5.87 and 9.0 MHz, respectively. The two subbands in each spectrum each contain approximately 2000 lines, have relative intensities of ~1:1, and are mainly *b*-type bands. (This is consistent with the assignment of the S_1 state of 4FBA as an L_b state, as in the case of other "perpendicularly" substituted benzenes.[15]) Owing to band congestion, the possible contributions of other band types could not be determined. Individual lines identified in the fitting process have FWHM's of about 40 MHz. Examination of the individual Voigt line shapes suggests approximately equal contributions to them from Doppler and lifetime broadening. A 20 MHz Lorentzian contribution to the linewidth suggests a fluorescence lifetime of about 5 ns.

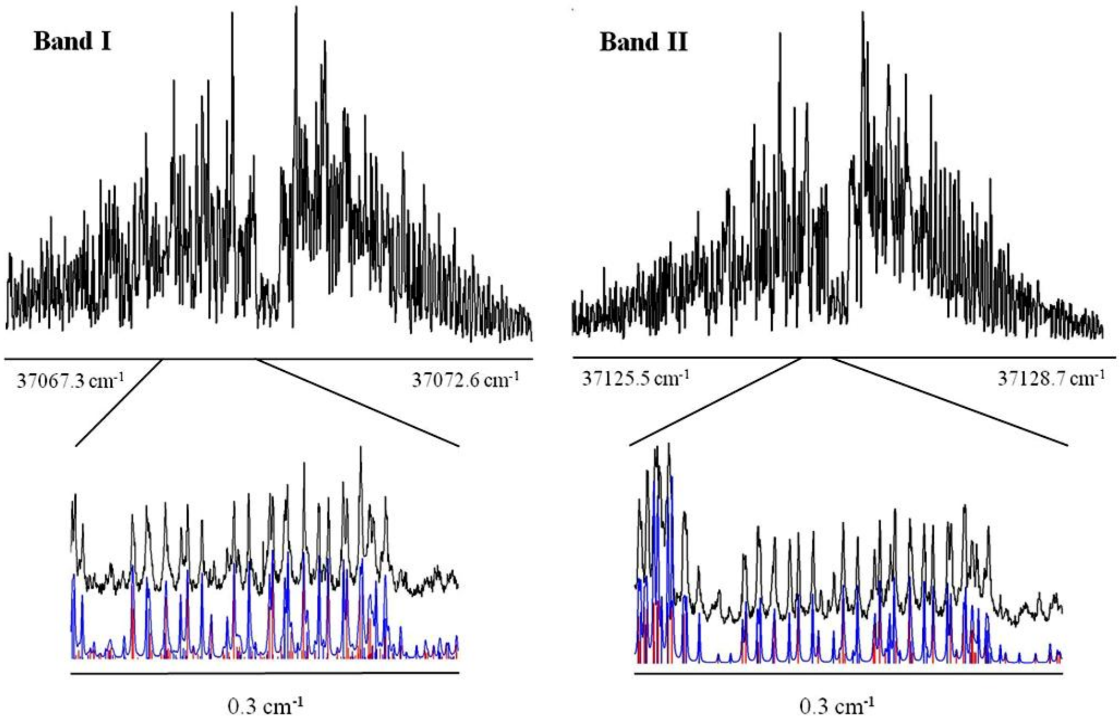

Figure 6.4. High resolution $S_1 \leftarrow S_0$ FES of Band I and Band II of 4FBA in a molecular beam.

Figure 6.5 shows the rotationally resolved spectra of Bands III and IV, observed at ~37183 (+113) and ~37236 cm^{-1} (+166 cm^{-1}), respectively. The appearance of these bands is different from those of Bands I and II; they are significantly more congested. Autocorrelation analyses of Bands III and IV show that each band consists of four subbands. In Band III, these are separated by ~110 and ~320 MHz, and have relative intensities of ~2:1.2:1. The fit of this band utilized ~50 assigned lines for each subband with standard deviations of 9.6, 10.2, 2.7 and 10.7 MHz, respectively. In Band IV, the four subbands are separated by ~320 and ~800 MHz, and have relative intensities of ~1:1:2:2. The fit of this band also utilized ~50 lines for each subband, with standard deviations of 7.9, 7.7, 10.1 and 7.7 MHz, respectively. All subbands in each spectrum are mainly *b*-type bands.

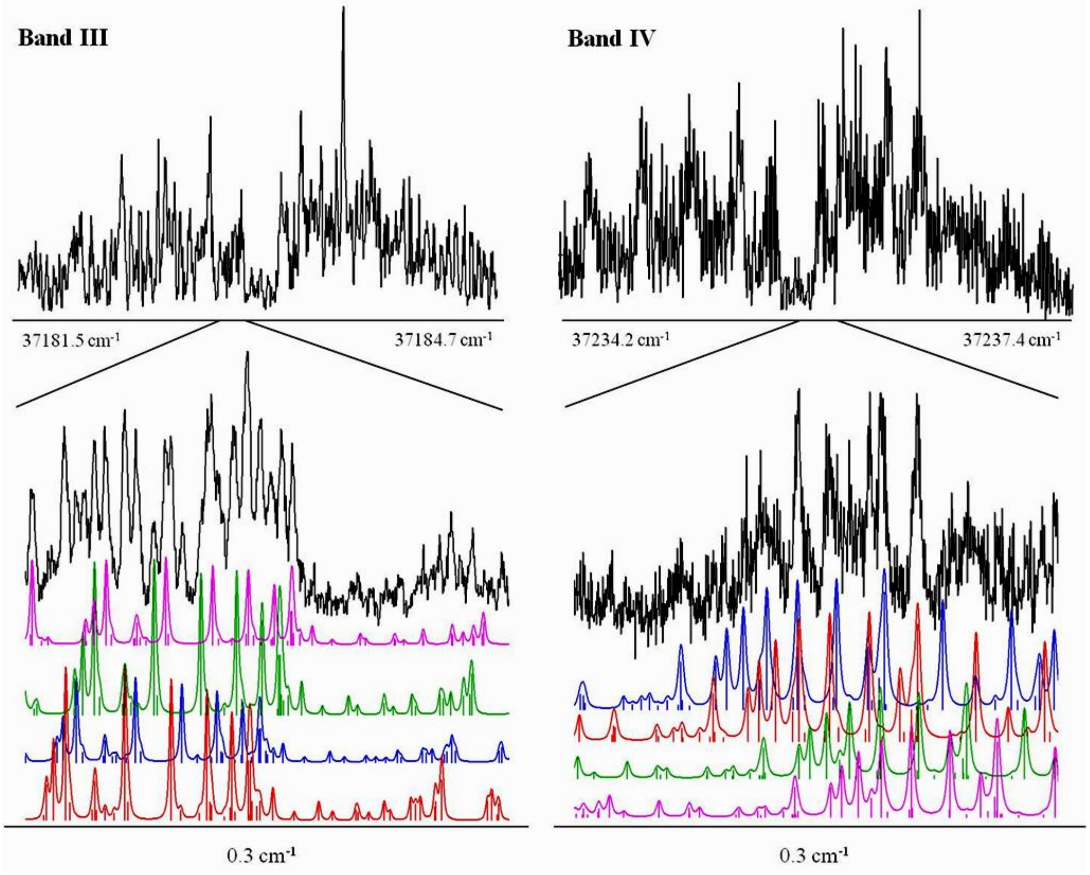

Figure 6.5. High resolution $S_1 \leftarrow S_0$ FES of Band III and IV of 4FBA in a molecular beam.

Ground and excited state inertial parameters of 4FBA that were derived from the fits of the rotationally resolved spectra of Bands I-IV of 4FBA are collected in Tables 6.3 and 6.4. The 12 measured ground state values of A, B, and C are in reasonable agreement with each other, showing that all four bands originate in the same ground state level, presumably the ZPL of the S_0 state. The average value of ΔI, the inertial defect, is -24.5 u Å^2. Comparing these values with those determined in the microwave experiment (Table 6.1), we see that there are differences on the order of 3-6 MHz in the values of the measured rotational constants, a not unreasonable result given the fact that the two sets of data were interpreted using different Hamiltonians. (In most cases, the addition of Watson distortion terms[12] improved the fits of the UV spectra, but these were not included in the final analysis.) The excited state values of A, B, and C are nearly the same for the two (or four) subbands in each spectrum, but differ greatly among the four measured spectra, and from the ground state values. The average values of ΔI are -12.1, -13.5, -15.6, and -17.3 uÅ^2 for Bands I-IV, respectively, evidencing significant structural differences of 4FBA in its ground and excited electronic states.

Table 6.3. Ground state inertial parameters derived from fits of Bands 1-4 in the $S_1 \leftarrow S_0$ electronic spectrum of 4FBA.[a]

	Band	A	B	C	ΔI	Origin Freq.
	Ia	4628.9(20)	928.5(10)	803.1(6)	-24.23	1111328487.7
	Ib	4628.3(15)	928.9(10)	803.8(10)	-24.53	+321.6
	IIa	4628.6(20)	928.8(20)	804.5(15)	-25.10	1113061845.3
I	IIb	4628.7(20)	927.7(15)	804.0(10)	-25.36	+312.8
	IIIa	4627.2(30)	928.0(10)	802.8(10)	-24.26	1114721783.4
	IIIb	4627.0(40)	928.4(10)	803.4(10)	-24.55	+105.6
II	IIIc	4628.6(10)	928.8(5)	803.2(5)	-24.11	+315.9
	IIId	4629.6(25)	929.3(10)	803.8(10)	-24.24	+440.3
	IVa	4628.1 (30)	928.3(10)	803.3(10)	-24.48	1116297330.6
	IVb	4628.4(30)	928.7(10)	803.1(10)	-24.11	+312.2
IV	IVc	4630.1(30)	927.9(10)	802.9(10)	-24.35	+812.3
	IVd	4628.7(30)	927.6(20)	803.2(15)	-24.79	+1119.2

[a] All parameters in MHz, except for ΔI (u Å^2)

Table 6.4. Excited state inertial parameters derived from fits of Bands 1-4 in the $S_1 \leftarrow S_0$ electronic spectrum of 4FBA.[a]

Band		A	B	C	ΔI	τ_1
	Ia	4493.7(10)	925.9(10)	782.2(5)	-12.23	32.8°
	Ib	4493.8(16)	926.4(15)	782.3(5)	-11.95	
	IIa	4473.1(40)	927.2(29)	784.6(35)	-13.96	35.6°
I	IIb	4475.1(30)	926.7(15)	783.2(15)	-13.01	
	IIIa	4454.4(30)	925.6(10)	785.0(10)	-15.67	39.6°
	IIIb	4454.4(30)	926.5(10)	785.5(5)	-15.56	
II	IIIc	4456.6(15)	926.0(5)	785.2(5)	-15.57	
	IIId	4456.6(40)	926.6(15)	785.6(10)	-15.51	
	IVa	4438.3(20)	926.1(10)	787.1(10)	-17.53	43.3°
	IVb	4439.1(20)	926.5(10)	786.8(10)	-17.02	
V	IVc	4439.5(30)	925.4(10)	786.6(10)	-17.51	
	IVd	4440.1(30)	925.4(20)	786.3(20)	-17.17	

[a] All parameters in MHz, except for ΔI (u Å^2) and τ_1 (degrees)

6.5 DISCUSSION

6.5.1 Structure of the ground state.

A number of *ab initio* calculations were performed to interpret the measured inertial parameters of 4FBA. If the –CH_2OH group was co-planar with the aromatic ring, the inertial defect ($\Delta I = I_c - I_a - I_b$) of the molecule would be -3.2 u Å^2, the equivalent of a single methyl group. The experimental structure of the ground state has ΔI = -30.7 u Å^2, so the –CH_2OH group must be significantly out-of-plane. An M05-2X/6-31+G(d,p) calculation converges to the non-planar structure shown in Scheme 6.2; the –CH_2OH group is out-of-the-plane of the benzene ring at an

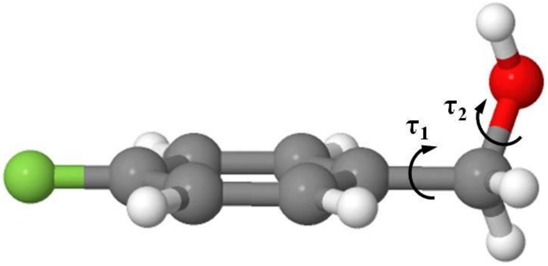

Scheme 6.2. Representations of the C-C-O torsional angle, τ_1, and the C-O-H torsional angle, τ_2, in 4FBA.

angle τ_1 = 44°, and the hydrogen atom of the –OH group points towards the ring at an angle τ_2 = 57°. The optimized structure has ΔI = -20.3 u Å^2. Since the potential energy surface along both torsional coordinates is likely to be fairly flat, one anticipates that the calculated and experimental values of ΔI might not agree owing to the effects of vibrational averaging. "Best-fit" values of τ_1 and τ_2 may be obtained by simultaneously changing them until the calculated values of A, B, C, and ΔI match those of the experimental structure. This yields the values τ_1 = 55° and τ_2 = -15°, which has ΔI = -24.4 u Å^2, close to the experimental value.

The value of ΔI is fairly insensitive to τ_2 owing to hydrogen's small mass. Therefore, we performed an extensive series of calculations with higher basis sets to search for the most likely position of the attached –OH group. 6-31G$^+$ calculations of the conformational landscapes show two local minima. The lower energy one has the hydrogen atom pointing towards the ring, with τ_2 (C_1C_7-OH) = 69°; the higher energy one has the hydrogen atom pointing away from the ring, with τ_2 (C_1C_7-OH) = 180°. Calculations suggest an energy difference of about 1000 cm^{-1} between the two structures. Nascent π-hydrogen bonding between the –OH hydrogen atom and the π-cloud of the aromatic ring is a likely source of this energy difference.[16]

6.5.2 Structure of the excited state.

While the inertial parameters of the excited state vibrational levels of 4FBA are different for each band, in general all values of A are about 0.1% larger in the S_1 state, compared to the ground state. Values of B are about 0.2% larger and values of C are about 10% smaller in the S_1 state. The small increases in A and B indicate that the benzene ring takes on quinoidal shape in the S_1 state, as in the case of aniline[17] and other substituted benzenes.[18] More insight into the light-induced changes in mass distribution along the *a*-, *b*- and *c*-axes is provided by comparisons of the planar moments of inertia listed in Table 6.5. The P_{aa} values of the excited state are approximately 5 u Å^2 larger than those of the ground state, and the P_{bb} values of the excited state are about 8 u Å^2 larger than those of the ground state. Both changes are consistent with a quinoidal structure for the S_1 state; the ring is expanded in both in-plane directions. More striking are the differences in C, and in the ΔI values of the two states; the values of the inertial defects in the S_1 state are all smaller in magnitude than the S_0 state, varying from -12.1 to -17.3 u Å^2 in Bands I through IV. Changes in the ring bond lengths and/or angles cannot be responsible for this trend. Instead, the data show that the dihedral angle τ_1 decreases substantially in electronic excitation, bringing the –CH_2OH group closer to the plane of the aromatic ring.

Table 6.5. The second moments of inertia in both S_0 ground and S_1 excited states

Band		P_{aa} (u Å^2)[a]	P_{bb} (u Å^2)	P_{cc} (u Å^2)
S_0		530.6	94.0	15.3
S_1	I	539.8	106.4	6.1
	II	538.1	106.0	7.0
	III	538.2	105.6	7.8
	IV	537.0	105.1	8.7

[a] Paa = $(I_b + I_c - I_a)/2$

The CIS/6-31g$^+$ calculated minimum energy structure of S_1 4FBA has a –CH_2OH out-of-plane angle of τ_1 = 32.8° (Table 4). The calculated inertial defect of this structure is -13 u Å^2, close to the experimental value from Band I of -12.1 u Å^2. Then, by varying τ_1 with all other parameters fixed, the observed inertial defects for the remaining Bands II-IV can be reproduced with τ_1 values of 35.6° (ΔI = -14 u Å^2), 39.6° (ΔI = -15 u Å^2), and 43.3 (ΔI = -17 u Å^2), as shown in Figure 6.6. Clearly, excitation of the S_1 state of FBA has a major influence on the preferred orientation of the –CH_2OH group.

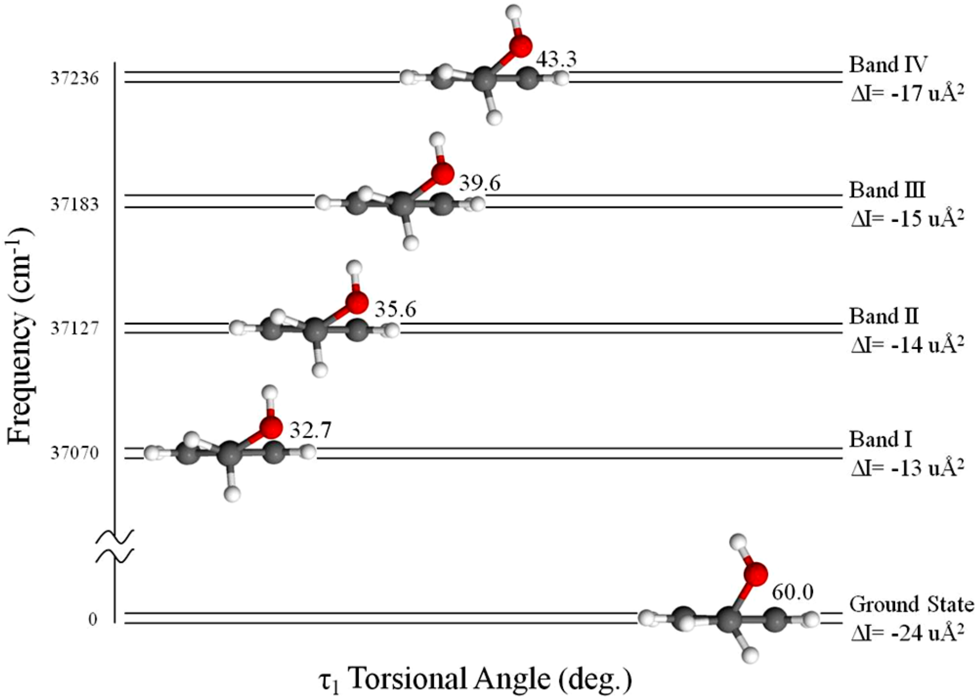

Figure 6.6. Electronic and vibrational state dependence of the measured inertial defect of 4FBA in the gas phase

6.5.3 Tunneling

Further information about the motion of the attached –CH_2OH group in the ground and electronically excited states of 4FBA is provided by the observation of tunneling splittings in its CP-FTMW and FES spectra. There are four equivalent structures in the ground state of 4FBA, two of which are separated by a 60° rotation of the –CH_2OH group, and two of which are separated by a 120° rotation of the –CH_2OH group, as shown in Figure 6.7 (left). This leads to two different barrier widths and two different barrier heights along the torsional coordinate. In the 60° motion, the –OH hydrogen remains in contact with the π-orbitals either above or below the plane of the ring; for the rotor to tunnel through the 120° barrier, it must break this hydrogen bond. Therefore, the 60° motion is expected to have a smaller barrier height as well as a smaller barrier width. Additionally, tunneling through the 60° barrier inverts the μ_b-type dipole while tunneling through the 120° barrier inverts the μ_c-type dipole. Since only μ_a and μ_b-type transitions were observed in the CP-FTMW spectrum, the observed tunneling splitting of 337 MHz must be due to the tunneling through the 60° barrier. The effective barrier height of this two-fold motion is 304 cm^{-1}.

The parent molecule benzyl alcohol (BA) exhibits a similar behavior. Recent microwave experiments[5] show that ground state BA has a *gauche* structure characterized by a C_1C_2-C_7O dihedral angle of approximately 60°. A tunneling splitting of ~493 MHz (~136 MHz) was observed in the microwave spectrum of BA that was attributed to –CH_2OH (–CH_2OD) internal rotation analogous to that observed in 4FBA. A one-dimensional model calculation shows that these splittings can be accounted for if the –CH_2OH internal rotation is opposed by a two-fold barrier of order ~280 cm^{-1}.[5] The 3-fluoro derivative of BA also exhibits a tunneling splitting in its microwave spectrum; in this case, the motion connects two equivalent minima above and below the plane of the aromatic ring, and is described by a two-fold barrier of height 155 cm^{-1}.[19] The larger barrier in ground state 4FBA compared to both BA and 3FBA might have its origin in the electron withdrawing ability of the attached fluorine atom.

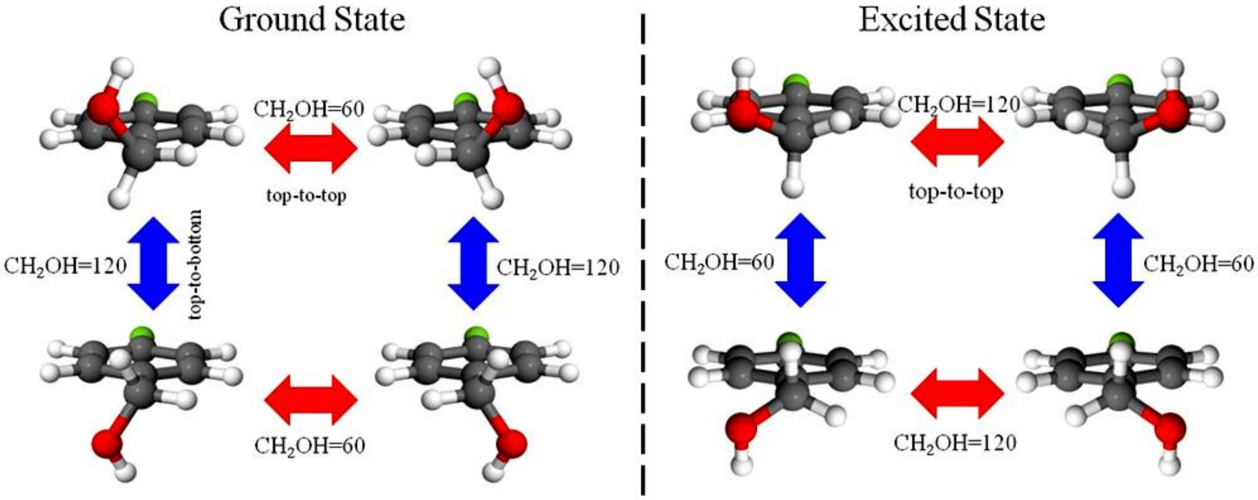

Figure 6.7. Torsional dynamics of the –CH$_2$OH group in the ground electronic state (left) and the first excited state (right) of 4FBA.

Tunneling splittings also are observed in the FES spectrum of 4FBA, but in this case their interpretation is more subtle. Again, we expect four equivalent structures along the –CH$_2$OH torsional coordinate in the S$_1$ state. But the zero-point vibrational level of excited state 4FBA has a significantly smaller (in magnitude) inertial defect (-12.1 u Å^2) than that of the ground state (-30.7 u Å^2). This change in the inertial defect reflects a change in the preferred out-of-plane angle of the —CH$_2$OH group from ~60° to ~30°, which is equivalent to switching from an eclipsed to a staggered position (Scheme 6.3). This change also increases the angular separation

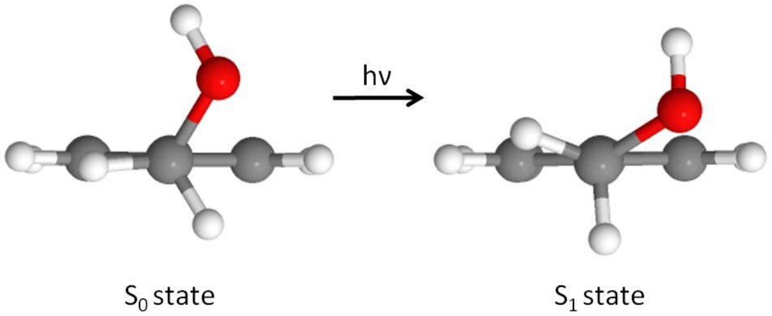

Scheme 6.3. –CH_2OH rotor positions in the ground (eclipsed) and excited (staggered) electronic states of 4FBA.

between the equivalent –CH_2OH positions that are exchanged by the "top-to-top" tunneling motion, from ~60° to ~120°, and decreases the angular separation between the equivalent –CH_2OH positions that are exchanged by the "top-to-bottom" tunneling motion, from ~ 120° to ~60° (Figure 6.7, right). Thus, owing the "phase shift" of the S_1 surface with respect to the S_0 surface along the tunneling coordinate, all four torsional sublevels in the excited state are in principle accessible *via* Franck-Condon allowed transitions from the four torsional sublevels in the ground state. The usual symmetry-based selection rules do not apply.

The vibrational progression of 0, 58, 113, and 166 cm^{-1} that is observed in the low resolution FES spectrum of 4FBA may be assigned to transitions from the v=0 torsional manifold of the ground state to the v=0, 1, 2, and 3 torsional manifolds of the excited state. The vibrational spacings in this progression may be fit to a barrier that is 113° wide and 300 cm^{-1} high using a Gaussian model. This increased barrier width, compared to that of the ground state, is consistent with expectations, as it reflects the increase in the angular separation of equivalent –CH_2OH positions that are exchanged by the "top-to-top" tunneling motion, see Figure 6.8. The tunneling splitting of ~320 MHz that appears in Bands I and II of this progression may be assigned to the ground state, where the barrier width is ~60°, as already mentioned. No other splittings appear in these bands at our resolution. However, new splittings do appear in Bands III and IV; significantly, the new splitting (~110 MHz) in Band III is less than ~320 MHz, whereas the new splitting in Band IV (~800 MHz) is greater than ~320 MHz. One interpretation of these new splittings is that they are the result of ~120° "top-to-top" motion in the S_1 state. With the same Gaussian model, these splittings were fit to a barrier of ~300 cm^{-1}. Even though the barrier height is small, the large angular width causes the effective barrier height to be much larger. This large effective barrier height explains the absence of excited state splittings in Bands I and II.

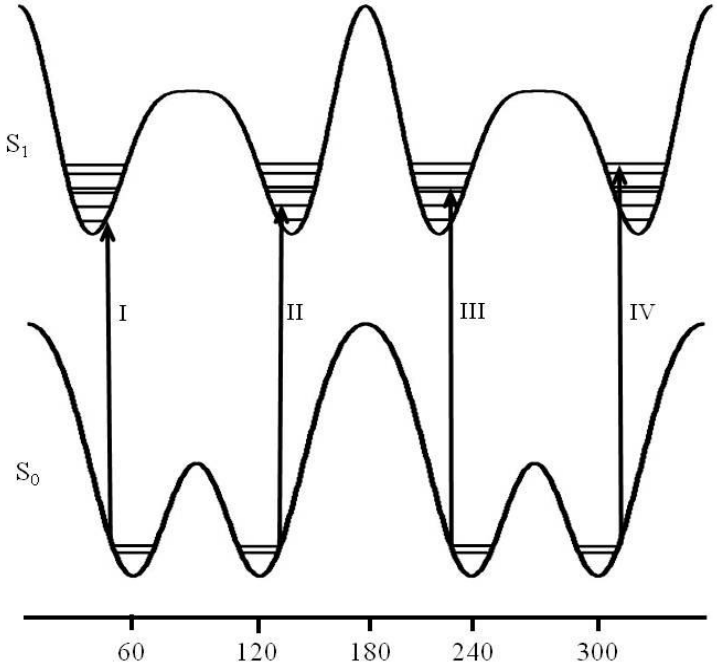

Figure 6.8. Energy landscape along the –CH_2OH torsional coordinate and assignment of the four bands in the $S_1 \leftarrow S_0$ FES spectra of 4FBA

Another interpretation of the new splittings that appear in Bands III-IV is that they arise from "top-to-bottom" type torsional motions, made accessible by the aforementioned shift of two surfaces with respect to each other, see Figures 6.7 and 6.8. Motions of this type should be governed by higher barriers than "top-to-top" motions, since they require a breaking of the π-hydrogen bond involving the –CH_2OH group and the ring π-electrons. Consistent with this view is the absence of tunneling splittings that would be produced by this motion in Bands I and II; they are apparently too small to resolve in the high resolution UV spectra. Also consistent are the observed relative intensities of the four observed subbands in Bands III and IV; ~2:1:2:1 in Band III and ~1:1:2:2 in Band IV. The observed tunneling splittings of ~110 and ~800 MHz in these two bands give an effective barrier height for the ~60° motion in the zero-point level of excited state 4FBA of ~1200 cm^{-1}. The increased height of this barrier, compared to the ground state, also accords with expectations; this is a reasonable estimate of the strength of a hydrogen bond.[16]

Of the two explanations offered for these splittings, the "top-to-top" motion is preferred, since the inertial defect data show that excitation of the -CH_2OH torsional mode makes for effectively *less* planar structures in the electronically excited state.

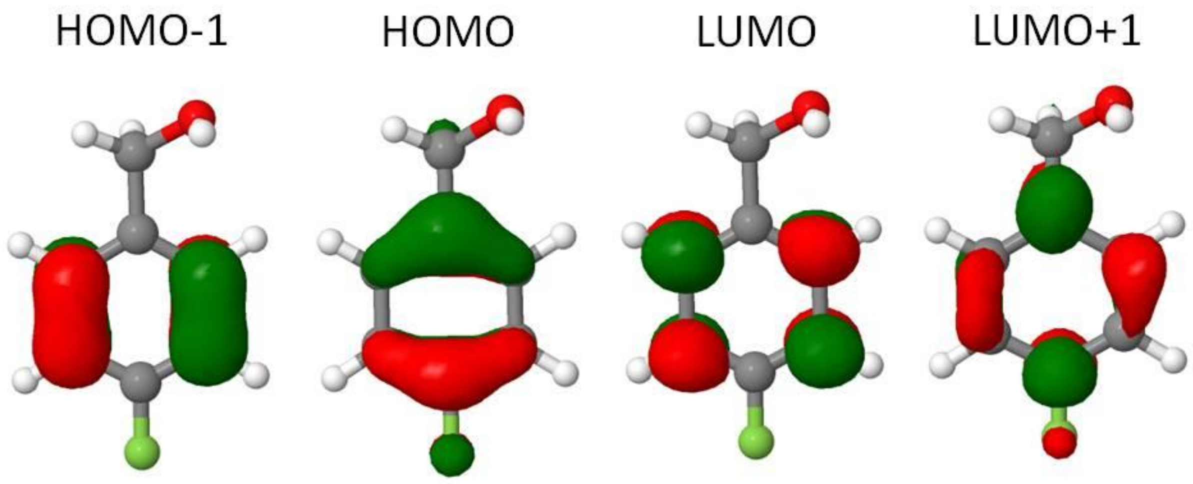

Figure 6.9. (left to right) The CIS/6-311g(d,p) calculated HOMO-1, HOMO, LUMO, and LUMO+1 molecular orbitals of 4FBA.

The change in the preferred –CH_2OH rotor position from eclipsed to staggered upon electronic excitation is a consequence of a light-induced change in the π–electron distribution in the aromatic ring. Figure 6.9 shows the CIS/6-311g(d,p) calculated molecular orbitals for the ground and excited states of 4FBA. S_1 excitation of 4FBA can be described by two single electron transitions; the major one is HOMO to LUMO (75%) with a small amount of HOMO-1 to LUMO+1 (25%). From these transitions, an electronic density difference can be calculated, as shown in Figure 6.10. (Here, red indicates an increase π-electron density, while blue indicates a decrease in π-electron density). Careful examination of these results shows that the π-electron density shifts from the C_α carbons to the C_β position when the photon is absorbed, which causes the rotor to shift from an eclipsed to a staggered position. In the ground state, the large electronic density around C_α interacts with the –OH hydrogen, driving the rotor into an eclipsed position. In the excited state, the majority of the electronic density shifts to C_β, causing the rotor to switch to a staggered position. This electronic density change is also reflected in the calculated –OH hydrogen-C_β distance, as this decreases from 3.1 Å (S_0) to 2.9 Å (S_1), reflecting an increase in interaction between the two groups. Therefore, the strength of the π-hydrogen bond in 4FBA is higher in the S_1 state, compared to the S_0 state in the isolated molecule. Ionization-induced changes in the preferred conformations of other molecules containing –CH_2OH groups have been previously observed.[20]

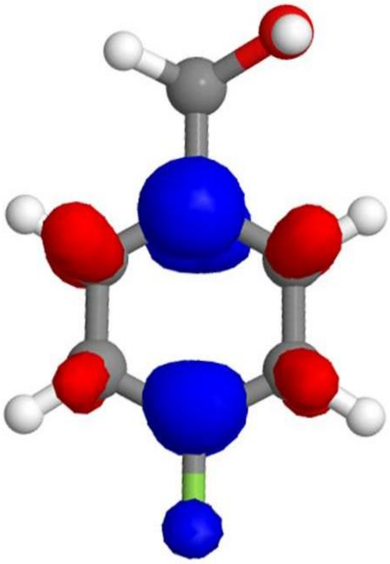

Figure 6.10. The CIS/6-311g(d,p) calculated "HOMO-LUMO" π-electron density difference between the ground and excited state of FBA. Red represents an increase in electronic density, while blue represents a decrease.

6.6 SUMMARY

4-Fluorobenzyl alcohol in the gas phase exhibits rich microwave and UV spectra. Analysis of the microwave spectrum shows that the attached $–CH_2OH$ rotor is in an eclipsed position and tunnels between two equivalent positions on the top and bottom of the benzene ring. Analysis of the UV spectrum shows that the $–CH_2OH$ rotor is in a staggered position in the excited S_1 state and tunnels between two equivalent positions on the top and bottom of the benzene ring. The shift in equilibrium positions of the $–CH_2OH$ group is the result of the change in the electron density caused by a quinoidal-like structure in the excited state. This shift allows the spectroscopic sampling of regions of the excited state potential energy surfaces that would otherwise be forbidden by selection rules. Barriers to the torsional motions of the $–CH_2OH$

group in the two states were determined by an analysis of the tunneling splittings observed in the microwave and fluorescence excitation spectra.

6.7 ACKNOWLEDGEMENTS

This work has been supported by NSF (CHE-0315584, CHE-0618740, CHE-0911117, and CHE-0960074) to whom we are grateful.

6.8 REFERENCES

(1) A review of the early literature in this field is given in Borst, *et al*., *J. Chem. Phys*. **116**, 7057 (2002)

(2) H. –S. Im, E. R. Bernstein, H. V. Secor, and J. I. Seeman, *J. Am. Chem. Soc*. **113**, 4422 (1991).

(3) N. Guchhait, T. Ebata, and N. Mikami, J. *Am. Chem. Soc*. **121**, 5705 (1999).

(4) M. Mons, E. G. Robertson, and J. P. Simons, *J. Phys. Chem*. **A 104**, 1430 (2000).

(5) K. Utzat, R. K. Bohn, J. A. Montgomery, Jr., H. H. Michaels, and W. Caminati, *J. Phys. Chem. A* **114**, 6913 (2010).

(6) G. G. Brown, B. C. Dian, K. O. Douglass, S. M. Geyer, S. T. Shipman, and B. H. Pate, *Rev. Sci. Instrum*. **79**, 053103 (2008).

(7) R. G. Bird, J. L. Neill, V. J. Alstadt, J. W. Young, B. H. Pate, and D. W. Pratt, *J. Phys. Chem. A,* in press.

(8) D. F. Plusquellic, Ph. D. Thesis, University of Pittsburgh, 1992.

(9) S. Gerstenkorn and P. Luc, *Atlas du spectroscopie d'absorption de la molecule d'iode*, CNRS, Paris, 1978 and 1982.

(10) M. J. Frisch, G. W. Trucks, H. B. Schlegel et al., Gaussian 03, Gaussian, Inc., Wallingford, CT, 2004.

(11) H. M. Pickett, *J. Mol. Spectrosc.* **148,** 371 (1991).

(12) J. K. G. Watson, in *Vibrational Spectra and Structure*, ed. J. R. Durig (Elsevier, Amsterdam, 1977), Vol. 6, p. 1.

(13) W. Gordy and R. L. Cook, *Microwave Molecular Spectra*, 3rd ed., Wiley-Interscience, New York, 1984.

(14) D. F. Plusquellic, R. D. Suenram, B. Mate', J. O. Jensen, and A. C. Samuels, J. *Chem. Phys*. **115**, 3057 (2001).

(15) J. W. Ribblett, D. R. Borst, and D. W. Pratt, *J. Chem. Phys.* **111**, 8454 (1999).

(16) D. M. Miller, J. W. Young, P. J. Morgan, and D. W. Pratt, *J. Chem. Phys*. **133**, 124312 (2010).

(17) W.E. Sinclair and D.W. Pratt, *J. Chem. Phys*. **105**, 7942 (1996).

(18) T. Cvitas, J. M. Hollas, and G. H. Kirby, *Mol. Phys*. **19**, 305 (1970).

(19) S.-Y. Tang, Z.-N. Xie, A. Maris, and W. Caminati, *Chem. Phys. Lett*. **498**, 52 (2010).

(20) C.E.H. Dessent, W.D. Geppert, S. Ullrich, and K. Müller-Dethlefs, *Chem. Phys. Lett*. **319,** 375 (2000).

7.0 CHIRPED-PULSED FTMW SPECTRA OF VALERIC ACID, 5-AMINOVALERIC ACID, AND δ-VALEROLACTAM. A STUDY OF AMINO ACID MIMICS IN THE GAS PHASE

To be submitted for publication

R.G. Bird and D.P. Zaleski performed the experimental measurements and analyzed the spectra, V. Vaquero performed the theoretical calculations, and R.G. Bird wrote the paper.

7.1 ABSTRACT

The lowest energy conformations of valeric acid, 5-aminovaleric acid (AVA), and δ-valerolactam were determined using chirped-pulsed Fourier transform microwave spectroscopy. Upon heating, AVA reacted to form δ-valerolactam. Microwave spectra of valeric acid and δ-valerolactam were recorded and their structures were determined. A study of the reaction pathway leading to δ-valerolactam identified the preferred structure of AVA and demonstrated that an n→π* interaction plays the key role in the transformation of reactant into product. Additionally, the spectra of single and double water complexes of δ-valerolactam along with the ^{13}C and ^{15}N-substituted species (in natural abundance) were collected and analyzed.

7.2 INTRODUCTION

Progressive substitution of an organic molecule with functional groups creates new opportunities for intramolecular interactions between them. For example, the Pace group[1] showed that protein stability was enhanced by replacing different residues with proline, an amino acid known for promoting n→π* interactions. A simple way of determining the relative strengths of such interactions is to compare the melting points of the different substances. For example, since the melting point of 5-aminovaleric acid (AVA) is 195 °C higher than that of valeric acid,[2] one can imagine that there are additional attractive interactions in the crystalline solid that stabilize the δ-amino acid relative to the unsubstituted acid. Intrigued by this fact, we report here a study of these two molecules by chirped-pulse Fourier-transform microwave (CP-FTMW) spectroscopy which was intended to determine the structures of their preferred conformations and to identify the important intra and intermolecular interactions that might distinguish them. Comparison of these results with previous results on propanoic acid,[3] 3-aminopropanoic acid[4,5] (β-alanine), and 4-aminobutyric acid[6] (GABA) will additionally reveal how these interactions are affected by differences in the lengths of the backbones to which the functional groups are attached.

As will become apparent, our CP-FTMW study of AVA revealed that it could be transformed into δ-valerolactam by heating in the pulsed nozzle, and that an n→π* interaction between the $–NH_2$ and –COOH groups plays a key role in this process. Interactions of this type were first identified in 1973, when Bürgi and Dunitz[7] observed short interaction distances between nucleophiles and carbonyl groups while inspecting high resolution crystal structures of small molecules. These Bürgi-Dunitz interactions are created by a polarizing carbonyl group which exposes the electrophilic carbon to a nucleophilic attack. Thus, the n-orbital (yellow) of the nucleophilic atom interacts with the π* orbital (green) of the carbonyl carbon (Scheme 7.1).

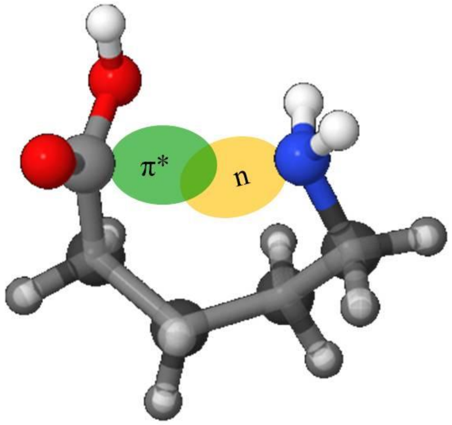

Scheme 7.1. The Bürgi-Dunitz n- π* interactions.

While steric repulsion had been previously thought to be a major factor in peptide conformational stability, Hinderaker *et al.*[8] proved that n→π* interactions have a greater effect. Such interactions were also shown to stabilize both α-helices and PPII helices[9] and to control the reaction responsible for prebiotic syntheses of activated ribonucleotides.[10] Additionally, Raines and co-workers[11] showed that increasing the strength of n→π* interactions increases the stability of collagen. Furthermore, Fufezan[12] speculated that these interactions are responsible for the formation of α-helices in short peptides when current theories about stability contradict these results. Additionally, a large study of the protein database by Bartlett, *et al*.[13] discovered possible n→π* interactions in all 1,731 proteins that they surveyed. In what follows, we show that an interaction of this type also is responsible for the formation of lactams from δ-amino acids, thereby transforming them into biologically "irrelevant" species.

7.3 EXPERIMENTAL

Valeric acid and 5-aminovaleric acid were purchased from Aldrich and used without further purification. Our CP-FTMW spectrometer resembles the broadband instrument developed by the Pate group[14], but it employs a mirror-horn cavity[15] to reduce the power requirements while retaining some of the broadband capabilities of the original machine. Liquid valeric acid (VA) was placed in an external sample container and 1 bar of He was flowed over it. The gas mixture then passed through a nozzle heated to 55 °C, to prevent dimer formation, and expanded perpendicular to the microwave axis. The spectra of VA were taken between 6.5 and 17.5 GHz in 450 MHz segments, collecting a 10 μs FID and signal averaging for up to 5,000 shots.

In the AVA experiment, the sample was heated to 80 °C, backed by 1 bar Ne, and expanded through 3 nozzles. Upon heating AVA, it was discovered that the amino and carboxylic groups had reacted with each other, producing the condensation product δ-valerolactam (DVL). Subsequently, a CP-FTMW spectrum of DVL was recorded using the Pate group[13] broadband instrument from 6.5 to 18.5 GHz. ^{13}C and ^{15}N-substituted species (in natural abundance) were detected collecting 150,000 averages. Theoretical calculations were performed using the Gaussian 03 suite of electronic structure programs.[16]

7.4 RESULTS

7.4.1 Valeric Acid

Figure 7.1 shows the microwave spectrum of valeric acid (VA) between 6-18 GHz. Eleven μ_a-type R-branch transitions were detected and analyzed using JB95.[17] The parameters obtained from this fit are listed in Table 7.1 and show excellent agreement with theoretical values.

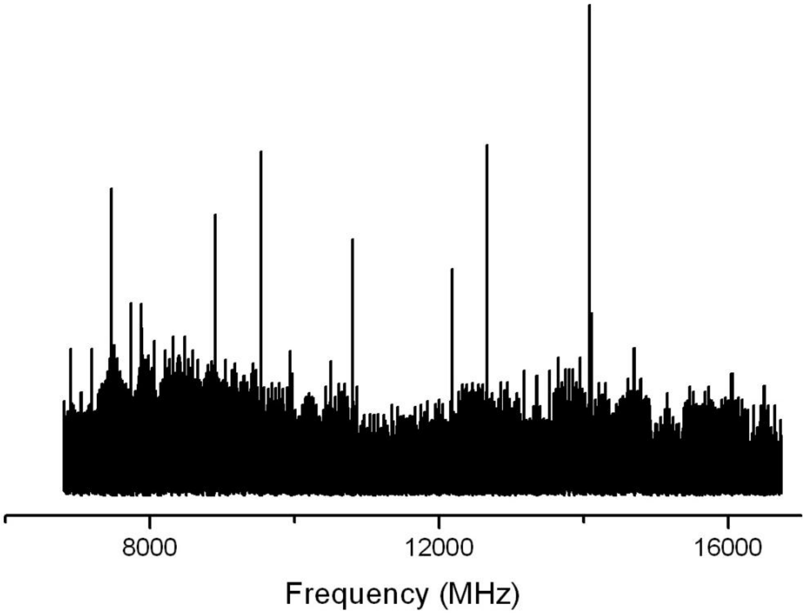

Figure 7.1. The CP-FTMW spectrum of VA from 6 to 18 GHz, collected by averaging 5,000 chirped pulses spanning 450 MHz, Fourier transforming each segment, and joining them together.

Table 7.1 Rotational constants of valeric acid.

Parameters	Experiment	Theory[a]
A (MHz)	7951.42(1)	8001.27
B (MHz)	1051.011(5)	1058.629
C (MHz)	950.947(3)	956.863
ΔI (u Å^2)	-13.0	-12.4

[a] Calculated using Gaussian 03 (M052x/6-31+g(d)).

7.4.2 5-Aminovaleric Acid

Figure 2 shows the microwave spectrum that was observed when AVA was heated in a metal nozzle and expanded into the vacuum chamber in a He carrier gas. Despite several efforts, none of the strong transitions that were detected could be fit using the rotational constants calculated by Gaussian for any of the expected low energy conformations of AVA. But a unique fit of the observed spectrum was obtained using the predicted rotational constants of the condensation product δ-valerolactam (DVL, Scheme 7.2). The parameters (including N-14 coupling constants) constants) obtained from this fit are listed in Table 7.2 and show excellent agreement with both theory and the rotational constants previously measured by Kuze, *et al*.[18]

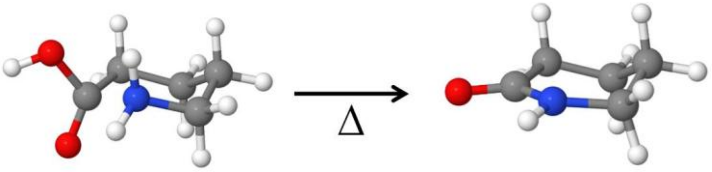

Scheme 7.2. Transformation of 5-aminovaleric acid to δ-valerolactam upon heating.

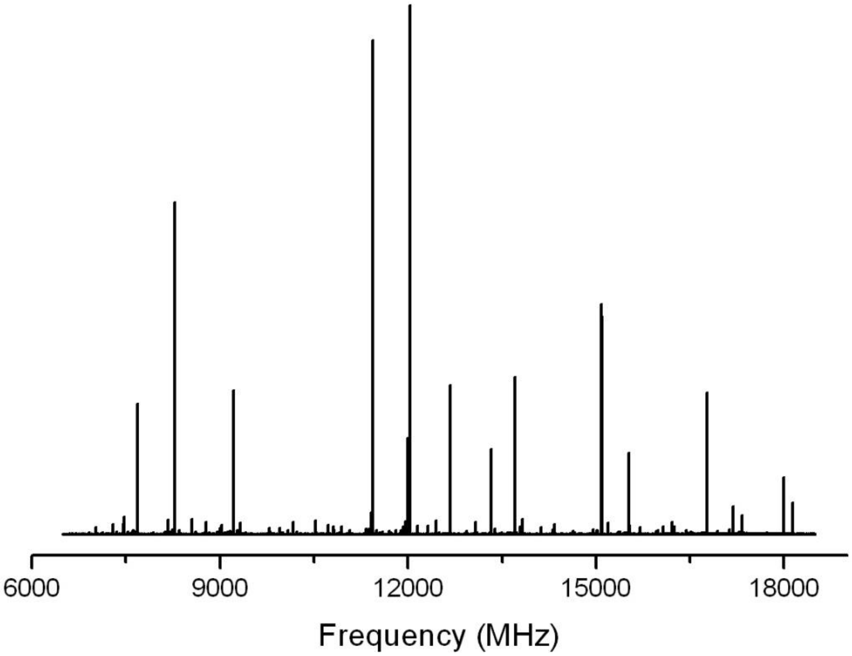

Figure 7.2. Microwave spectrum of δ-valerolactam from 6.5-18.5 GHz collecting 150,000 averages.

Table 7.2. Rotational and N-14 quadrupole coupling constants of δ-valerolactam.

Parameter	This Work	Kuze (Ref 17)	Theory
A (MHz)	4590.9107(6)	4590.96(11)	4618.95[a]
B (MHz)	2495.0392(6)	2495.03(2)	2505.722[a]
C (MHz)	1731.0550(3)	1731.06(2)	1739.754[a]
χ_{aa} (MHz)	2.323(8)		2.32[b]
χ_{bb} (MHz)	1.86(1)		1.84[b]
χ_{cc} (MHz)	-4.18(1)		-4.16[b]
ΔI (u Å^2)	-20.7	-21.0	-20.6

[a] Calculated using Gaussian 03 (M052x/6-31+g(d)).
[b] Calculated from the optimized structure using Gaussian 03 (b3pw91/6-311+g(df,pd)).

Subsequent experiments on DVL were performed on the broadband spectrometer at UVa. Deep signal averaging on this instrument made possible the detection of singly substituted ^{13}C and ^{15}N species in natural abundance (Table 7.4). A comparison of these values using Kraitchman's equations[19] led to the determination of the heavy-atom substitution coordinates of DVL; see Figure 7.10 and Table 7.5 (Supplementary Information). The resulting substitution structure is shown in Figure 7.3.

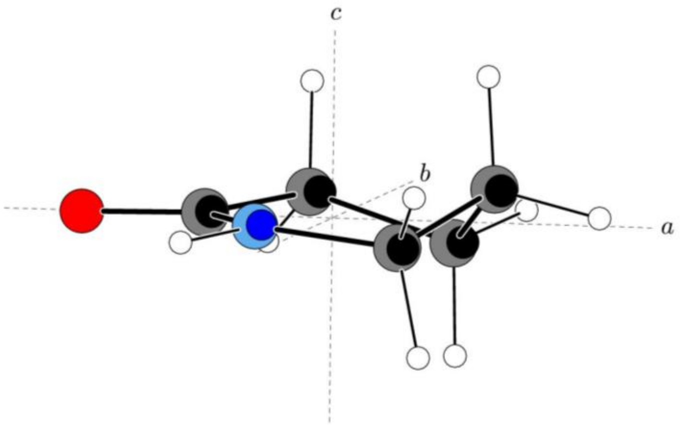

Figure 7.3. Substitution structure of δ-valerolactam (small circles), compared to an *ab initio* structure calculated at the M052x/6-31+g(d) level of theory (large circles). The diameter of the *ab initio* atom positions is 0.45 Å, while the diameter of the experimental atom positions is 0.30 Å.

Additional lines were detected in the broadband spectrum that correspond to the pure rotational transitions of single and double water complexes of DVL; see Table 7.3. In the single water complex, as shown in Figure 7.4, the water makes two hydrogen bonds with DVL, creating a six-membered ring similar to those found in organic acid single water complexes.[3,20] The non-interacting water hydrogen is "out-of-plane", leading to two configurations and a possible motion between them. However, since DVL lacks a plane of symmetry, these configurations are inequivalent and, therefore, no tunneling splittings are observed in the spectrum. The double water complex forms an eight-membered ring, with one water forming a hydrogen bond with the amine group and the other water forming a second hydrogen bond with the carboxyl group. A third hydrogen bond connects the two waters, as in the water dimer.[21] Similar structures also have been observed in organic acid double water complexes.[3,20]

Table 7.3. Rotational and N-14 quadrupole coupling constants of single and double water complexes of δ-valerolactam.

	δ-valerolactam (H_2O)	Theory	δ-valerolactam $(H_2O)_2$	Theory
A (MHz)	3485.929(2)	3493.856[a]	2314.66(1)	2328.24[a]
B (MHz)	1244.7297(8)	1258.315[a]	823.0632(5)	827.218[a]
C (MHz)	954.725(2)	962.679[a]	625.404(1)	629.999[a]
Δ_J (kHz)	0.23(1)		0.116(3)	
Δ_{JK} (kHz)	-0.46(6)		0.14(3)	
δ_J (kHz)	0.042(5)		0.025(2)	
Δ_K (kHz)	1.1(2)		0.38(7)	
χ_{aa} (MHz)	1.70(1)	1.33[b]	1.3(1)	1.1[b]
χ_{bb} (MHz)	2.02(3)	2.35[b]	2.1(1)	2.3[b]
χ_{cc} (MHz)	-3.73(3)	-3.69[b]	-3.4(1)	-3.4[b]

[a] Calculated using Gaussian 03 (M052x/6-31+g(d)).
[b] Calculated from the optimized structure using Gaussian 03 (B3pw91/6-311+g(df,pd)).

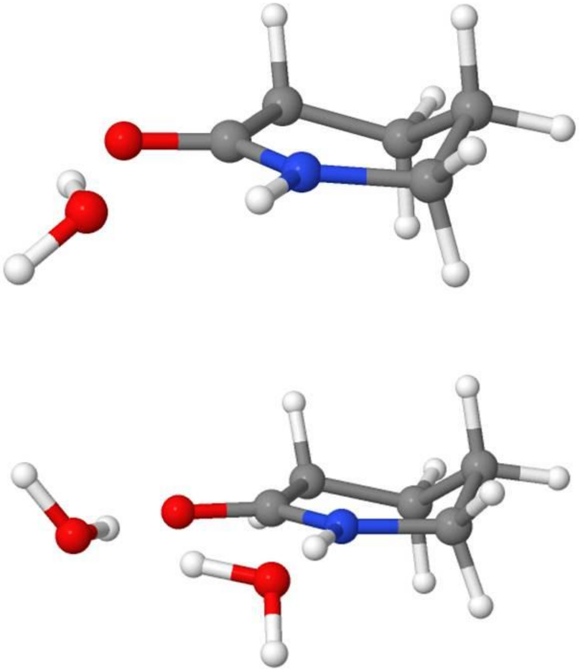

Figure 7.4. Single and double water complexes of δ-valerolactam. The single water complex forms a six-membered ring while the double water complex forms an eight-membered ring.

7.5 DISCUSSION

Figure 7.5 shows a comparison of the structures of propanoic[3] and pentanoic (valeric) acids in the gas phase. Both molecules exhibit an intramolecular interaction between the –OH and C=O groups of the carboxylic acid functionality. Apart from this, most simple carboxylic acids have “straight” chains, in a typical alkane fashion, and are generally unaffected by the presence of the acid group. But the results on AVA show that the addition of a substituent group to a carboxylic acid introduces additional intermolecular interactions that affect its structure.

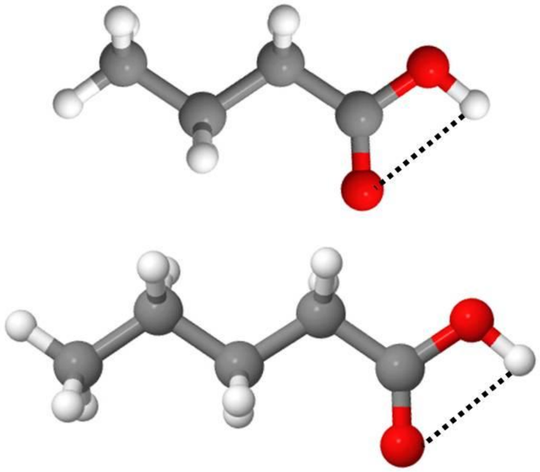

Figure 7.5. Structures of propanoic[9] and pentanoic (valeric) acids with their principal intramolecular interactions depicted as dotted lines.

When AVA was heated in a metal nozzle, it reacted with itself forming DVL. An independent NMR study showed that heating AVA in a glass beaker resulted in no reaction, whereas heating in a metal beaker produced DVL. Therefore, the reaction we observed must have been catalyzed by the metal nozzle. Since this reaction forms a lactam, the initial structure of AVA must be a conformation in which the amine group is interacting with the carbonyl carbon. Such an interaction must result in the formation of a C-N bond and can best be exemplified by an n→π* interaction (Scheme 7.1).

With an understanding of the initial structure of AVA, the full reaction pathway can be calculated using RHF/6-311++g(d,p)[15]; the results are depicted in Figure 7.6. The reaction thus proceeds with the initial formation of an AVA conformer dominated by an n→π* interaction. Next, the reaction continues along the nucleophilic substitution pathway, with an OH^- molecule leaving (7.6b), followed by a bond formation between the carbonyl carbon and anime nitrogen (7.6c). After bond formation the hydroxyl group removes the extra amine hydrogen resulting in a water leaving group and DVL (7.6d), which then vibrates until it reaches its lowest energy conformation (7.6e). It should be noted that the water leaves from a position above the ring plane, while in the water complex (Figure 7.4), the water bonds in the plane of the ring. Thus the water leaving during the reaction is not the same water observed in the δ-valerolactam-water complex.

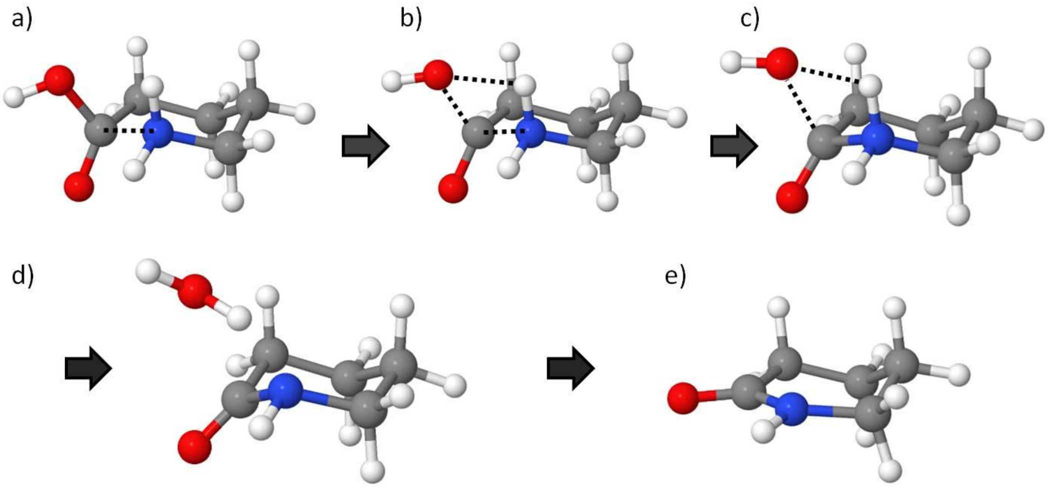

Figure 7.6. The reaction pathway of AVA to δ-valerolactam calculated using RHF/6-311++g(d,p).[15]

The relative energy of the reaction coordinate can be seen in Figure 7.7 with the steps from Figure 6a-e superimposed upon it. The overall reaction is exothermic by 100 kJ/mol with an activation energy of 120 kJ/mol. The point where the water molecule first leaves (Figure 7.6d) was determined to be the transition state, after which DVL loses significant energy upon vibrational relaxation. Of all the possible conformations for AVA, the only one that would result in the formation of DVL is that shown in Figure 6a. The n→π* interaction not only stabilizes this conformer, but it also initiates the nucleophilic attack. Furthermore, since no conformer of AVA was observed in the microwave spectrum, we can assume that the conformer in 6a is the most prevalent and lowest energy conformer, with the later being proven by theoretical calculations.

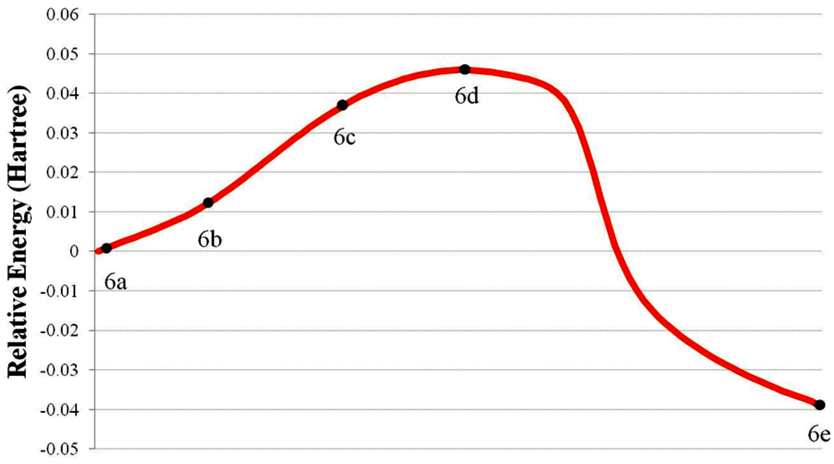

Figure 7.7. The reaction coordinate of AVA and δ-valerolactam with the steps from Figure 6a-e superimposed.

A comparison of the lowest energy conformation of β-alanine[4], GABA,[5] and AVA is depicted in Figure 7.8. As can be seen, both AVA and GABA conformers are dominated by n→π* interactions, while β-alanine is stabilized by an NH···O hydrogen bond. Thus, we conclude that the addition of a single carbon atom to the backbone of an amino acid has a dramatic effect on its preferred conformation. Increasing the length of the chain from a β-amino acid to a γ-amino acid changes the preferred stabilizing interaction from a standard NH···O hydrogen bond to an n→π* interaction. Further increasing the length of the chain from a γ-amino acid to a δ-amino acid only strengthens the interaction. The resulting n→π* interaction is so strong that the molecule readily reacts to form DVL. Initially, one would expect steric effects to be responsible for this trend; the longer the carbon backbone, the closer the nitrogen and carbonyl carbon can interact. However, a comparison of the theoretical structures of the three species reveals that the N-COOH distances are same in all three molecules (~2.9 Å). While these distances are short enough to accommodate proper n→π* overlap, their angles are not. Bürgi and Dunitz found the best C=O···N angle for nucleophilic attack to be 105 ± 5°.[1] AVA displays and angle that is closest to this (96°), followed by GABA (88°), and finally β-alanine

(78°). Therefore, it can be confirmed that angle of nucleophilic attack has a great effect on the strength of the n→π* interaction. Furthermore, as this angle approaches 105°, the stability of the conformer increases, this explains why no other conformation of AVA was observed.

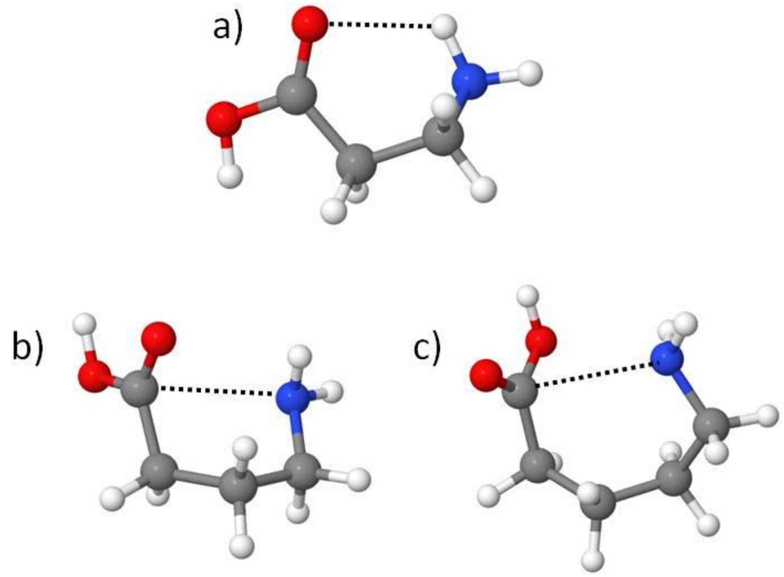

Figure 7.8 A comparison of the lowest energy conformers of β-alanine, (a) GABA, (b) and AVA (c).

Finally, we made an interesting observation while studying the isotopomer spectra of DVL. In the example of the $3_{03} \leftarrow 2_{02}$ transition shown in Figure 7.9, the intensity of the $^{13}C_6$ transition is larger than any other ^{13}C isotopomers. The compared lines consist of the same quantum numbers and are close enough in frequency to be experiencing the same microwave field strength. Additionally, the dipole moments for all isotopomers are expected to be the same, and so their relative intensities are a direct measurement of their relative population. Therefore, there is a greater population of $^{13}C_6$ compared to any other isotopomer. This difference in population was created during the reaction of AVA, a phenomenon known as the kinetic isotope effect.[22] Since the population of $^{13}C_6$ is affected by this reaction, whereas $^{13}C_3$ isn't (Figure 7.10, Supplementary Information), the increase in $^{13}C_6$ signal reflects an increases the rate of the DVL formation, a result known as an inverse kinetic isotope effect. Unfortunately, a study on this effect produced inconclusive findings due to large standard deviations caused by the presence of quadrupole splittings along with poor signal to noise ratios.

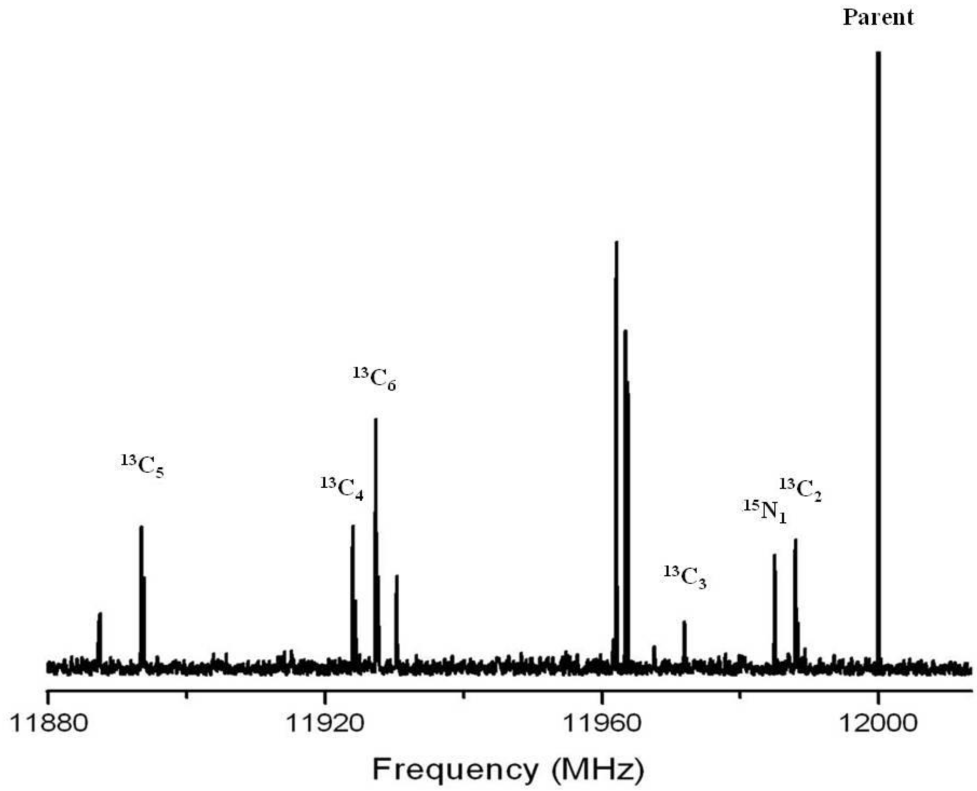

Figure 7.9. The parent and C-13 and N-15 isotopomer 3_{03}←2_{02} transitions of δ-valerolactam.

Summarizing, a study of the reaction of AVA and the structure of its product, DVL, revealed its preferred conformation. Comparisons of AVA, GABA and β-alanine revealed the importance of the nucleophilic attack angle and its effect on the strength of the n→π* interaction. This angle is greatly affected by the number of carbons in the backbone. Conversely, a comparison of VA and propanoic acid showed that additions to the carbon backbone have minimal affect on simple carboxylic acids. Furthermore, the strength and reactivity of the n→π* interaction in δ-amino acids would inhibit the creation of polypeptides, thus diminishing its evolutionary relevance.

7.6 ACKNOWLEDGMENTS

This research has been supported by NSF (CHE-0618740 and CHE-0960074).

7.7 REFERENCES

(1) H. Fu, G. R. Grimsley, A. Razvi, J. M. Scholtz, C. N. Pace, Proteins: Struct. Funct. Bioinform. 77 (2009) 491-498.

(2) http://www.sigmaaldrich.com

(3) B. Ouyang, B. J. Howard, J. Phys. Chem. A 112 (2008) 8208-8214.

(4) S. J. McGlone, P. D. Godfrey, J. Am. Chem. Soc. 117 (1995) 1043-1048.

(5) M. E. Sanz, A. Lesarri, M. I. Peña, V. Vaquero, V. Cortijo, J. C. López, J. L. Alonso, J. Am. Chem. Soc. 128 (2006) 3812-3817.

(6) S. Blanco, J. C. López, S. Mata, J. L. Alonso, Angew. Chem. Int. Ed. 49 (2010) 9187-9192.

(7) H. B. Bürgi, J. D. Dunitz, E. Shefter, J. Am. Chem. Soc. 95 (1973) 5065-5067.

(8) M. P. Hinderaker, R. T. Raines, Protein Sci. 12 (2003) 1188-1194.

(9) J. A. Hodges, R. T. Raines, Org. Lett. 8 (2006) 4695-4697.

(10) A. Choudhary, K. J. Kamer, M. W. Powner, J. D. Sutherland, R. T. Raines, ACS Chemical Biology 5 (2010) 655-657.

(11) S. K. Holmgren, K. M. Taylor, L. E. Bretscher, R. T. Raines, Nature 392 (1998) 666-667.

(12) C. Fufezan, Proteins: Structure, Function, and Bioinformatics 78 (2010) 2831-2838.

(13) G. J. Bartlett, A. Choudhary, R. T. Raines, D. N. Woolfson, Nat. Chem. Biol. 6 (2010) 615-620.

(14) G. G. Brown, B. C. Dian, K. O. Douglass, S. M. Geyer, S. T. Shipman, B. H. Pate, Rev. Sci. Instrum. 79 (2008) 053103.

(15) R. G. Bird, J. L. Neill, V. J. Alstadt, B. H. Pate, D. W. Pratt, in preparation.

(16) M. J. Frisch, G. W. Trucks, H. B. Schlegel, G. E. Scuseria, M. A. Robb, J. R. Cheeseman, J. A. J. Montgomery, T. Vreven, K. N. Kudin, J. C. Burant, J. M. Millam, S. S. Iyengar, J. Tomasi, V. Barone, B. Mennucci, M. Cossi, G. Scalmani, N. Rega, G. A. Petersson, H. Nakatsuji, M. Hada, M. Ehara, K. Toyota, R. Fukuda, J. Hasegawa, M. Ishida, T. Nakajima, Y. Honda, O. Kitao, H. Nakai, M. Klene, X. Li, J. E. Knox, H. P. Hratchian, J. B. Cross, V. Bakken, C. Adamo, J. Jaramillo, R. Gomperts, R. E. Stratmann, O. Yazyev, A. J. Austin, R. Cammi, C. Pomelli, J. W. Ochterski, P. Y. Ayala, K. Morokuma, G. A. Voth, P. Salvador, J. J. Dannenberg, V. G. Zakrzewski, S. Dapprich, A. D. Daniels, M. C. Strain, O. Farkas, D. K. Malick, A. D. Rabuck, K. Raghavachari, J. B. Foresman, J. V. Ortiz, Q. Cui, A. G. Baboul, S. Clifford, J. Cioslowski, B. B. Stefanov, G. Liu, A. Liashenko, P. Piskorz, I. Komaromi, R. L. Martin, D. J. Fox, T. Keith, M. A. Al-Laham, C. Y. Peng, A. Nanayakkara, M. Challacombe, P. M. W. Gill, B. Johnson, W. Chen, M. W. Wong, C. Gonzalez, J. A. Pople, (2004).

(17) D. F. Plusquellic, R. D. Suenram, B. Mate, J. O. Jensen, A. C. Samuels, The Journal of Chemical Physics 115 (2001) 3057-3067.

(18) N. Kuze, H. Funahashi, M. Ogawa, H. Tajiri, Y. Ohta, T. Usami, T. Sakaizumi, O. Ohashi, J. Mol. Spectrosc. 198 (1999) 381-386.

(19) W. Gordy, R. L. Cook, Microwave Molecular Spectra. 3rd ed.; Wiley-Interscience: New York, 1984.

(20) D. Priem, T. K. Ha, A. Bauder, J. Chem. Phys. 113 (2000) 169-175.

(21) L. H. Coudert, J. T. Hougen, J. Mol. Spectrosc. 139 (1990) 259-277.

(22) D. A. Singleton, A. A. Thomas, J. Am. Chem. Soc. 117 (1995) 9357-9358.

7.8 SUPPLEMENTAL MATERIALS

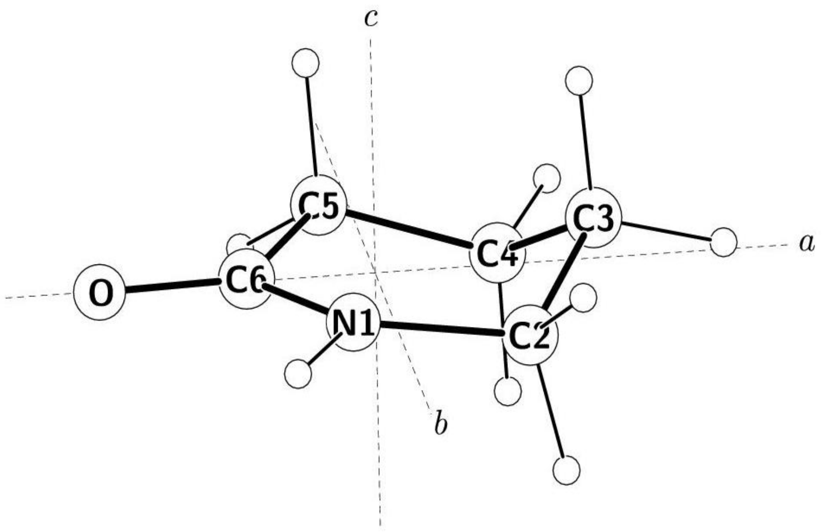

Figure 7.10. Atom labels for δ-valerolactam.

Table 7.4. Fit rotational constants of singly substituted isotopomers of δ-valerolactam

	^{15}N (1)	^{13}C (2)	^{13}C (3)	^{13}C (4)	^{13}C (5)	^{13}C (6)	Parent
A (MHz)	4537.26(4)	4591.09(4)	4520.36(3)	4528.26(1)	4586.77(2)	4524.46(3)	4590.9052(8)
B (MHz)	2493.635(2)	2481.339(1)	2493.924(1)	2476.8510(4)	2454.0144(9)	2479.800(1)	2495.0462(9)
C (MHz)	1722.705(2)	1724.486(4)	1720.576(3)	1714.485(1)	1711.834(2)	1714.522(3)	1731.0549(3)
χ_{aa} (MHz)		2.34(2)	2.34(2)	2.31(1)	2.32(1)	2.30(2)	2.33(1)
χ_{bb} (MHz)		1.40(6)	1.85(3)	1.81(2)	1.86(8)	1.93(6)	1.85(2)
χ_{cc} (MHz)		-3.74(6)	-4.19(3)	-4.12(2)	-4.18(8)	-4.23(6)	-4.18(2)
N_{lines}	9	31	25	25	20	26	132

Table 7.5. Heavy-atom substitution coordinates of δ-valerolactam

Atom	|*a*| (Å)	|*b*| (Å)	|*c*| (Å)
N_1	0.338(5)	-1.149(1)	-0.02(1)
C_2	1.061(1)	-0.076(2)	-0.03(4)
C_3	0.273(5)	1.310(1)	-0.13(1)
C_4	-1.175(1)	1.207(1)	0.312(4)
C_5	-1.817(1)	-0.07(2)	-0.326(5)
C_6	-1.099(1)	-1.275(1)	0.16(1)